



DISSERTATION

Passive Temperature Threshold Sensor

ausgeführt zum Zwecke der Erlangung des akademischen Grades
eines Doktors der technischen Wissenschaften unter der Leitung von

Ao. Univ.-Prof. Dipl.Ing Dr. Franz Keplinger
Institut für Sensor- und Aktuatorssysteme

eingereicht an der Technischen Universität Wien
Fakultät für Elektrotechnik und Informationstechnik

von

Harald Steiner

Matr.-Nr. 0126079

Wien, im August 2014

The research presented in this thesis was carried out at the Institute of Sensor and Actuator Systems, Vienna University of Technology and the Center for Integrated Sensor Systems, Danube University Krems, Wiener Neustadt.

This work was supported by the Austrian Research Promotion Agency (Contactless (RFID) Sensing Project, Project Nr.: 830604).

Supervisor: *Ao. Univ.-Prof. Dr. Franz Keplinger*
Co-supervisor: *Dr. Franz Kohl*

Referee I: *Ao. Univ.-Prof. Dr. Franz Keplinger*
 Institute of Sensor and Actuator Systems
 Vienna University of Technology, Austria
Referee II: *Univ.-Prof. Dr. Bernhard Jakoby*
 Institute for Microelectronics and Microsensors
 Johannes Kepler University Linz, Austria

Contents

Contents	iii
Kurzfassung	vii
Abstract	ix
Nomenclature	xi
List of Abbreviations	xi
List of Symbols	xii
1 Introduction	
or	
The First Step is Always the Toughest	1
1.1 Project Overview	1
1.2 State-of-the-Art	2
1.2.1 Chemical Principle	2
1.2.2 Magnetic Principle	3
1.2.3 Thermal Latch	4
1.3 Summary	10
2 Second Law of Thermodynamics	
or	
Why Stones Won't Fall Upwards	11
2.1 Definition	11
2.2 Examples	14
2.2.1 Jumping Stones	14
2.2.2 Falling Stone in Air	16
2.3 Impact on the Design of MEMS	17
2.3.1 Stiction	18
2.3.2 Mechanical Deformation	19
3 Design	
or	
Limitation of the Diversity of Solutions	23
3.1 Definition of the Problem	23

3.1.1	Boundary Conditions	24
3.1.2	Proposed Solution	25
3.2	Thermal Actuator	25
3.2.1	Design Considerations	27
3.2.2	Finite Element Model Simulation	33
3.3	Latch Mechanism	38
3.3.1	Triangle Shaped Latch	41
3.3.2	Circular Shaped Latch	43
3.3.3	Bistable Beam	44
3.4	Choice of Material	47
3.5	Analytical Model	49
3.5.1	Spring Stiffness of the Lever Transmission	50
3.5.2	Spring Stiffness of V-shaped Beam	52
3.5.3	Energy Equilibrium	54
4	Manufacture	
	or	
	Dos and Dont's	61
4.1	Technologies based on SU-8	61
4.1.1	SU-8 with SU-8 Technology	62
4.1.2	Cu with SU-8 Technology	64
4.1.3	SU-8 Technology Backside Released	68
4.2	Technologies based on Ni	74
4.2.1	Metal MUMPs Technology	74
4.2.2	Electroplated Ni Technology	77
5	Characterization Methods	
	or	
	The Art of Reproducible Results	85
5.1	Deflection	85
5.1.1	Temperature Setup	86
5.1.2	Image Processing	89
5.2	Intrinsic Stress	91
5.3	Young's Modulus	92
5.4	Stress Gradient	93
5.5	Coefficient of Thermal Expansion	94
5.6	Electrical Read Out	96
6	Achievements and Performance	
	or	
	What You Expect and What You Get	97


6.1	SU-8 Actuators	97
6.1.1	Design	98
6.1.2	Thermal Performance	99
6.1.3	Resonance Measurements	99
6.2	Ni Actuators	100
6.2.1	Europractice	100
6.2.2	Happy Plating	107
6.3	Thermal Threshold Sensor	112
6.3.1	Concept A	112
6.3.2	Concept B	115
6.3.3	Readout	119
7	Conclusion	
	and	
	What the Future Brings	121
7.1	Conclusion	121
7.2	Outlook	126
	Bibliography	129
	Danksagung	143
	About the Author	145

Kurzfassung

Jedes Jahr müssen Blutkonserven in Spitälern vernichtet werden, weil die korrekte Lagertemperatur der einzelnen Konserven nicht zweifelsfrei gewährleistet werden kann. Auch im Bereich von Kühlgütern ist es wichtig zu wissen, ob die Kühlkette im Laufe des Transports oder der Lagerung unterbrochen wurde. Es existiert eine Vielzahl von kommerziell erhältlichen Temperaturindikatoren, welche hauptsächlich auf chemischen Reaktionen basieren. Aber es fehlt die Möglichkeit einer einfachen, kosteneffizienten und stromsparenden Anzeige. Auch die Langzeitstabilität solcher Systeme ist zumeist nicht gewährleistet.

Zur Überwachung der Grenzwerttemperatur sind daher neue Ansätze für miniaturisierte passive Sensorsysteme notwendig. Solche Systeme kombinieren RFID Technologien zum Übertragen von Informationen und elektrischen Energien, Kapazitäten zur Zwischenspeicherung der Energien und die Temperaturaufnehmer zur Überwachung der Grenzwerte.

Ziel der Arbeit ist das Design und ein proof-of-concept eines passiven mikro-elektro-mechanischen Temperaturwandlers zur Überwachung einer gewissen Grenztemperatur. Der Wandler besteht aus einem thermischen Aktuator und Einrastmechanismen. Der thermische Aktuator wandelt die thermische Energie zufolge Temperaturänderungen des Kühlgutes in eine mechanische Energie um. Diese Energie wird genutzt um einen Einrastmechanismus zu aktivieren, welcher den Zustand des Sensors unwiderruflich ändert sobald eine definierte Grenztemperatur überschritten wird. Ein ausgeklügeltes Design erlaubt die Produktion und den Transport des Sensorsystems bei Raum- oder erhöhten Temperaturen. Nachdem das System bei niedrigen Temperaturen aktiviert wurde, kann ein Überschreiten einer Grenztemperatur festgestellt werden. Der Wandler arbeitet dabei komplett passiv und braucht keine elektrische Versorgung für die Überwachung.


Um zukünftig sowohl die RFID Antenne, die Speicherkapazität, die elektrische Auswerteschaltung und den mechanischen Temperaturwandler als eine Einheit zu produzieren, werden nur CMOS kompatible Prozesse zur Fertigung des Prototypen verwendet. 

Abstract

A huge amount of blood bottles in hospitals have to be disposed every year since the proper storage temperature could not be guaranteed. Also for refrigerator cargo it is important to know if the temperate chain was broken during the transport. Several temperature indicator labels are available on the market that commonly bases on chemical reactions and color change or darkening. But they lack the possibility of an easy, cost efficient, and low-energy readout. Furthermore, they have issues with their long-term stability.

Therefore, novel approaches for miniaturized passive sensor systems for the observation of threshold temperatures are necessary. Ideally, such systems are a combination of an RFID tag with an antenna for readout and power transmission, a capacitor device to storage the power during the readout, and a transducer device including an evaluation circuits.

The aim of the work is the design and a proof of concept of a passive temperature transducer, which is envisioned as micro-electro-mechanical system. It composes of two parts: A thermal actuator, and a latching mechanism. The thermal actuator converts thermal energy, due to a change in the temperature of the cargo, into mechanical energy. This mechanical energy is applied to a latching mechanism. At a specific threshold temperature, the latching mechanism hooks with its counterpart and irreversible changes the state of the device. A sophisticated design allows for production, transport, and storage of the devices at ambient or raised temperatures. Once it is activated at lower temperatures, an exceeding of a specific threshold temperature can be recorded even when the cargo is cooled down again. The transducer element is completely passive and does not need any power supply during the monitoring of the transport chain.

Pursuing the goal of a single unit package, it will be considered whether the RFID-antenna and perhaps even the capacitor and readout circuit could be manufactured together with the MEMS-transducer on the same chip. This is a boundary condition for the manufacturing of the MEMS subsystem. Hence, only standard CMOS compatible manufacturing process are applied for the fabrication of the device. 

Nomenclature

List of Abbreviations

ASIC	Application Specific Integrated Circuit
Au	Gold
Bosch Process	specific plasma etch process
CMOS	Complementary Metal Oxide Semiconductor
CoF	Coefficient of Friction
Cr	Chromium
CTE	Coefficient of Thermal Expansion
Cu	Copper
DI	DeIonized
DRIE	Deep Reactive Ion Etch
FEM	Finite Element Model
HB	Hard Bake
HF	Hydrofluoric Acid
IC	Integrated Circuit
KOH	Potassium Hydroxide
MEMS	Micro Electro Mechanical System
MSA	Micro System Analyzer
MUMPs	Multi-User Multi-Projects
N ₂	Nitrogen (molecular)
Ni	Nickel

PAG	Photo Acid Generator
PEB	Post Exposure Bake
PGMEA	Propylene Glycol Methyl Ether Acetate
PID	Proportional, Integral, Differential
PP	Polypropylen
Pt	Platinum
RFID	Radio Frequency Identification
SEM	Scanning Electron Microscope
SU-8	Negative Photoresist
Ti	Titanium
UV	Ultra Violet
VUT	Vienna University of Technology

List of Symbols

α	Coefficient of Thermal Expansion (CTE)	ppm/K
ΔT	Temperature Difference	K
ϵ	Strain	m/m
ϵ'	Hencky Strain	m/m
Γ	Vertical Stress Gradient	Pa/m
γ	Angle	rad
γ_s	Surface Energy Density	J/m ²
μ_0	Coefficient of Friction	1
ν	Poisson's Ratio	1
Ω	Number of Microstates	1
ρ	Density	kg/m ³

ρ_o	Optimization Parameter $\in [0,1]$	1
σ	Mechanical Stress	N/m ²
A	Cross Section Area, Area	m ²
A_S	Surface Area	m ²
b	Beam Width	m
d	Deflection	m
D_1	Gray Value Difference	1
E	Young's Modulus	N/m ²
F	Force	N
$F(T)$	Helmholtz Free Energy	J
f_i	i -th Natural Frequency	Hz
$G(T, P)$	Gibbs Free Energy	J
G_1, \tilde{G}_1	Grey Value	1
h	Height	m
$H(P)$	Enthalpy	J
h_a	Apex Height	m
I	Areal Moment of Inertia	m ⁴
i	Current	A
k	Spring Stiffness	N/m
k_B	Boltzmann Constant (1.38e-23 J/K)	J/K
k_{react}	Reaction Rate Constant	mol ¹⁻ⁿ · l ⁿ⁻¹ /s
l	Length	m
M	Momentum	Nm
N_P	Peelnumber	1
P	Pressure	Pa

p	Penalization Parameter (p=3)	1
Q	Heat, Thermal Energy	J
Q_a	Aspect Ratio	1
r	Radius	m
S	Entropy	J/K
S_A	Elastic Section Modulus	m ³
T	Temperature	K
t	Beam Thickness	m
U	Energy	J
u	In-plane Deflection	m
U_E	Elastic Energy	J
w	Deflection	m
W_{Area}	Area Specific Work	J/K ² m ²
x	Deflection, Offset	m
y	Deflection, Offset	m

"Call me Ishmael."

Herman Melville, Moby-Dick
1851

"If I have seen further it is by standing on ye sholders of Giants. [sic]"

Sir Isaac Newton, Letter to Robert Hooke
1676

"To raise new questions, new possibilities, to regard old questions from a new angle, requires creative imagination and arks real advances in science."

Albert Einstein

1 Introduction or The First Step is Always the Toughest

IT is always a good idea to start at the beginning. Scientific projects start mainly with an idea, how to solve a problem in a new manner or facing a new problem. Sometimes, there is also a novel solution and the inventor tries to figure out the corresponding problem. Both approaches have in common, that the pros and cons are evaluated and compared to the state-of-the-art. Before the scientific work can begin, the funding of the project must be raised. This can be a frustrating process, but belongs also to the work of a scientist as the actual scientific work. E.g., this project was funded by the Austria Research Promotion Agency in cooperation with Infineon Austria.

The following chapter describes the principal challenge including a discussion of state-of-the-art solutions.

1.1 Project Overview

The main aim of the work is an entirely **passive temperature threshold sensor**. The idea is to apply a small sensor device to a reefer cargo or other goods that need to be stored at low temperatures. This device should have an electrical readout, which is easily accessible via an RFID- (Radio Frequency Identification) reader. Furthermore, it should be able to track a specific threshold temperature without any power supply, e.g.,

battery. The sensor has to be robust for the use in harsh environments and a cost efficient fabrication technology is mandatory.

The temperature of a reefer cargo, e.g., in the food industry, is only checked randomly during storage and transportation, commonly by a contact thermometer on the out side of the package. Due to accommodativeness, only easily accessible spots of the goods or cargo are checked. Hence, the individual temperature distribution of a whole reefer cargo transporter/container is never examined. It can happen that the cooling chain is somewhere broken [1, 2]. This is a huge problem for blood transfusion bags in the clinical usage [3]. Large amounts of blood bags have to be destroyed every year, because there is no possibility to check if a single bag has exceed a defined threshold temperature.

The proposed sensor device can be applied to each individual cargo package. It holds a transducer element, a read/write antenna and an electric processing unit with a storage capacitor. The sensor is only powered during the readout process. The required energy is transferred via the RFID antenna and temporarily stored in the capacitor. A readout pulse is transmitted to the device when sufficient power is stored. An electrical processing unit checks the state of the sensor and sends back an according response.

This thesis focuses on the transducer element, which should be manufactured by micro fabrication technologies on wafer level for economical reasons.

1.2 State-of-the-Art

An easily exploitable intrinsic temperature dependent material parameter has to be applied as transduction principle due to the restricted power supply requirements. A significant measurable change of the state of the sensor must be obtained when a specific threshold temperature is exceeded. A summary of the most promising state-of-the-art approaches is summarized and the individual pros and cons are discussed.

1.2.1 Chemical Principle

Chemical reactions depend strongly on time and temperature. Accordingly to the law of Arrhenius¹, the rate constant k_{react} of a chemical reaction of the kind

¹Svante August Arrhenius, Swedish physicist and chemist, 1859-1927.



is given as

$$k_{\text{react}} = A_0 \exp\left(-\frac{E_A}{k_B T}\right) \quad . \quad (1.2)$$

Hence, a chemical reaction speeds up for higher temperatures. In this equation is A_0 the pre-exponential factor, E_A the activation energy for the chemical reaction, k_B the Boltzmann² constant and T the absolute temperature. The reaction constant k_{react} measures the speed of a chemical reaction. Chemical reactions can be tailored to take place slowly at low temperatures and speed up about several orders of magnitude for higher temperatures (when $k_B T$ is in the range of the activation energy). Hence, the reaction, e.g., change in color, can be exploited as an indicator for a specific threshold temperature.

Plenty of temperature indicator labels are available on the market and they are commonly used to verify the condition of reefer cargo. Most of them changes their color and can be used as readout out without additional equipment. But they lack the possibility to monitor fast or only small over-temperatures. Because the chemical reaction also depends on time, also the time since when the label was attached to the cargo must be known to make adequate statements about the condition of the goods, commonly called time-temperature combination [4, 5].

1.2.2 Magnetic Principle

With new advances in material science, especially in the field of magnetic materials, another possible sensing method arises. Recently, a start-up developed a temperature indicator sensor, based on magneto-elastic resonance measurements, which are commonly used for electronic article surveillance [6, 7]. A thin amorphous metal strip is mechanical oscillating due to magneto-striction in a time varying magnetic field. When this amorphous strip is excited at its mechanical resonance frequency and the magnetic field is turned off, it oscillates freely for a few milliseconds. The resonance frequency is mainly determined by the length and the Young's³ modulus of the strip. With a constant magnetic bias, e.g., provided by a permanent magnet, the mechanical oscillation results in a

²Ludwig Boltzmann, Austrian physicist, 1844-1906.

³Thomas Young, British ophthalmologist and physicist, 1773-1829.

changing magnetization that can be monitored by an electrical pick up coil.

For a temperature indicator sensor, a magnetic shape memory alloy layer is added between the permanent magnet and the amorphous resonator strip. The Curie⁴ temperature of this layer can be tailored in accordance to the application by changing the composition of the alloys. When the threshold temperature (Curie temperature) is exceeded, the bias magnetic field at the resonator is significantly changed. This change results in a detectable shift of the resonance frequency because of the magnetic field dependency of the Young's modulus. Hence, the response frequency is a measure for the state of the cargo [8,9].

Large coils have to be used to generate sufficient excitation amplitudes because the magnetic field is proportional to $1/r^3$, where r is the radial distance from the center of the coil. When several sensors are placed next to each other, all of them are excited and the response is a superimposition of all of them. Up to now, it is not possible to distinguish individual sensors.

1.2.3 Thermal Latch

A micro fabricated latch mechanism consists of a hook and a counterpart, where one or both parts are connected to a flexible micro structure. When a force is applied, e.g., mechanical shock or electrical voltage, both parts can be brought into contact to each other, establishing an irreversible mechanical connection [10–15]. Such a latch can also be activated by an electro-thermal actuator exploiting the thermal expansion of a material [16–19].

Thermal Expansion

The origin of the thermal expansion of a material can be found in the thermally induced oscillation amplitude of the atoms in a solid. But the descriptive model of two atoms, connected by a linear spring, cannot solely explain the thermal expansion. The interaction-potential of such a model is symmetric and the mean distance between the atoms would remain constant when the vibration amplitude is increased. Only a non-symmetric interaction model, such as the Lennard-Jones⁵ potential, leads to a thermal expansion. This potential is given by

⁴Pierre Curie, French physicist, 1859-1906.

⁵John Lennard-Jones, British mathematician, 1894-1954.

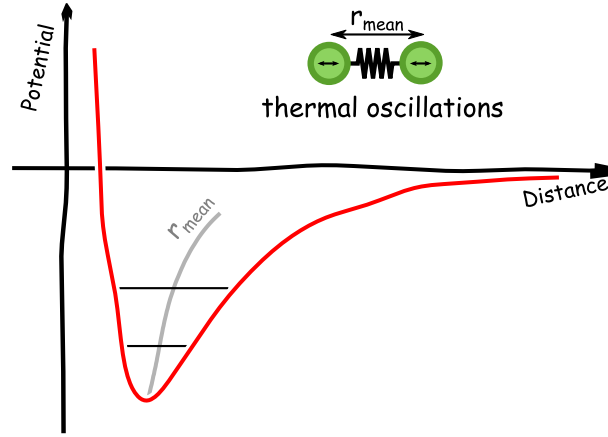


Figure 1.1: The interaction between two atoms can be described by the Lennard-Jones potential. The mean distance between two atoms increases with larger thermal oscillations due to the non-linearity of the potential. Hence, a material expands with increasing temperature.

$$V(r) = -\frac{a}{r^6} + \frac{b}{r^{12}} \quad . \quad (1.3)$$

with a, b empirical constants and r the distance between both atoms (Fig. 1.1). The potential describes a long range attraction (Van der Waals⁶ force, Dipole-Dipole interaction) and a short range repulsion (Pauli⁷ repulsion resulting from overlapping electron orbitals) of the atoms. It can be assumed that the spring becomes stiffer when both atoms get closer to each other. This non-linearity results in an increased mean distance r_{mean} for larger thermal oscillation amplitudes and, therefore, in a thermal expansion of the material.

Thermal Actuator

The difference in thermal expansion of two materials can be used to build up an actuator systems. The thermal expansion itself is in the range of a few ppm/K for most of the technical materials. Hence, the mechanical elongation must be amplified by a sophisticated design to gain displacements of several tens of μm . In the recent years, thermal actuators became popular in MEMS technology [20–22]. Commonly,

⁶Johannes Diderik van der Waals, Dutch physicist, 1837-1923.

⁷Wolfgang Ernst Pauli, Austrian physicist, 1900-1958.

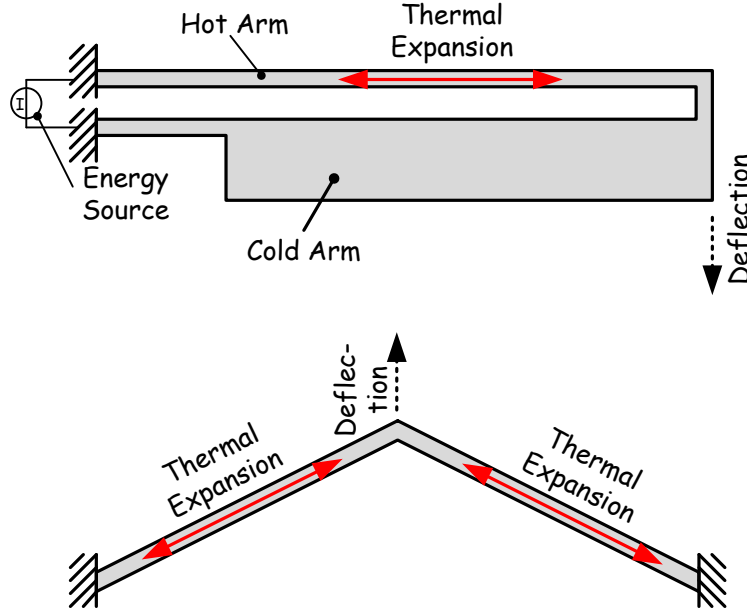


Figure 1.2: Basic geometries for thermal actuators. U-shaped beams rely on the temperature difference between a hot and a cold arm. V-shaped beams exhibit a deflection or buckling perpendicular to the elongation of the beam.

they are heated via Joule⁸ heating up to several hundred degree Celsius⁹ [23–27]. There are two basic concepts for such actuators; U-shaped and V-shaped geometries (Fig. 1.2).

The U-shaped actuators exhibit an arm with a low electrical resistivity and another arm with a higher resistivity. Both are mechanically connected and the temperature increases at the arm with higher resistivity due to Joule heating. This results in a larger thermal expansion of the hotter arm and, hence, an in-plane deformation of the whole structure. The resistivity of the cold arm can be reduced by applying a metal layer on top of the arm or by an increased width of the arm [28–30].

V-shaped actuators, also called chevron type, rely on two beams with an inclination angle. When the ends of the beams are fixed and the temperature is increased, the thermal expansion leads to a buckling of the structure. State-of-the-art V-shaped actuators are heated also by electrical resistivity heating to get a well defined actuation stroke [31–36]. But it is possible to operate such shapes completely passive. Consid-

⁸James Prescott Joule, British physicist, 1818–1889.

⁹Anders Celsius, Swedish astronomer, 1701–1744.

ering a quasi static condition, where the temperature is homogeneously distributed along the beams. The difference in the thermal expansion of substrate and actuator material leads to a deflection of the structure when the temperature changes. Hence, such an actuator can operate completely passive and only relies on the temperature change of the environment.

In contrast, the U-shaped design always needs a temperature difference between both of its arms. This makes this U-shaped principle worthless for the desired application.

Table 1.1 summarizes deflection, force, occupied chip area, applied temperature difference, thermal sensitivity (deflection per Kelvin¹⁰), basic shape, and active material of published state-of-the-art thermal micro actuators. The data are conscientiously gathered from published literature. The occupied chip area is approximated by measuring the dimensions of the designs presented in the papers from SEM images or schematics. Often only the required electrical power is revealed and the temperature for a specific electric power is extracted by comparing corresponding literature (conference publications, literature showing simulated results, ...) of the cited work and by interpolating data points from graphs depicted in the manuscripts. The shape primary distinguishes between U-, V-, and special (S)- shaped actuators, marking the basic geometry. The S-shaped actuators can not be easily addressed to one of the other types. They summarize geometries like bi-metallic shapes, out-of-plane actuators, linear expanding meander shapes, or more complex topology optimized shapes (see subsection 3.2.1 for details).

Figure 1.3 depicts a graphical illustration of the data given in Tab. 1.1 considering only publications with a specific threshold value for an easier overview. The force per Kelvin over the deflection per Kelvin is depicted in the upper graph. The force cannot be approximated for every cited publication. Hence, a vertical dashed line marks the deflection of relevant experimental works with missing data. The lower graph depicts the area specific work (force-displacement product) per squared Kelvin versus the deflection per Kelvin per area. The force-displacement product is a measure for the work the actuator can provide. Both, the deflection and the force depends on the temperature. Hence, the area-specific work scales with the applied squared temperature difference.

¹⁰William Thomson, 1st baron Kelvin, British mathematician and physicist, 1824-1907.

Name 1st Author	Date	Shape	Mat.	d μm	F mN	A mm^2	ΔT K	$d/\Delta T$ $\mu\text{m}/\text{K}$
Ando [37]	2011	V	Ni	30.0		1.0	170	0.176
Arthur [38]	2011	V	Si	2.6	0.08	0.6	300	0.009
Chen [39]	2004	V	Si	190.0		0.41	1500	0.127
Chronis [40]	2002	V	SU-8	42.0		0.4	50	0.84
Chronis [41]	2005	U	SU-8	6.0		0.02	55	0.109
Daneshm. [42]	2009	V	Ni	5.0		0.3	188	0.027
Enikov [43]	2005	V	Ni	20.0	1.67	0.11	220	0.091
Guan [44]	2010	S	Si	1.1	0.3	0.06	400	0.003
Huang [45]	1999	U	Si	16.0		0.02	720	0.022
Khazaai [46]	2010	S	Si	6.5	0.04	0.44	200	0.033
Khazaai [47]	2011	V	Ni	81.0	2.4	1.26	170	0.476
Khazaai [48]	2012	V	Ni	13.4	8.4	0.89	180	0.074
Lee [49]	2005	V	Si	50.0				
Luo [50]	2009	V	Ni	17.5		0.3	465	0.038
Matoba [51]	1994	S	Si	6.0		0.02		
Nguyen [52]	2004	U	SU-8	7.5		9.0	11	0.682
Oak [53]	2011	V	Si	10.0	2.76	0.35	600	0.017
Ogando [54]	2012	S	Si	1.0		0.04	300	0.003
Paryab [55]	2009	U	Si	5.0		0.03	580	0.009
Qiu [56]	2005	U	Si	120.0	13.0	1.56	220	0.545
Que [57]	1999	V	Ni	3.0	0.75	0.01	600	0.005
Que [58]	2001	V	Si	3.0	0.13	0.13	48	0.063
Que [58]	2001	V	Si	30.0	0.1	1.0	680	0.044
Sigm. [59]	2001	S	Ni	44.4	6.0	0.1	730	0.061
Sigm. [59]	2001	S	Ni	19.2	40	0.1	472	0.041
Stevens. [60]	2007	S	Si	3.5	0.06	0.3	35	0.1
Wei [61]	2008	S	SU-8	7.0	0.08	0.27	60	0.117
Yan [62]	2004	S	Si	2.0		0.02	400	0.005
Yang [63]	2009	S	Si	250.0	2.0	19.2	700	0.357
Zhu [64]	2006	V	Si	0.7	43.2	0.23	300	0.002

Table 1.1: Overview of design and performance data of state-of-the-art thermal actuators. The column “shape” reveals the principle actuator shape, such as V-, U-, or special shapes (S). The column “material” refers to the active material for the actuator. The data are extracted from literature by interpolating graphs depicted in the publications and by comparing corresponding publications. .

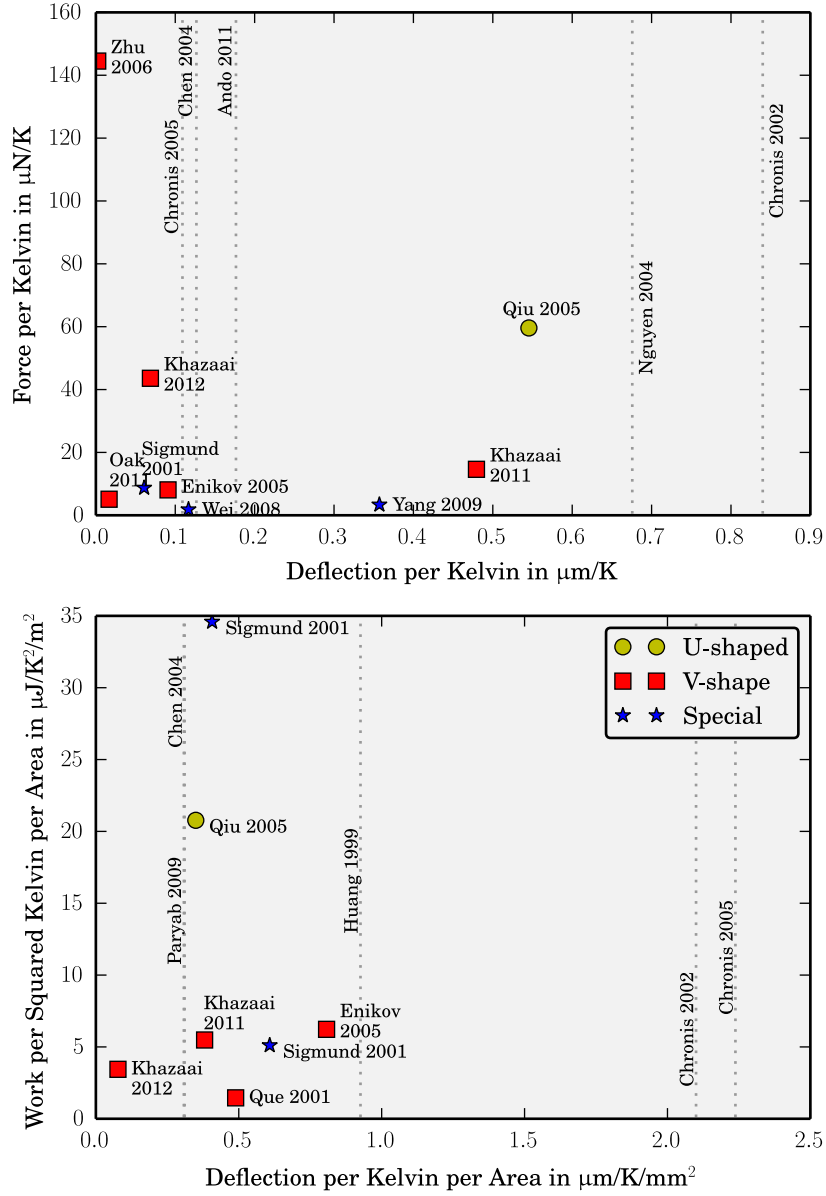


Figure 1.3: Overview of the performance of state-of-art thermal actuators. Vertical dashed lines mark the deflections per Kelvin and area-specific deflections of relevant publications that miss data concerning the available actuation forces.


1.3 Summary

Chemical based sensors lack the possibility of an easy electrical readout because the chemical reaction is mainly designed to change its color. Their sensitivity is defined by the time-temperature product. Hence, they become unstable with increasing time and the information value about exceeding a certain threshold temperature decreases.

Sensors based on magnetic material properties are an interesting concept but lack the possibility of an individual readout of devices that are located next to each other. Furthermore, they require large readout coils and, therefore, there is a high energy consumption for the whole readout process.

Thermal micro actuators are the most promising approach to solve the challenges of designing a passive temperature threshold sensor. In combination with latching mechanisms and RFID antennas, they offer a unique combination of individual identification, easy readability, passive functionality, and well defined behavior when a threshold temperature is exceeded. The restriction of an activation of the sensor device at low temperatures can be smartly solved by applying two separate latches, where the first latch activates the second one when a specific lower temperature is reached.

Important is the thermal sensitivity (deflection per Kelvin) of the actuator. Most of the state-of-the-art actuators are heated up to several hundred °C. For the challenging sensor device, only a few tens of °C are available as temperature difference and several tens of μm of deflection are required to actuate a latching mechanism. Hence, a sensitivity of at least $1\mu\text{m}/\text{K}$ is required, with still sufficient forces to push a latch mechanism and to overcome the friction of the material. Non of the state-of-the-art actuators meet these requirements. Therefore, the actuator designs have to be improved or complete new approaches have to be thought off. Technological processes have to be established for manufacturing the devices with the required boundary conditions, such as; low stress gradient, low initial stress levels, reproducible material conditions, and sufficient aspect ratios.

The design process starts from scratch and has to consider the limitations due to the technological manufacturing process to push the limits of thermal actuators to reliable thermal sensitivities. 

"The law that entropy always increases holds, I think, the supreme position among the laws of Nature. If someone points out to you that your pet theory of the universe is in disagreement with Maxwell's equations then so much the worse for Maxwell's equations. If it is found to be contradicted by observation well, these experimentalists do bungle things sometimes. But if your theory is found to be against the second law of thermodynamics I can give you no hope; there is nothing for it but to collapse in deepest humiliation."

*Sir Arthur Stanley Eddington, The Nature of the Physical World
1927*

Second Law of Thermodynamics 2 or Why Stones Won't Fall Upwards



THIS chapter focus on a fundamental law in nature that results in the simple rule: Systems tend to a state with lowest energy. One can say that it is a philosophic point of view, but the second law of thermodynamics clearly shows why physical systems try to minimize their energy. Even though it represents an empirical law, firstly stated by Rudolf Clausius¹, it has never been proved wrong until now.

The definition of the 2nd Law is given and, subsequently, its impact on physical systems and models is described.

2.1 Definition

The most common and simplest definition of the second law of thermodynamics is

$$\frac{dS}{dt} \geq 0 \quad , \quad (2.1)$$

¹Rudolf Julius Emanuel Clausius, German physicist and mathematician, 1822-1888.

where S is the entropy² in J/K, defined as

$$\Delta S \geq \frac{\Delta Q}{T} \quad , \quad (2.2)$$

or, as stated by Ludwig Boltzmann,

$$\Delta S = k_B \ln \frac{\Omega_1}{\Omega_2} \quad , \quad (2.3)$$

with Q as the heat energy in J, T the absolute temperature in K, k_B the Boltzmann constant and $\Omega_{1,2}$ the number of possible micro-states for the final and initial state. The 2nd law of thermodynamics means, that the entropy of an isolated³ system increases with time and will tend to a maximum, so that the number of possible micro-states is largest. This definition may be the easiest by means of its mathematical formulation but not by means of its physical impact on observable things.

Other equivalent formulations are:

- A perpetual mobile of 2nd kind is impossible.
- There are no naturally spontaneous processes, where the entropy decreases.
- Every closed macroscopic system tends towards its most probable state.
- No process is possible in which the sole result is the absorption of heat from a reservoir and its complete conversion into work.

The second law of thermodynamics enabled the definition of an explicit time arrow of physical processes for the first time in science. Spontaneous processes only occur when the entropy increases. Hence, it is possible to distinguish between initial and final states. If a chemical reaction will occur spontaneously the state with the higher entropy is, by meaning of time, the later one and, therefore, the result. The 2nd law of thermodynamics shows, that in nature, every closed⁴ macroscopic physical system in equilibrium will be found preferably in a state with its lowest energy.

²Named by Rudolf Clausius from the Greek word τροπή [tropē] for transformation.

³An isolated system cannot exchange energy or matter with the surrounding.

⁴A closed system can exchange energy but not matter.

When the entropy $S(U, X_i)$ of a closed system depends on the inner energy $U(S, X_i)$ and another extensive parameter X_i , the system is in thermodynamic equilibrium when the relations

$$\left(\frac{\partial S}{\partial X_i}\right)_U = 0 \quad , \quad (2.4)$$

and

$$\left(\frac{\partial^2 S}{\partial X_i^2}\right)_U < 0 \quad , \quad (2.5)$$

are fulfilled, where $(\partial S/\partial X_i)_U$ means the partial differential for constant U . When Eq. 2.4 and Eq. 2.5 are satisfied, the entropy is in a maximum with $S(U, X_i) = S_0$. Using the properties of the implicit function theorem the differential of $S(U(X_i), X_i)$ leads to

$$\begin{aligned} \left(\frac{\partial S}{\partial X}\right)_U + \left(\frac{\partial S}{\partial U}\right)_X \cdot \left(\frac{\partial U}{\partial X}\right)_{S_0} &= 0 \\ &\stackrel{=0 \quad \text{Eq. 2.4}}{\overbrace{\left(\frac{\partial S}{\partial X}\right)_U}} \rightarrow \left(\frac{\partial U}{\partial X}\right)_{S_0} = 0 \quad . \end{aligned} \quad (2.6)$$

The second partial differential gives

$$\begin{aligned} \left(\frac{\partial^2 S}{\partial X^2}\right)_U + \left(\frac{\partial}{\partial U}\left(\frac{\partial S}{\partial X}\right)_U\right)_X \cdot \overbrace{\left(\frac{\partial U}{\partial X}\right)_{S_0}}^{=0 \quad \text{Eq. 2.6}} + \left(\left(\frac{\partial^2 S}{\partial U^2}\right)_X \left(\frac{\partial U}{\partial X}\right)_{S_0} \right. \\ \left. + \left(\frac{\partial}{\partial X}\left(\frac{\partial S}{\partial U}\right)_X\right)_U \cdot \overbrace{\left(\frac{\partial U}{\partial X}\right)_{S_0}}^{=0 \quad \text{Eq. 2.6}} + \left(\frac{\partial S}{\partial U}\right)_X \cdot \left(\frac{\partial^2 U}{\partial X^2}\right)_{S_0} \right) = 0 \\ \left(\frac{\partial^2 S}{\partial X^2}\right)_U + \left(\frac{\partial S}{\partial U}\right)_X \cdot \left(\frac{\partial^2 U}{\partial X^2}\right)_{S_0} = 0 \end{aligned} \quad (2.7)$$

leading to

$$\left(\frac{\partial^2 U}{\partial X^2}\right)_{S_0} = -\frac{\overbrace{\left(\frac{\partial^2 S}{\partial X^2}\right)_U}^{<0 \quad \text{Eq. 2.5}}}{\left(\frac{\partial S}{\partial U}\right)_X} \rightarrow \left(\frac{d^2 U}{dX^2}\right)_{S_0} > 0 \quad . \quad (2.8)$$

Eq. 2.6 and Eq. 2.8 states, that the inner energy of a closed system in thermodynamical equilibrium is in a minimum for a given total entropy [65].

This energy minimum principle can be extended to other thermodynamical potentials that are derived by Legendre⁵ transformations of the inner energy. The Helmholtz⁶ free energy $F(T)$ is derived by exchanging the entropy S by the temperature T as independent variable. For the enthalpy $H(P)$ the volume is replaced with the pressure P , and the Gibbs⁷ free energy $G(T, P)$ is derived by replacing the entropy and volume with the temperature and pressure as independent variable, respectively [65].

The inner energy and the Helmholtz free energy are commonly the most relevant thermodynamic potential for physical systems. The energy minimum principle results in a minimized Helmholtz free energy for a closed system in thermodynamical equilibrium when the temperature is kept constant (temperature reservoir). The inner energy for such systems is in a minimum, when the entropy is constant. All potentials are equivalent formulations but from a different point of view [65].

2.2 Examples

2.2.1 Jumping Stones

Considering a closed system of a stone with the mass m , held at height h_0 above a plain (Fig. 2.1). The stone has potential and kinetic energy ($E_{\text{pot}}, E_{\text{kin}}$) which is in this case also the inner energy of the system:

$$E_{\text{pot}} + E_{\text{kin}} = U = mgh_0 \quad . \quad (2.9)$$

At first, the stone is at rest and with a kinetic energy of $E_{\text{kin}} = 0$. The potential energy converts into kinetic energy in accordance to

$$E_{\text{kin}} = \frac{mv^2}{2} = mg(h_0 - x) \quad , \quad (2.10)$$

where x is the covered distance directed towards the plain. It is obvious that a gravitational attractive force acts on the stone, resulting in a fall down. From a philosophic point of view, one can state that the thermodynamically driving mechanism for the complete physical process is

⁵Adrien-Marie Legendre, French mathematician, 1752 - 1833.

⁶Hermann von Helmholtz, German physician and physicist, 1821 - 1894.

⁷Josiah Willard Gibbs, American physicist, 1839 - 1903.

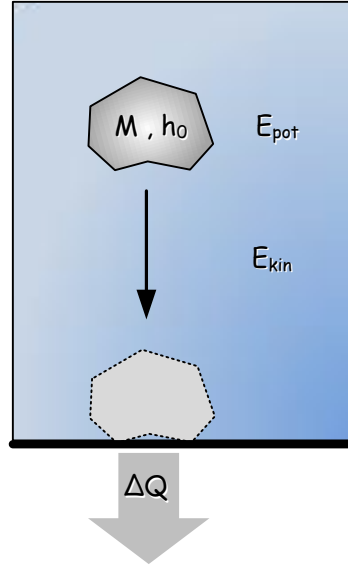


Figure 2.1: A stone with mass m is placed at height h above a plain. The potential energy is converted into kinetic energy. When the stone hits the ground this energy is transformed into thermal energy ΔQ which is released into the surrounding.

the maximization of the entropy or the minimization of the inner energy. Finally, the potential energy is zero and the kinetic energy is transformed into thermal energy ΔQ after the stone hits the ground ($x = h_0$). Hence, the change in entropy is calculated to

$$\Delta S = \frac{\Delta Q}{T} = \frac{\Delta U}{T} = \frac{mgh_0}{T} > 0 \quad . \quad (2.11)$$

The entropy increases (maximizes) when the stone converts its energy into thermal energy. Question: How large is the probability that the stone will spontaneously jump upwards?

As funny as it sounds, there is a possibility that a stone can spontaneously jump upwards to a height h_1 . The change in entropy for such a case is

$$\Delta S = -\frac{mgh}{T} \quad . \quad (2.12)$$

Considering that the change in entropy is the change of the probabilities

$$\Delta S = k_B \ln \frac{\Omega_1}{\Omega_2} \quad , \quad (2.13)$$

where Ω_1 is the probability to find the stone in a height h and Ω_2 is the probability that the stone is found on the bottom ($h = 0$) if the stone can

freely decide. The later one can be set equal to 1. Ω_1 can be calculated to

$$\Omega_1 = \Omega_2 \exp k_B \Delta S = \Omega_2 \exp \left(-\frac{mgh}{k_B T} \right) . \quad (2.14)$$

For $m = 1 \text{ kg}$, $h = 0.3 \text{ m}$, and $T = 300 \text{ K}$ the probability that a stone will spontaneously jump up to 30 cm is $\Omega_1 = \exp(-2 \cdot 10^{-23})$. This is an impressively small number and, therefore, the event is extremely unlikely to happen.

2.2.2 Falling Stone in Air

Another model for the stone can be described by considering the energy loss due to friction in the fluid (Fig. 2.2). The inner energy of a stone in a surrounding air volume consists of the potential and kinetic energy of the stone

$$U = E_{\text{pot}} + E_{\text{kin}} . \quad (2.15)$$

The moving stone in the fluid converts its potential energy loss only partially into kinetic energy, so that the velocity of the stone v can be calculated by

$$v = \sqrt{2gx} . \quad (2.16)$$

The kinetic energy will be partially converted into thermal energy due to friction force F_r (Stokes⁸ drag force) within the fluid

$$F_r = 6\pi r \nu v \quad , \quad Q = \int F dx = \int 6\pi r \nu \sqrt{2gx} dx = 4\pi r \nu \sqrt{2g} x^{\frac{3}{2}} . \quad (2.17)$$

The change in the entropy is therefore

$$\Delta S = \Delta Q/T = 4\pi r \nu \sqrt{2g} \Delta x^{\frac{3}{2}}/T > 0 . \quad (2.18)$$

The temperature T can be assumed to be constant because the volume of the fluid is large. It can be seen, that the entropy change is positive. Hence, the falling of the stone will happen spontaneously. The change in the inner energy of the system is

$$\Delta U = \Delta Q + \Delta E_{\text{pot}} + \Delta E_{\text{kin}} = -6 \cdot \frac{2}{3} \pi r \nu \sqrt{2g} \Delta x^{\frac{3}{2}} - mg \Delta x + mg \Delta x < 0 \quad (2.19)$$

⁸Sir George Gabriel Stokes, 1st Baronet, Irish physicist and mathematician, 1819-1903.

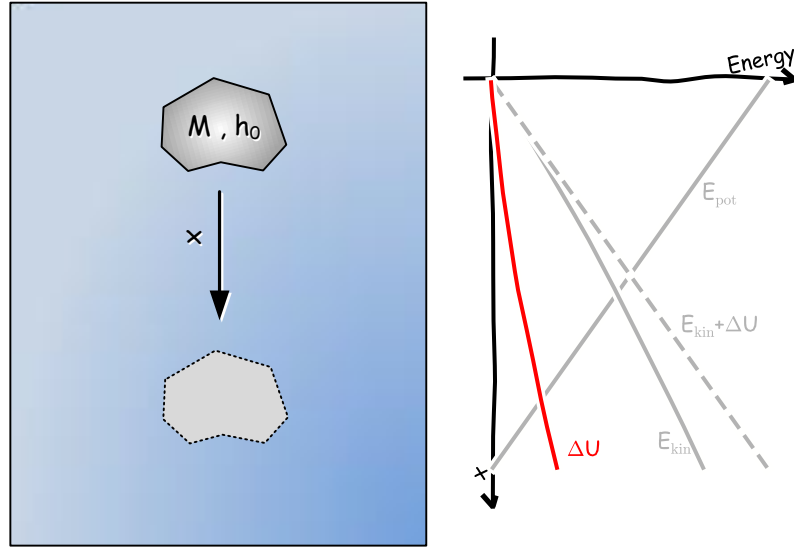


Figure 2.2: Simple model of a falling stone with the corresponding potential energy, kinetic energy and energy loss due to friction.

and, therefore, decreases. The stone “tries” to minimize its internal energy by falling down.

In absence of a fluid (vacuum, interplanetary space) the stone will follow a constant energy surface, converting the kinetic and potential energy in accordance to the gravitational field⁹, resulting in an orbital curve around the earth (neglecting the influence of other gravitational forces, e.g., sun, moon, and other planets). As soon as friction takes place, the energy loss will result in a descendent orbit, till the stone hit the surface of the earth, or vanishes in a temperature induced evaporation and rapid oxidation reaction releasing electro-magnetic waves in the frequency range of $10^{13} - 10^{16}$ Hz, leaving behind only particles.

2.3 Impact on the Design of MEMS

The fact that a system tends to minimize its energy has a large influence on the functionality and the design of MEMS devices. In the following, two major examples are given. First, the stiction (static-friction) due to

⁹The potential energy is only valid near to the surface of a star or planet. For increased distances to the surface, the Newton’s (Isaac Newton, English physicist and mathematician, 1642 - 1727.) law of universal gravitation or the general relativity theory takes place.

attractive forces between flat surfaces, which has a large influence on the producibility of a design and second, the rest position of two connected and deflected springs.

In later chapters, the energy minimum principle will be used widely. Such as in section 3.4 (concerning the material choice) and subsection 3.5.3 (dealing with the analytical model for the thermal actuator).

2.3.1 Stiction

Stiction means static-friction and describes a failure mechanism in MEMS devices when two movable parts get into contact and stick together permanently. This can happen during the fabrication (so called release-stiction) and also during the operation of the device. Wet chemical processes lead to capillary forces during the fabrication of the devices when the liquids evaporate. These forces can pull adjacent surfaces into contact to each other. A direct contact can be established also during the operation of devices due to overload shocks or high electrostatic forces [66–70].

Stiction happens when the surface energy of two separated areas is larger than the elastic energy stored in the deformed shape of the device when a contact is established. The surface energy is an intrinsic property of interfaces due to free valences.

Considering a simple model (Fig. 2.3) of two surface areas A_s , where one is fixed and the second one is attached to a spring with spring stiffness k . The surface area is zero, as long as the contact between the areas is established. Two surfaces are created when the areas are separated, holding the surface energy

$$U_{\text{surf}} = 2 \cdot A_s \cdot \gamma_s \quad , \quad (2.20)$$

with γ_s the surface energy density in J/m². An extension of the spring x is introduced, resulting in a deformation energy (elastic energy)

$$U_{\text{def}} = \frac{1}{2} \cdot kx^2 \quad , \quad (2.21)$$

stored within the linear spring. For $x = 0$, the surfaces are in contact and the spring is at rest, so that U_{surf} and U_{def} are zero. At a specific deflection $x = x_2$ the deformation energy equals the energy needed to create two separated surfaces. In accordance to the energy minimum

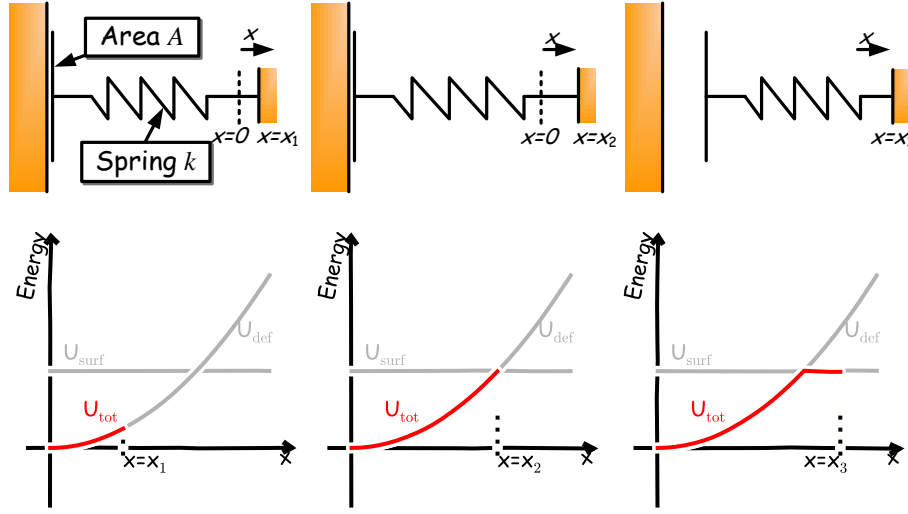


Figure 2.3: Model for stiction. The spring will be elongated progressively from the left to the right. The areas at the left will stick together until the energy in the spring equals the surface energy.

principle, any further stretch of the spring leads to a break of the bond interface, because the total energy

$$U_{\text{tot}} = U_{\text{surf}} + U_{\text{def}} \quad (2.22)$$

is lower when the surface areas are created and the energy of the spring is released.

A peel-number N_P can be defined, which indicates the probability for the occurrence of stiction. When $N_P > 1$ stiction will not become a problem. Stiction is likely to occur for peel-numbers $N_P < 1$. In the described spring model the peel-number is

$$N_P = \frac{U_{\text{def}}}{U_{\text{surf}}} = \frac{1}{4} \frac{kx^2}{\gamma_s A_s} \quad , \quad (2.23)$$

and can be avoided by increasing the stiffness k and the deformation x that is required to establish a surface contact or by decreasing the surface energy density γ_s and the contact area A_s .

2.3.2 Mechanical Deformation

Its obvious that a mechanical deformation of a structure will take place until a force equilibrium is reached. This equilibrium again is a result of the energy minimum principle stated before. The deformation energy is

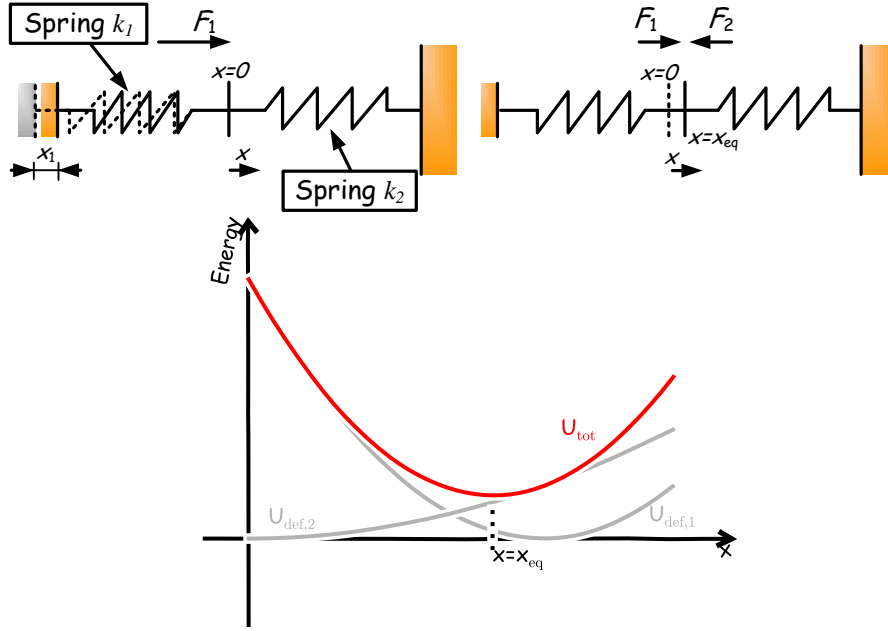


Figure 2.4: Two connected springs will push against each other, until a force equilibrium is reached and the total energy is minimal.

$$dU_{def} = Fdx \quad (2.24)$$

where F is the force in N. The energy is at an extremum when

$$\frac{dU}{dx} = F = 0 \quad (2.25)$$

The resulting force is zero when the deformation energy is in a minimum. Considering two connected springs with k_1 and k_2 , where one spring is initially elongated along the x -coordinate and the second is at rest (Fig. 2.4). The total energy of the system is therefore

$$U_{tot} = U_{def,1} + U_{def,2} = \frac{k_1 x_1^2}{2} + 0 \quad (2.26)$$

The elongated spring will try to get back into its rest position, elongating the second spring about a value of x , so the total energy becomes

$$U_{tot}(x) = U_{def,1} + U_{def,2} = \frac{k_1 (x_1 - x)^2}{2} + \frac{k_2 x^2}{2} \quad (2.27)$$

Combination with Eq. 2.25 leads to

$$\overbrace{-k_1(x_1 - x)}^{F_1} + \overbrace{k_2 x}^{F_2} = 0 \quad (2.28)$$

which is again equal to the force equilibrium $F_1 + F_2 = 0$. In this simple model, the minimization of the energy equals a force equilibrium. For more complex systems, e.g., comb drives, the force can not be calculated such easy and, therefore, the deflections have to be calculated using the overall electrical and mechanical energies [71]. ◀◀

"There is always an easy solution to every human problem - neat, plausible, and wrong."

H.L. Mencken
1917

"No real problem has a solution."

Smith's Law

3 Design or Limitation of the Diversity of Solutions

FOR every technical problem there is a wide variety of solutions. This diversity can be limited by defining boundary conditions for the given problem. But even then, there is aplenty of possible solutions. Hence, a rough breakdown and review for different approaches has to be made in order to compare the strengths and weaknesses. Afterwards, the most promising approach is chosen and the details are clarified. The way of finding a solution is often an iterative one and at some point, one can see that there is no ultimate solution, because every benefit has its own very special drawbacks.

This chapter summarizes the boundary conditions for the thermal threshold sensor, the design approaches, and a promising design with a corresponding analytical model.

3.1 Definition of the Problem

A temperature threshold sensor has to be developed that remembers if a specified upper threshold temperature is reached. The whole sensor device consists of the temperature transducer element, an electronic readout, an electrical circuit and an RFID antenna. The idea is to apply the sensor to a reefer cargo and to check if the temperature has exceeded a specific limit during transportation and storage due to insufficient han-

dling or cooling failures. The state of the cargo can be checked by an RFID transponder. At first, energy is contactlessly transferred from an RFID reader to the sensor to wake up the electronics. The state of the sensor is checked with an electrical circuit and the RFID part transmits the answer to the reader. In between those checks, the device operates completely passively. The presented work focuses on the temperature measuring element.

3.1.1 Boundary Conditions

The boundary conditions for such a temperature sensing element are:

- Passive operation.
- Temperature range from $+50^{\circ}\text{C}$ down to -40°C .
- Activation at low storage temperatures.
- Easy readout.
- Small spatial dimensions.
- Robustness.
- Self check ability.

The functionality of the sensor has to be completely passive. The sensor has to track constantly the temperature and must remember a temperature that exceeds a specific threshold. Hence, an inherent physical material property has to be exploited for measuring the temperature. The sensor has to keep its functionality in a temperature range from $+50^{\circ}\text{C}$ down to -40°C . It should be inactive until it is applied to the cooled reefer cargo (until a specific lower temperature boundary is reached). The sensor is manufactured at room temperature and should be activated when it is applied to the cooled cargo. It has to remember a threshold temperature that is commonly somewhere between the manufacturing temperature and the activation temperature. Since the total energy transmitted and stored in the sensor device is limited, an easy electrical readout is preferred. The dimensions of the transducer element have to be small for a simple combination with the RFID parts. Additionally, a reduced size enhances the usability when applied to small sized cargo packages. Also, the total costs of the product are minimized

because the spatial volume used for MEMS devices is directly proportional to their fabrication costs.

Furthermore, the sensor has to be robust with respect to mechanical shocks. The transportation of cargo can be rough and the sensor has to withstand accidental dropping of the cargo. Moreover, stiction is a common problem during MEMS fabrication when movable parts are pulled into contact to each other due to caterpillar forces or mechanical shocks. Thus, the sensor has to be stiff enough to reduce the probability for such failures. A self check ability is desired to prove the state of the sensor and to increase the reliability of the whole device.

3.1.2 Proposed Solution

A thermal actuator exploiting the difference in the thermal expansion of a device and a substrate material can operate completely passively. Thermal actuators achieve displacements, only by relying on temperature changes of the surrounding environment and the thermal expansion of the material. These displacements can be used to trigger a latch mechanism, which can be designed to be activated at lower temperatures and to remember the exceeding of a specific threshold temperature. The basic idea for the given problem is the use of two latch mechanisms. At first, a mechanical deflection due to shrinking of a material at decreasing temperatures activates the first latch mechanism. At this point, the sensor is put into operation. When the temperature is raised again, the expansion pushes against the already triggered latch, which activates itself another latch mechanism. When this second latch mechanism is triggered, it gets struck irreversibly, jamming further movements. The state of the sensor can be checked with help of an electrical resistance measurement. The resistance between the second latch and its counterpart is high if there is no electrical contact and is only limited by leak currents between the two separated leads. Once the second irreversible latch-contact is established, a short circuit is created and the resistance changes by several orders of magnitude. Fig. 3.1 depicts the schematic operating principle of the proposed latch mechanisms.

3.2 Thermal Actuator

A properly designed thermal actuator is essential for the proposed solution. On the one hand, it has to be compact and small, and on the other hand, it has to exhibit deflections in the range of several tens of

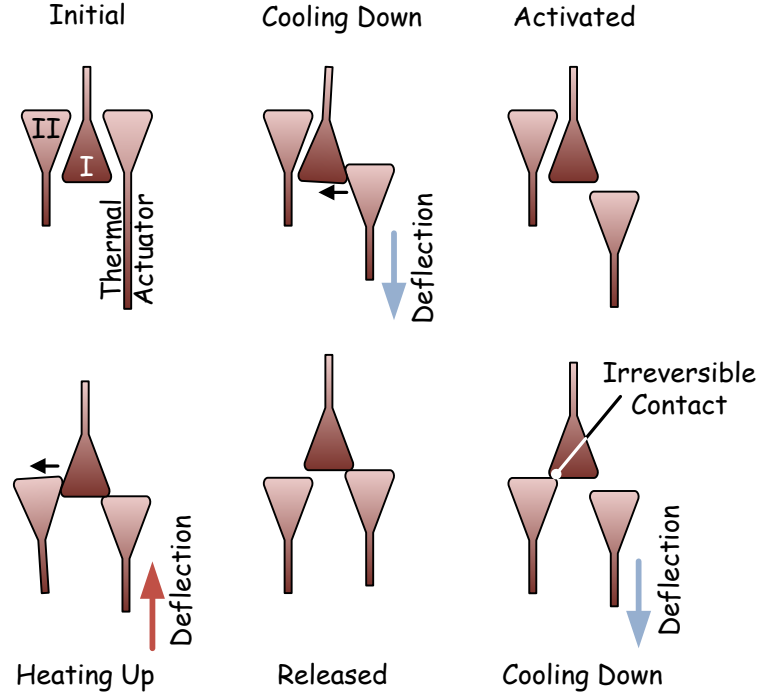


Figure 3.1: The proposed solution compose of a thermal actuator and two latch mechanisms. The first latch is triggered during cooling down the device. upon reaching an upper threshold temperature, the second mechanism is activated. This leads to an irreversible electrical contact that can be measured via electrical resistance measurements.

micrometers. Both aims are opposite objectives. The deflections can be increased, by enlarging the dimensions of the structure. An optimum between these contrary objectives has to be found. Large deflections are needed due to the minimum gap sizes between the latch mechanisms. These gaps are defined by the manufacturing process and the aspect ratios. The gap sizes are in the range of several microns for state of the art micro machining technologies. Hence, the deflection has to overcome at least those gaps for a temperature range of a few tens of °C. When the gap is estimated to be $10\text{ }\mu\text{m}$ and the temperature difference of 20 K is taken into account, the actuator has to exhibit a sensitivity of at least $0.5\text{ }\mu\text{m/K}$. In addition, it has to achieve forces in the order of mN to overcome the friction between the latch and its counterpart. The most promising design relies on V-shaped beams. But since single stage V-shaped beams only exhibit thermal sensitivities of up to $0.1\text{ }\mu\text{m/K}$, cascaded designs and designs with lever transmissions are investigated.

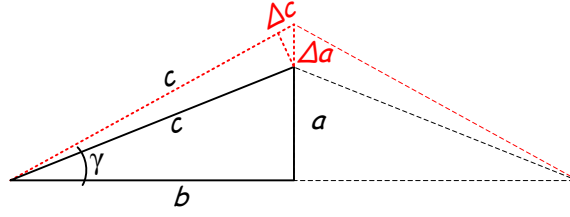


Figure 3.2: The change in length Δa is large for flat triangles with small angles γ .

3.2.1 Design Considerations

The V-shaped beam results from simple triangle mathematics. When one arm of the V-shaped beam is identified with the hypotenuse c of a rectangular triangle (Fig. 3.2) and the beam becomes longer about Δc due to thermal expansion while the adjacent b is fixed, the change in length of the opposite a becomes

$$\Delta a = \sqrt{c^2 (1 + \alpha \Delta T)^2 - b^2} - a \quad . \quad (3.1)$$

Here, α is the coefficient of thermal expansion (CTE) and ΔT the temperature change. For a flat triangle with a small angle γ , Δa becomes large in respect to a temperature change (Fig. 3.2). This basic consideration assumes a hinge condition in the interconnection of the beams, but does not take into account that not only a deflection but also a force must be applied on the tip of the triangle. Nevertheless, this model is sufficient for a generic actuator design. The deflection Δa can be increased by a transmission, e.g., a cascaded triangle or a lever beam. These two basic designs are depicted in Fig. 3.3.

The thermally induced energy has to be efficiently transformed into mechanical work. The product of force and displacement at the tip of the structures is a measure for the work the structure can provide. Basically, a large deflection is needed for actuation, but the resulting force has also to be kept in mind. It has to be sufficiently large to push against the latch mechanism that exhibits a specific spring stiffness and friction, once a contact is established with its counterpart.

The primary V-shaped beam is stacked in parallel several times to increase the thermally induced energy. Also the beam width of the V-shaped beams has to be large to increase the total work provided by the actuator. The transformation into mechanical work has to be effi-

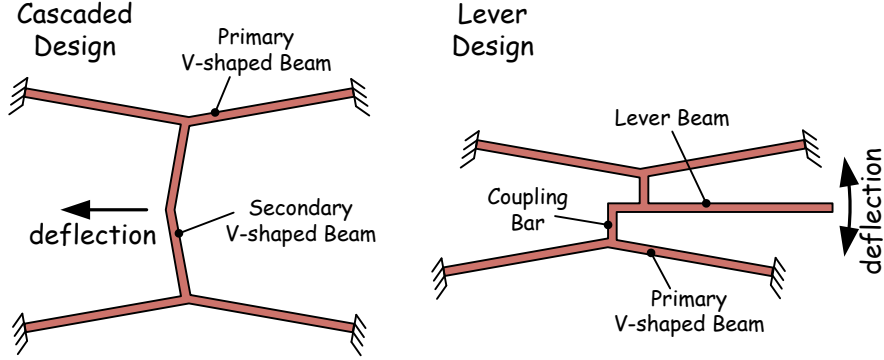


Figure 3.3: The generic developed designs rely on V-shaped beams. The deflection can be increased by either a cascaded V-shaped beam or a lever transmission.

cient with low energy losses. These losses arise from the elastic energy of the deformation of the structure. The elastic deformation energy is proportional to the mechanical stress within the material. Care must be taken that the yield strength of the material is not exceeded. Otherwise, there will be plastic deformations that leads to a non-linear behavior of the device. Consequently, reducing the stress within the structure will help to avoid plastic deformations and to reduce the energy loss. The occurring mechanical stress of a deformed structure can be described by a simple model of a single clamped beam featuring a height h , a width b , a length l , and a deflection d . The maximal momentum is given by $M = \frac{3Eb^3h}{12} \frac{d}{l^2}$ and the elastic section modulus by $S_A = \frac{hb^2}{6}$. Hence, the occurring mechanical stress is calculated to be

$$\sigma_{\text{mech}} = \frac{M}{S_A} = \frac{3}{2} \frac{E \cdot d}{l^2} b \quad , \quad (3.2)$$

where E is the Young's modulus of the material. It is assumed that the neutral axis is equal to the symmetry plane of the rectangular beam shape for simplification of the calculations. The corresponding elastic deformation energy is calculated to be

$$U_{\text{def}} = \frac{1}{2} k d^2 = \frac{E}{8} \frac{h \cdot d^2}{l^3} b^3 \quad , \quad (3.3)$$

where k is the spring stiffness of the cantilever, given by $k = \frac{Ehb^3}{4l^3}$. The mechanical stress can be reduced by scaling the width of the beam, which is in contrast to maximizing the induced thermal energy. Quasi-hinges with a reduced beam width are designed and implemented in the most

affected regions, such as: the connections of the beams and the coupling bars to the lever. But the width of the hinge beam has to be sufficient to withstand the compressive forces. Buckling occurs in the worst case, resulting in a loss of the functionality of the actuator. The design is always a trade-off between mechanical stress, displacement, and force. Finite element model simulations are carried out to optimize the generic designs. These simulations are explained in detail in subsection 3.2.2.

Topology Optimization

Aside from generic and analytic designs, the concept of topology optimization was utilized [72–74]. This concept was presented in [75] for optimizing thermally activated micro grippers, demonstrating the usability of the method for thermo-mechanical problems. Topological optimization is the optimization of an area with regard to a requested extreme of an output value. In context of the presented work, topology can be reduced to a general structure geometry that fits within a well defined area.

Two regions are defined for the design optimization. One is the optimization area that has to be adapted and formed and the second one provides the feedback for the evaluation algorithm (Fig. 3.4). The optimization process involves a specific value, which has to be maximized or minimized. A structure should be generated within the boundaries of the optimization area. It should exhibit a maximum in-plane deflection or force at a specific point when the temperature is changed and thermal stress is induced within this area. The energy or work (force-displacement product) that can be applied against a spring is chosen as control value and should be maximized.

The topology optimization toolbox of COMSOL Multiphysics® provides a solver and an iteration algorithm for such optimization problems. The area which needs to be optimized has two fixed boundaries. One boundary is modeled with a roller bearing condition which represents a symmetry axis for the resulting structure (Fig. 3.4). The Young's modulus $E(x, y)$ in each point in the area is defined as

$$E(x, y) = E_0 \cdot \rho_o(x, y)^p \quad , \quad (3.4)$$

where $\rho_o(x, y)$ is the optimization parameter ($\rho_o(x, y) \in [0, 1]$), p the penalization parameter ($p = 3$), and E_0 the Young's modulus of the material ($E_0 = 210 \text{ GPa}$). The area should induce a maximum elastic energy

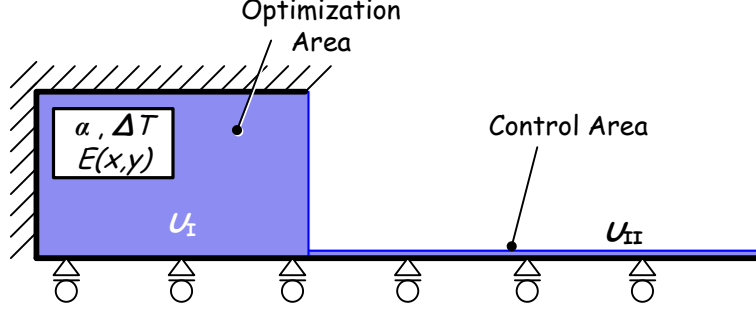


Figure 3.4: Simulation model for the topology optimization with the defined areas and the boundary conditions. The narrow area is the control area which provides the control variable for iteration algorithm. The optimization area defines the area in which the Young's modulus is adapted to built up the optimized geometry.

in the control area, which is modeled as a narrow beam. The Young's modulus in this control area is $E_C = 1$ GPa and small compared to E_0 . A thermal stress σ_{therm} is induced in the optimization area by applying a thermal expansion and a temperature change. This stress should be converted to an in-plane deflection, pushing against the control area. Therefore, the energy difference $U_{\min} = U_I - U_{II}$ between the elastic energy of the optimization area U_I and the elastic energy of the control area U_{II} is used as control value for the optimization algorithm. The elastic energy of the control area equals the thermally induced elastic energy of optimization area when the energy difference is at a minimum. Due to the low Young's modulus of the control area, the elastic energy is high when the deformation (compression) of the control area is large. This means that the deflection is large at the point where the optimization area is connected to the control area.

The optimization parameter ρ_o in each point within the optimization area is varied in order to reduce U_{\min} during the iteration process. This leads to areas where the Young's modulus is either zero or E_0 . The penalization parameter suppresses areas with an intermediate Young's modulus. Figure 3.5 shows the evolution over time of the optimization process and how the resulting structure is formed. The basic, rudimentary, and replicated structures that can be found are triangles, pushing against other triangle geometries (Fig. 3.6). These geometries can be identified as beams with a non-linear width. The single beams are broad

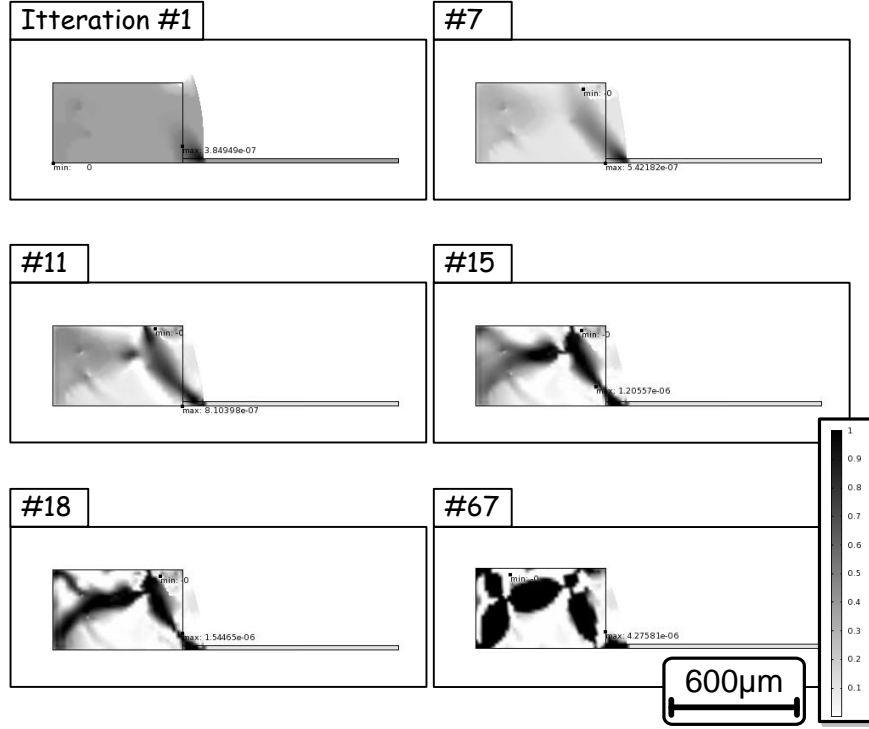


Figure 3.5: Iteration steps of the simulation for optimizing the topology of the structure. The optimization parameter ρ_o is plotted after iteration step 1, 7, 11, 15, 18, and 67, respectively. In the beginning, the optimization parameter is homogeneously distributed and set to 0.1. In each individual step, the parameter is adjusted to meet the optimization goal. In the shown case, the elastic energy difference between the control area and the optimization area should become minimal.

in the middle and small at the interconnections. In this way, the elastic energy output is increased, while the losses due to bending deformations in the hinges are decreased.

The stability of the solution of the simulation is sensitive to the chosen initial and boundary conditions, such as:

- Initial optimization parameter
- Upper and lower boundary for the optimization parameter
- Maximum occupied area of the resulting structure

These parameters were found by a trial and error approach. The initially homogeneously distributed optimization parameter is the starting point

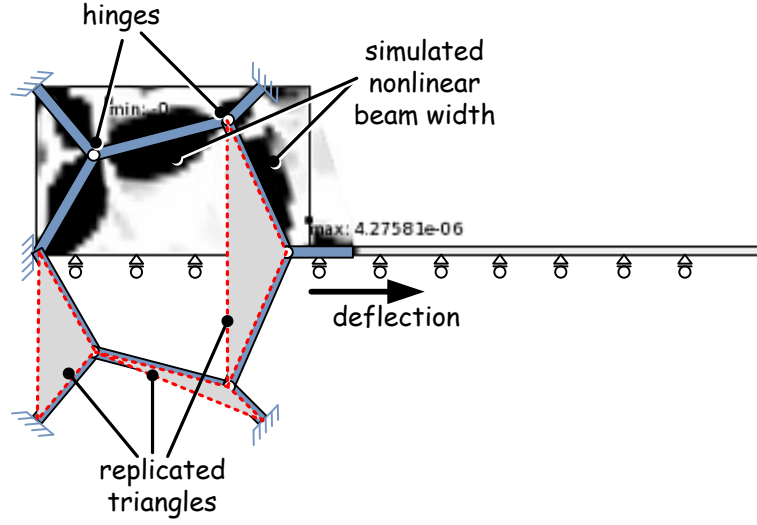


Figure 3.6: The resulting structure features beams with a non-linear width and only narrow interconnections between the beams. The design is approximated by linear beams and hinges with a small width. A rudimentary, basic triangle structure can be identified that pushes against other triangles to convert the thermally induced stress into an in-plane deflection.

Young's modulus	E_0	200 GPa
Young's modulus	E_C	1 GPa
CTE	α	16.5 ppm/K
Poisson's ratio	ν	0.33
Temperature difference	ΔT	60 K
Initial $\rho_o(x, y)$	ρ_{ini}	0.1
Occupied area max	A_{fill}	16%
Optimization area	A_{opt}	600x370 μm^2
Lower boundary		1e-4
Upper boundary		1

Table 3.1: Parameters used for the topology optimization.

for the simulation. The upper boundary for the optimization parameter is 1. When the lower boundary is set to zero, the simulation becomes unstable and, hence, 10^{-4} is chosen as lower boundary. The maximum occupied area of the resulting structure is the area that the structure is allowed to cover (percent of the total optimization area). The parameters used in this simulation are listed in Tab. 3.1.

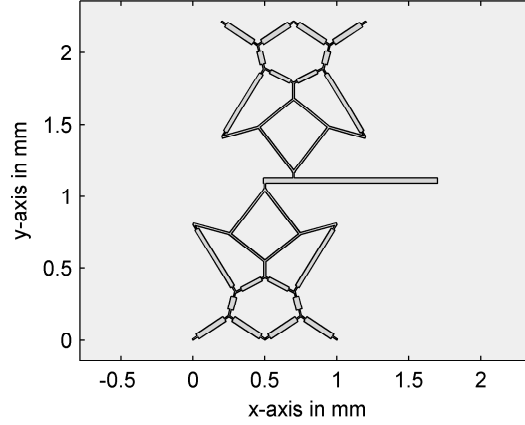


Figure 3.7: A thermal actuator based on the approximated geometry resulting from topology optimization. Two actuators are placed facing each other, connected to a lever, which moves up- and down in accordance to temperature changes.

The resulting structure is approximated by linear beams (Fig. 3.6) to obtain a geometry that can be mapped onto a lithography mask. The hinges for the interconnections between the beams are approximated by narrow beams. Based on the approximated structure, a thermal actuator is designed. Two of them are arranged facing each other with a small offset, connected to a lever which increases the thermally induced deflections. A sample geometry is plotted in Fig. 3.7. The whole actuator is created by a Matlab® script and automatically simulated regarding the thermo-mechanical behavior using COMSOL Multiphysics®. The design is manually adapted to decrease the arising stress and to increase the work that the actuator can provide.

3.2.2 Finite Element Model Simulation

Finite Element Model (FEM) simulations are carried out to predict the behavior of the designs. The geometries are parametrized created with Matlab®, which offers an interface to COMSOL Multiphysics®. The parameters in the simulations were varied to find optimal designs regarding the deflections, the forces, and the mechanical stresses.

The structures are modeled as 2D plain-strain geometries, including a thermal expansion of the material and an initial stress resulting from the manufacturing of the devices. The plain-strain condition means that the strain in z -direction (perpendicular to the 2D-plane) is zero. A nonlinear

simulation mode is chosen because the deflections cannot be considered to be small compared to the width of the beams. This condition takes into account stress and strain effects of second order and instead of the linear strain and stress the Green¹ strain and Piola²-Kirchhoff³ stress are used. The mechanical deformation is linked to a moving mesh application. The boundaries of the anchors are fixed, whereas the rest is free moveable. The simulation is carried out in two steps to simulate the deflection and the force at the tip of the structures. At first, the geometry is simulated at a specific temperature difference including the thermal expansion and also the intrinsic stress. This leads to the deflection d_{\max} of the tip at elevated temperatures. The maximum occurring von Mises⁴ stress is evaluated by searching for the maximum stress within the geometry [76]. In the next step, the temperature difference is removed and only the deformation of the structure due to the intrinsic stress d_{intr} is evaluated. The deflection sensitivity per Kelvin is calculated to be

$$d_K = \frac{d_{\max} - d_{\text{intr}}}{\Delta T} \quad , \quad (3.5)$$

with ΔT the temperature difference. With the moving mesh application a new geometry is created that results of the simulated deformed shape. Subsequently, the intrinsic stress is removed because the structure is already deformed due to this stress. The tip of the structure is fixed and a temperature difference is applied again. The reaction force at the tip is evaluated and the force per Kelvin F_K can be computed when the deflection of the tip is restricted. The product of deflection and force is a measure for the work that a structure can provide against a spring. Figure 3.8 depicts the boundary conditions and the simulation sequence for a typical design.

Design Evaluation

Different geometries and design approaches are simulated and the deflections and forces are evaluated. The occurring maximum stress is not evaluated in these simulations because only a rough estimation of the performance of the different design approaches is relevant at this point. Nevertheless, after finding the most promising design regarding the overall performance evaluating the technology to manufacture the devices,

¹George Green, British mathematician and physicist, 1793-1841.

²Gabrio Piola, Italian mathematician and physicist, 1794-1850.

³Gustav Kirchhoff, German physicist, 1824-1887.

⁴Richard Edler von Mises, Austrian mathematician, 1883-1953.

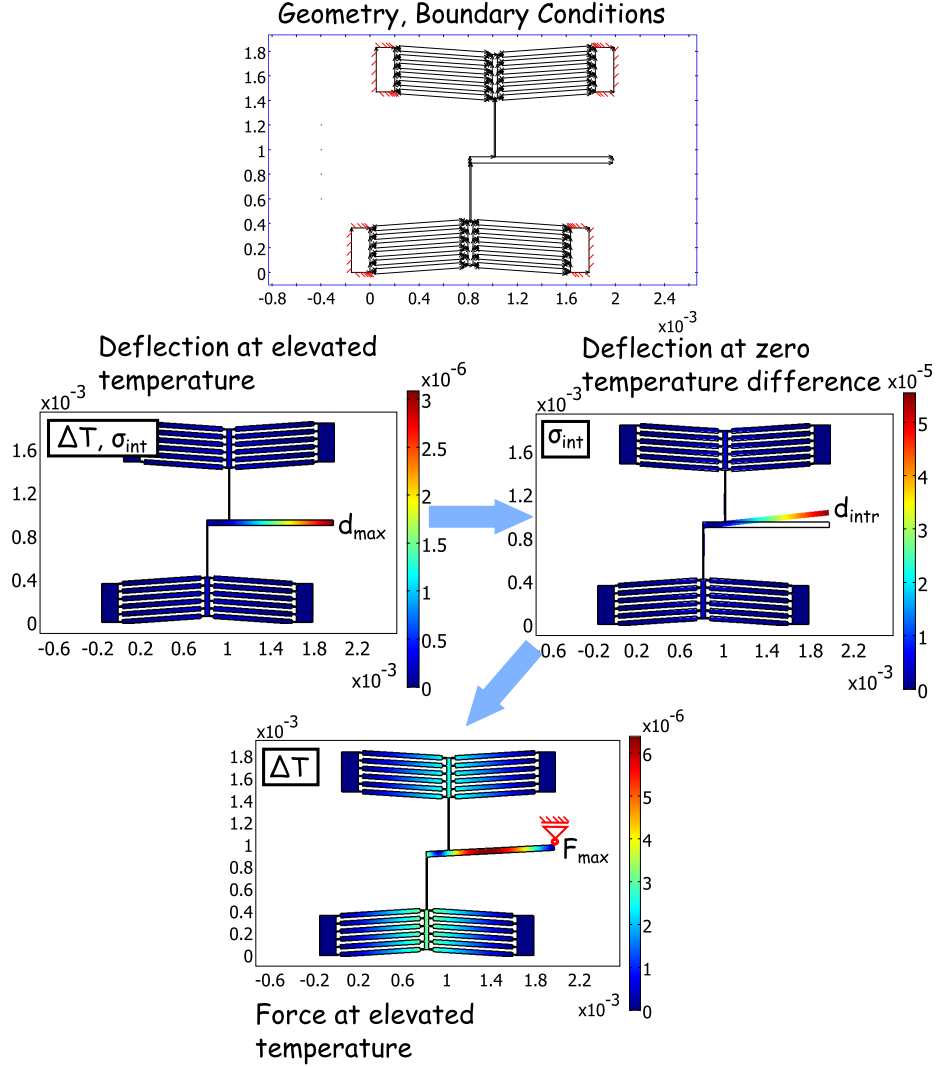


Figure 3.8: FEM simulations to predict the behavior of the structures. The boundaries of the anchor regions are fixed, whereas the rest of the structure is free. The deflection and intrinsic stress are evaluated at raised temperatures. Subsequently, the temperature difference is set to zero, leading to the deformation caused by the intrinsic stress that is in the same order than the thermally induced deflection. Hence, the deflection due to increased temperature and the intrinsic stress nearly cancel out each other. A new geometry is created resulting from the deformed shape. The tip of the structure is fixed and the reaction force is evaluated at increased temperatures.

the geometries need to be adapted regarding the initial intrinsic stress as well as the maximum occurring stress.

The geometric parameters of the structures (e.g., length and width of the beams, offset between the mirrored V-shaped beam stacks, etc.) are varied to find an optimum between deflection and force. This multi-parameter problem is solved by a manual iteration process. At first, the most obvious parameters are adjusted, such as the angle of the primary V-shaped beams and the offset between the stacks for both, the generic, (Fig. 3.3) and the topology optimization designs (Fig. 3.6). The parameters promising the best performance are taken and the next geometric parameter is adjusted. In this way all geometry parameters are tested. The iteration is carried out 2-3 times until no more significant increase in performance is achieved. This manual approach has the risk to run into a local minimum, but there is no simple way to handle such multi-parameter optimization problems in general. Several different initial starting parameters are tested and iterated to reduce the risk of running into local minimum.

To compare the different designs, a Young's modulus of $E = 200$ GPa, a CTE of $\alpha = 16.5$ ppm/K, a Poisson's⁵ ratio of $\nu = 0.33$, and a temperature difference of $\Delta T = 40$ K are assumed. Also the total occupied area, defined by a rectangular shape enveloping the whole structure, is considered to provide an additional decision criteria and to find the best design for the given problem (large deflection, low area consumption, sufficient force to push a latch mechanism). Table 3.2 summarizes the simulated deflections, forces, and occupied areas of different manually optimized designs. The product of deflection d and force F at the tip of the structure is a measure for the work and the area specific work $d \cdot F/A$ measures the efficiency of the actuator per required area. The dimensions of the structures can be scaled to increase the force-displacement product, but this is in contrast to the requirements of a small spatial volume for the whole device. Two representative designs for each of the topology optimized, the cascaded V-shaped beam, and the V-shaped beam geometries with a lever transmission are compared. The cascaded V-shaped beam structures feature the lowest maximum deflections, but the highest forces. Due to the cascaded design there is plenty of unused space between the mirrored beam stacks which require relatively large areas compared to other design approaches. The topology opti-

⁵Siméon Denis Poisson, French mathematician, geometer, and physicist, 1781-1840.

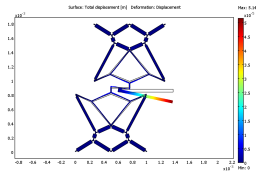
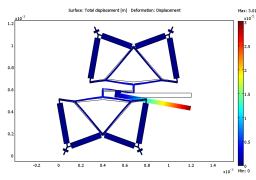
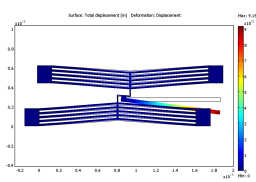
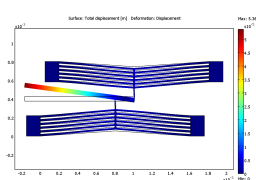
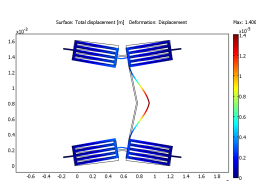
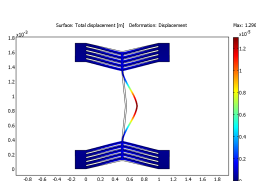
Design	d μm	F mN	Area A mm^2		$d \cdot F$ nJ	$d \cdot F / A$ nJ/mm^2
	51	1.3	1.4×1.8	2.52	66.3	26.3
	30	1.0	1.2×1.2	1.44	30.0	20.8
	91	1.8	1.7×0.6	1.02	163.8	160.6
	54	3.3	1.8×0.8	1.44	178.2	123.8
	16	5.9	1.6×1.6	2.56	94.4	36.9
	14	14	1.4×1.8	2.52	196.0	77.8

Table 3.2: Different designs are compared regarding the simulated deflections, forces, and required areas. The simulations are carried out for $E = 200 \text{ GPa}$, $\alpha = 16.5 \text{ ppm/K}$, $\nu = 0.33$, and $\Delta T = 40 \text{ K}$.

mized geometries exhibits the lowest force-displacement product. They also require a lot of chip area and the area specific work $d \cdot F/A$ is the lowest of the compared geometries. One big benefit is their robustness against out-of-plane deformation which is due to the distributed anchor points (see also Fig. 3.6). The V-shaped beams with lever transmission promise the best performance for the thermal micro actuator. The trade-off between force and displacement can be easily adjusted by changing the lever transmission. Very high displacements can be achieved at the expense of force. This structures can also be designed to be very compact resulting in a large area specific work. Therefore, these geometries are investigated in detail including an analytical model (sec. 3.5). Finally, they are used as actuators in the prototype devices. The evaluation of the manufacturing technology and the design iterations are established simultaneously. Hence, all of the designs are manufactured with different technological approaches and are evaluated by thermal measurements.

The designs have to be adapted in accordance to the chosen technological manufacturing approach. Young's modulus, CTE, and intrinsic stress vary for different materials and technologies and these parameters have a significant influence on the behavior of the structures. The Young's modulus is directly proportional to the occurring stress and the force the actuator can provide. The CTE influences the thermally induced energy and output work. The intrinsic stress leads to an initial deformation. In the case of SU-8 technology, this deformation significantly changes the angle of the primary V-shaped beams, so that the angle in the proposed design has to be larger. The initial deflection due to this stress influences the offset for the latch mechanism. When the latch mechanism has to be activated at a specific temperature, the offset has to be accordingly considered.

3.3 Latch Mechanism

A latch mechanism is needed as part of the sensing element to remember if the threshold temperature was exceeded. The latches are triggered by the thermal actuator and a schematic design is depicted in Fig. 3.9. The latch is inactive at first (during fabrication) and activated when the lower threshold temperature is reached. When the device is heated up again, the actuator pushes against the latch until an upper threshold temperature is exceeded. At this point, a second latch is triggered which establishes a mechanical contact that irreversibly blocks further movements. The displacement sensitivity of the actuator and the required

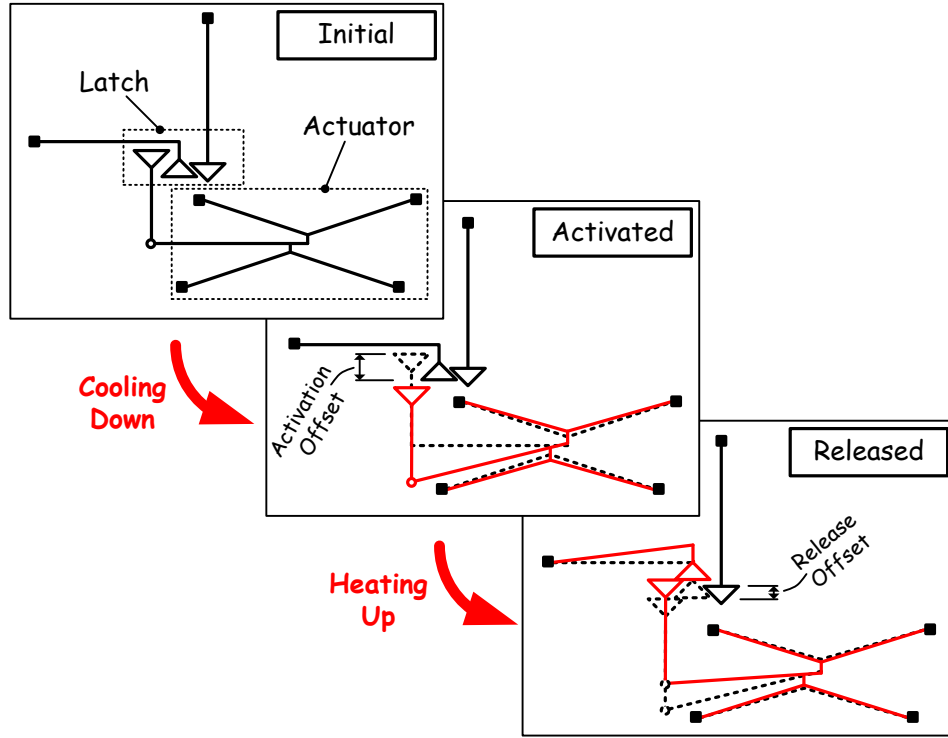


Figure 3.9: Functional principle of the mechanical transducer element. When the temperature decreases, the tip of the actuator moves down and activates a latch. When the temperature is raised again, the actuator pushes against the latch, until it is released and an irreversible contact is established.

activation temperature defines the offsets between the latches. The minimum offset is given by the minimum aspect ratio of the manufacturing process.

The maximum actuated deflection of the latch depends on the deformation energy of the actuator and the latch. For a well defined temperature and zero deflection $d = 0$, the force of the actuator equals F_0 . The actuator can be considered as a spring with stiffness k_{act} and the resulting energy of the actuator is thus calculated to be

$$U_{\text{act}} = -F_0 d + \frac{k_{\text{act}} d^2}{2} \quad . \quad (3.6)$$

Therefore, the maximum deflection d_{max} is reached when U_{act} is minimal. When pushing against a latch mechanism with a spring stiffness k_{latch} ,

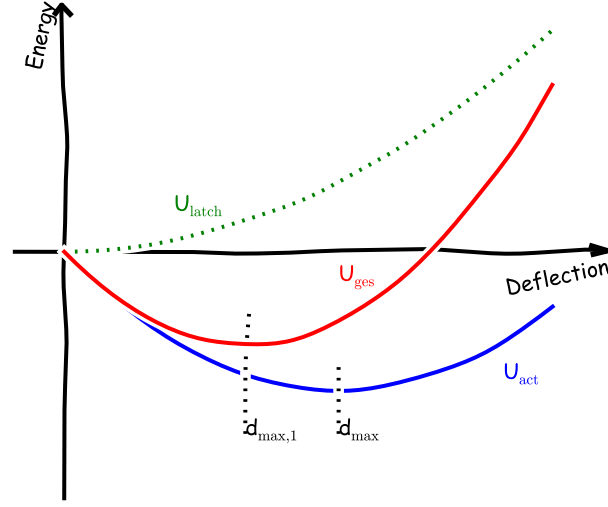


Figure 3.10: Energy of the thermal actuator as a function of the deflection. The maximum deflection is reduced to $d_{\max,1}$ when the actuator pushes against the latch mechanism, assuming that the actuator is in contact to the latch right from the start. In this model, the initial offset between actuator and latch is neglected, as it appears in a real geometry.

the total energy is calculated to be

$$U_{\text{ges}} = U_{\text{act}} + U_{\text{latch}} = -F_0 d + \frac{k_{\text{act}} d^2}{2} + \frac{k_{\text{latch}} d^2}{2} \quad . \quad (3.7)$$

This model assumes that the actuator and the latch are already in contact to each other, neglecting the initial offset between them as it appears for a real device. The maximum deflection is accordingly reduced to $d_{\max,1}$, as depicted in Fig. 3.10. The corresponding force is a function of d as well and given by

$$F(d) = -\frac{dU_{\text{ges}}}{dd} = F_0 - (k_{\text{act}} + k_{\text{latch}}) d \quad . \quad (3.8)$$

Hence, the spring stiffness of the mechanism has to be small in order to reduce the reaction force pushing against the actuator. From a different point of view, a more flexible mechanism reduces the loss of energy due to the deformation. When the occurring deformation energy of the latch mechanism is reduced, the actuated maximum displacement is increased.

Two different approaches for the basic latching geometry are investigated in detail regarding the contribution of the friction to the total energy.

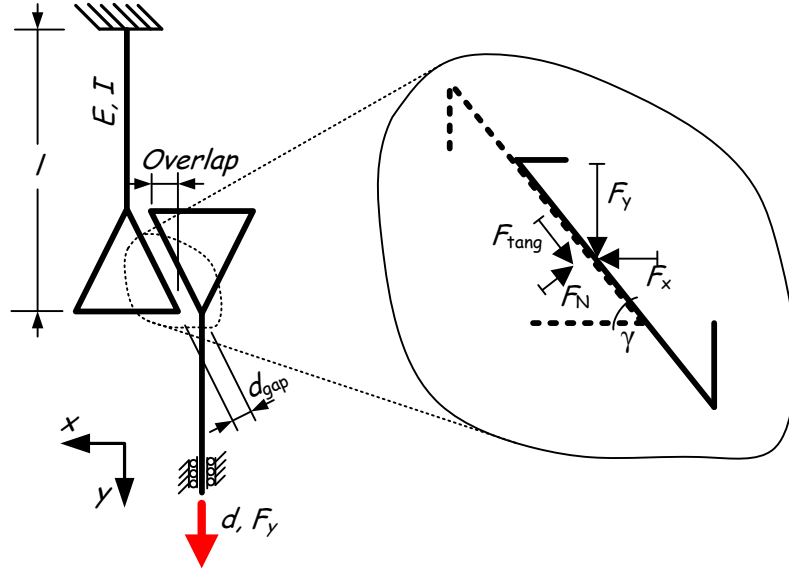


Figure 3.11: Schematic of a triangular shaped latch mechanism. The right part is fixed to the thermal actuator which causes a force F_y and a deflection d . The left part is fixed onto a beam that is clamped on one end.

3.3.1 Triangle Shaped Latch

The friction of the material has to be overcome in order for both parts to slide along each other. For a triangle shaped latch (Fig. 3.11) with an angle γ and a coefficient of friction (CoF) μ_0 , the tangential force F_{tang} has to be larger than the friction force resulting from the contact force F_N . The tangential force results from the pushing force of the thermal actuator and the angle of the triangle

$$F_{\text{tang}} = \sin(\gamma) F_y - \cos(\gamma) F_x - \mu_0 [\cos(\gamma) F_y + \sin(\gamma) F_x] \quad , \quad (3.9)$$

where the index x and y corresponds to the lateral component (see Fig. 3.11). In the simple case where the latch is fixed onto a beam that is clamped on one end, the force F_x can be calculated to be

$$F_x = \frac{3EI}{l^3} \frac{d}{\tan(\gamma)} \quad . \quad (3.10)$$

Here l , I , and E are the beam's length, second momentum of inertia and Young's modulus, respectively, while d is the deflection in y -direction. When the thermal actuator, featuring a maximum deflection d_{max} and

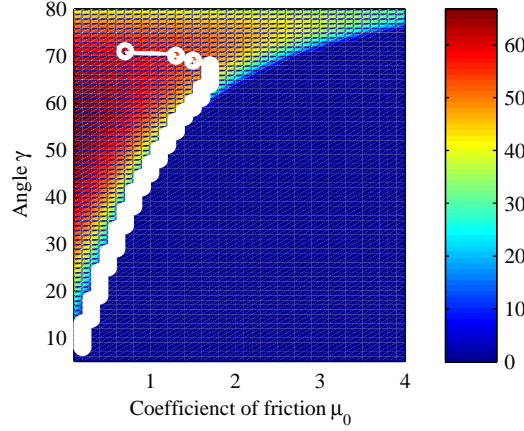


Figure 3.12: Calculation of the maximum deflection depending on the coefficient of friction and the angle. Within the marked region (white dots), the deflection is sufficient for both parts to completely pass each other when an overlap of $20\text{ }\mu\text{m}$ is assumed. The color marks the maximum deflection ranging from $0\text{ }\mu\text{m}$ (blue) to $67\text{ }\mu\text{m}$ (red).

a maximum force of F_0 , pushes against the latch, the force F_y of the actuator depends on the deflection as

$$F_y(d) = F_0 - \frac{\overbrace{F_0}^{k_{\text{act}}}}{d_{\text{max}}} \left(d + \frac{d_{\text{gap}}}{\cos(\gamma)} \right) . \quad (3.11)$$

The gap size d_{gap} corresponds to the initial gap between the latch and the actuator. The latch slides against its counterpart as long as $F_{\text{tang}} > 0$. Hence, the influence of the angle γ and the CoF μ_0 can be studied. Fig. 3.12 depicts the maximum deflection of a thermal actuator sliding against a latch depending on γ and μ_0 . The parameters $E = 210\text{ GPa}$, $I = 1667\text{ }\mu\text{m}^4$, $l = 700\text{ }\mu\text{m}$, $F_0 = 2\text{ mN}$, $d_{\text{max}} = 86\text{ }\mu\text{m}$, $d_{\text{gap}} = 8\text{ }\mu\text{m}$, and an overlap of $20\text{ }\mu\text{m}$ were used for this calculation. The deflection and force of the thermal actuator are insufficient to move against the latch for large angles and high values of μ_0 . For the given values and an angle of $\gamma = 65^\circ$ a maximum CoF of $\mu_0 = 1.7$ can be surpassed. The dots mark the region where the deflection is sufficient so that both parts of the latch can completely pass each other.

It was not distinguished between static and kinetic friction due to simplifications. The coefficient of kinetic friction is in general smaller compared to the coefficient of static friction. But in the worst case, the temperature

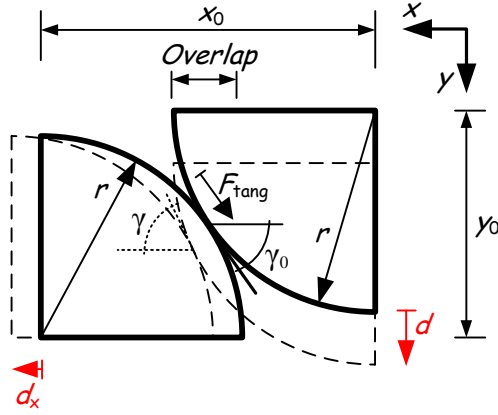


Figure 3.13: Schematic of a circular shaped latch mechanism. The tangential contact angle depends on the deflection d .

increase and, hence, the movement of the parts is very slow, resulting in a quasi static friction.

3.3.2 Circular Shaped Latch

When the same calculations are carried out for a circular shaped latch, care must be taken since the angle γ is no longer constant. Two circular shapes with radius r and an offset x_0 between the respective centers are modeled (Fig. 3.13). The thermal actuator deflects until the first contact between the curved shapes is established. The initial tangential angle is

$$\gamma_0 = \arctan\left(\frac{x_0}{y_0}\right) \quad , \quad (3.12)$$

where y_0 is the vertical distance between the center of the curves, defined by

$$y_0 = \sqrt{4r^2 - x_0^2} \quad . \quad (3.13)$$

The force of the actuator is the same as Eq. 3.11 when the initial gap d_{gap} is taken into account

$$F_y(d) = F_0 - \overbrace{\frac{F_0}{d_{\text{max}}}}^{k_{\text{act}}} \left(d + \frac{d_{\text{gap}}}{\cos(\gamma_0)} \right) \quad . \quad (3.14)$$

The perpendicular deflection of the shape d_x is calculated to be

$$d_x = \sqrt{4r^2 - (y_0 - d)^2} - x_0 \quad , \quad (3.15)$$

and the reaction force in x -direction is

$$F_x = \frac{3EI}{l^3} d_x \quad . \quad (3.16)$$

The latch moves by d_x in x -direction when the actuator deflects by d in the y -direction and the contact angle changes accordingly as

$$\gamma = \arctan\left(\frac{x_0 + d_x}{y_0 - d}\right) \quad . \quad (3.17)$$

As long as the tangential force

$$F_{\text{tang}} = \sin(\gamma) F_y - \cos(\gamma) F_x - \mu_0 [\sin(\gamma) F_x + \cos(\gamma) F_y] \quad (3.18)$$

is positive, the actuator will move on and both parts can slide along each other. The force F_x is small compared to the friction force. Hence, when an initial condition is found where $F_{\text{tang}} > 0$, both parts will slide more easily for increasing deflection d . This is due to the circular shape and the friction force that decreases with the changing angle. To obtain parameters for which the latch can slide along its counterpart, the coefficient of friction (CoF) and the lateral offset are varied. For the plot shown in Fig. 3.14, the values $E = 210 \text{ GPa}$, $I = 1667 \mu\text{m}^4$, $l = 700 \mu\text{m}$, $F_0 = 2 \text{ mN}$, $d_{\text{max}} = 86 \mu\text{m}$, $d_{\text{gap}} = 8 \mu\text{m}$, and $r = 15 \mu\text{m}$ were used. The plot indicates parameters for the overlap and the CoF where the latch can slide along its counterpart. For increasing values of μ_0 , the allowed overlap ($= 2r - x_0$) of both circular shaped geometries drops rapidly. As for the triangle shaped latch, the difference between static and kinetic friction was neglected.

3.3.3 Bistable Beam

A geometry featuring two stable configurations can also be used as latch mechanism instead of the concept depicted in Fig. 3.9. A pre-curved beam, also called bistable beam, seems natural for such an application [77–84]. By applying a force to the bistable beam, it can be pushed to snap from its primary shape into its second stable position. Since there are several buckling modes (Fig. 3.15), at least two parallel curved beams are needed to stabilize the second position. Otherwise, it would bounce back into its primary position when the force is removed. Figure 3.16 depicts an SEM image of such a geometry as well as the analytical and numerically simulated force-displacement curve. The shape w of the

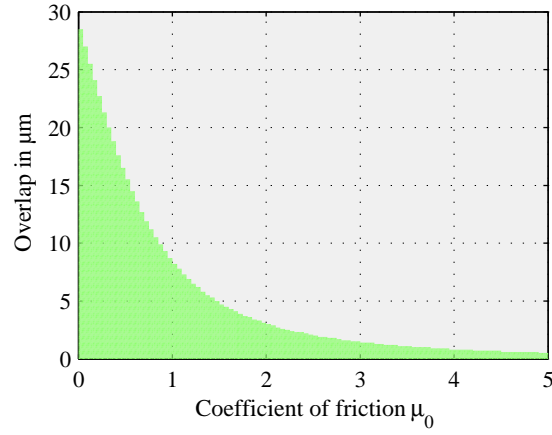


Figure 3.14: If two circular shaped geometries can slide along each other depends on the overlap of both parts and the coefficient of friction μ_0 . For increasing values of μ_0 the allowed overlap becomes smaller and smaller.

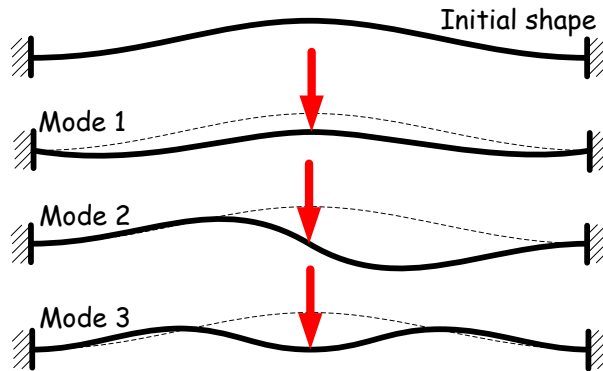


Figure 3.15: The pre-curved beam exhibits several buckling modes when a force is applied. Here, the first three modes are illustrated. The higher modes have an increasing number of nodal points.

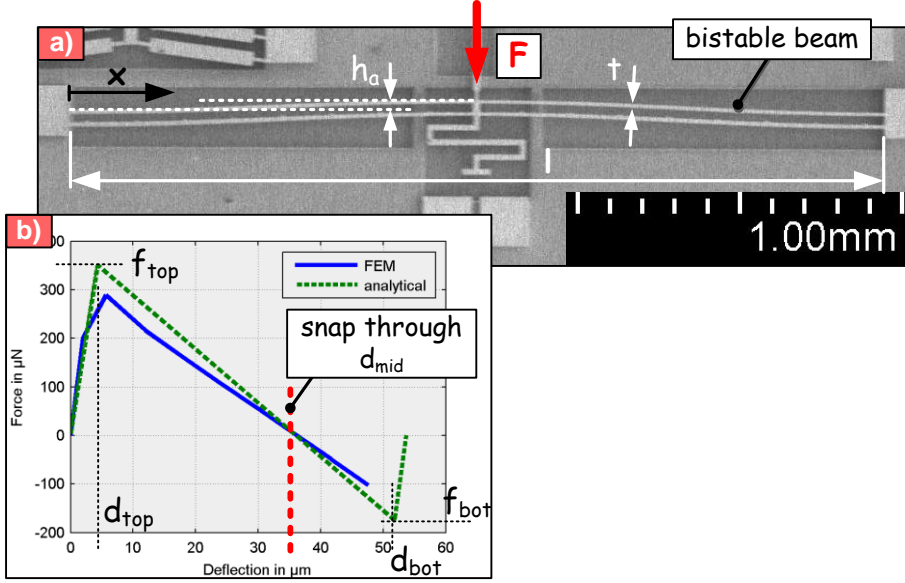


Figure 3.16: SEM micrograph of a bistable Ni beam with width t , length l and initial apex height h_a . The force-displacement curve of the shape is numerically simulated and compared to the results of an analytical model.

curved beam as a function of the elongation x is given by

$$w(x) = \frac{h_a}{2} \left(1 - \cos \left(2\pi \frac{x}{l} \right) \right) \quad , \quad (3.19)$$

with h_a as the initial apex height and l the span of the beam. An analytical model for this geometry is given in [80]. The relevant forces and displacements are calculated to be

$$f_{\text{top}} \approx 740 \frac{EI h_a}{l^3}, \quad f_{\text{bot}} \approx 370 \frac{EI h_a}{l^3}, \quad (3.20)$$

$$d_{\text{top}} \approx 0.16 h_a, \quad d_{\text{bot}} \approx 1.92 h_a, \quad d_{\text{mid}} = \frac{4}{3} h_a \quad . \quad (3.21)$$

Furthermore, the aspect ratio

$$Q_a = \frac{h_a}{t} \quad , \quad (3.22)$$

with t being the width of the beam, has to be $Q_a \geq 6$ to stabilize the second position. The minimal feature size of the chosen manufacturing

process defines the minimal width and, therefore, the apex height. The required force to push the beam into its second position is given by f_{top} and has to be smaller than the force exerted by the thermal actuator. Hence, the length l has to be chosen properly.

3.4 Choice of Material

What is a good or bad material an thermal actuator based on the thermal expansion? From an empirical point of view, the coefficient of thermal expansion (CTE) can be identified as the most relevant material parameter. In this section this empirical thesis is proved with analytic models and also the influence of other material parameters is evaluated.

The technical Hencky⁶ strain ϵ' is given by

$$d\epsilon' = \frac{dl}{l_0} \quad , \quad (3.23)$$

with l_0 the initial length and dl the differential length difference, or in the integrated form

$$\epsilon' = \ln \left(\frac{l_T}{l_0} \right) \quad . \quad (3.24)$$

The linear thermal expansion of a beam can be written as

$$\alpha \Delta T = \epsilon'_{\text{therm}} \quad . \quad (3.25)$$

The elongated length l_T due to temperature changes is

$$l_T = \exp(\alpha \Delta T) \cdot l_0 \quad , \quad (3.26)$$

with α being the coefficient of thermal expansion, and ΔT the temperature change.

To evaluate the important material parameters, a model of a cantilever that is clamped on one end was set up. The cantilever features a length l_0 , Young's modulus E , cross section Area A , a CTE α and a temperature change ΔT (Fig. 3.17). When the beam is elongated due to thermal expansion, the elastic energy U_E stored in the beam is zero. But when a force is applied and the elongated beam is compressed until the initial length l_0 is reached, the elastic energy corresponds to

$$U_E = - \int_0^{\Delta l} \epsilon'(x) \cdot E \cdot A dx \quad , \quad (3.27)$$

⁶Heinrich Hencky, German engineer, 1885-1951.

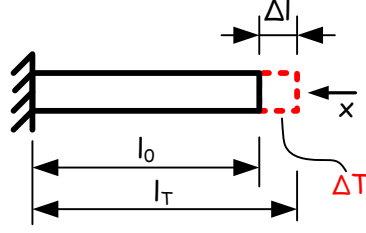


Figure 3.17: Model for determining the relevant parameters for a thermal actuator. A one sided clamped beam is heated up, elongates due to thermal expansion and is compressed until its initial length l_0 is reached. In this way the thermal energy is calculated.

with

$$\epsilon' = \ln \left(\frac{l_T - x}{l_T} \right) \quad (3.28)$$

and

$$\Delta l = l_0 - l_T = (1 - \exp(\alpha \Delta T)) \cdot l_0 \quad (3.29)$$

Substituting Eq. 3.28 and Eq. 3.29 into Eq. 3.27 and integrating leads to

$$U_E = - \left\{ (1 - 2 \cdot \exp(\alpha \Delta T)) \cdot \log \left(\frac{2 \cdot \exp(\alpha \Delta T) - 1}{\exp(\alpha \Delta T)} \right) - 1 + \exp(\alpha \Delta T) \right\} \cdot l_0 \cdot E \cdot A \quad (3.30)$$

A Taylor⁷ approximation for $\alpha \Delta T \ll 1$ results in

$$U_E = - \left\{ \left(1 - 2 \cdot \left[1 + \alpha \Delta T + \frac{(\alpha \Delta T)^2}{2} \right] \right) \cdot [\alpha \Delta T - (\alpha \Delta T)^2] - 1 + \left[1 + \alpha \Delta T + \frac{(\alpha \Delta T)^2}{2} \right] + \mathcal{O}((\alpha \Delta T)^3) \right\} \cdot l_0 \cdot E \cdot A \quad (3.31)$$

Taking into account only terms up to $(\alpha \Delta T)^2$, the elastic energy U_E stored in a beam which is heated up by ΔT and compressed to its initial length l_0 is given by

$$U_E = \frac{(\alpha \Delta T)^2}{2} \cdot l_0 \cdot E \cdot A \quad (3.32)$$

The energy depends strongly on the material parameters α^2 and E , and the design parameters A and l_0 . A material with a high product of $\alpha^2 E$

⁷Brook Taylor, British mathematician, 1685-1731.

Mat.	α 10 ⁻⁶ /K	E GPa	$E \cdot \alpha^2$ Pa/K ²	Mat.	α 10 ⁻⁶ /K	E GPa	$E \cdot \alpha^2$ Pa/K ²
SU-8	25-50	4	10.0	Mg ₂ Si	11.5	115	15.2
Al	23	70.6	37.0	Mg ₂ Ge	15	109	24.5
Pb	29.3	16.1	13.0	Mg	26	44.7	30.2
Au	14.2	78.5	15.8	Ni	13	200	33.8
Ag	19.5	82.7	31.4	Si ₃ N ₄	10	205	20.5
Ti	10.8	120.2	14.0	Brass	20.3	100	41.2
Sn	26.7	49.9	35.6	Fe	11.7	205	28
W	4.5	411	8.3	Cs	97	1.7	16
Zn	26.3	104.5	35.6	Na	71	10	50
ZnO	5	30-250	0.8-6.3	K	83.3		
Si	2.5	170	1	CuGe ₂ P ₃	37.6		
Cu	17	129.8	37.5	AgI	-2.5		

Table 3.3: Overview about the CTE and the Young's modulus of selected materials [85, 86].

is recommended to increase the elastic energy, which is a measure for the work the actuator can provide. Tab. 3.3 summarizes the CTE and the Young's modulus of different materials. Most of them are not suitable for fabrication, they are either unstable (e.g., easily oxidize or corrode), need special environmental conditions (e.g., Na, Mg) or they are way too expensive (Ag). Nickel and copper are well known in the fabrication of MEMS and can be deposited in reliable structure heights. Copper, however, has a low dislocation energy and recrystallizes when mechanical stress is applied. Therefore, its long term stability is questionable, especially at elevated temperature. Thus, nickel is left as the most preferred material though when it has a relatively low α .

3.5 Analytical Model

An analytical model for the deflection of the tip of the actuator is set up. Only an analytical model for the V-shaped beams with a lever transmission is carried out, because these structures are used for the resulting final prototype.

The geometry is separated into the V-shaped beam stack and the lever transmission. The spring stiffnesses k_V and k_L of a single beam of the stack and the lever transmission, respectively, are calculated for a given

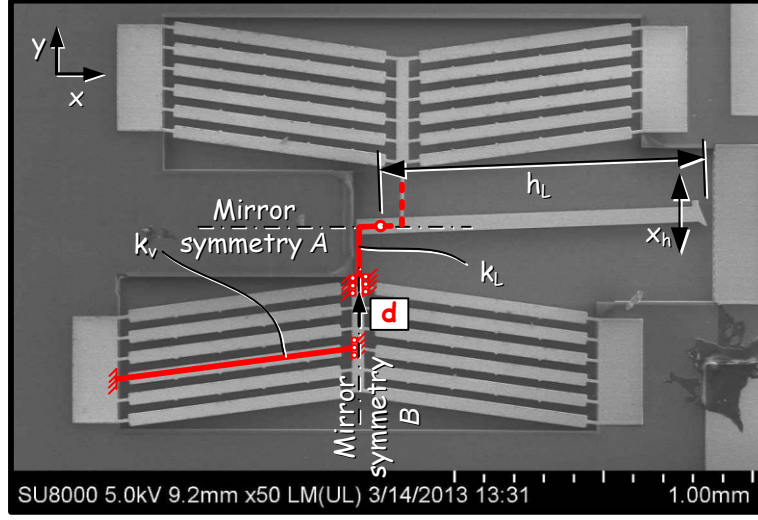


Figure 3.18: Scanning electron micrograph of the actuator. For the analytical model, the structure is separated into V-shaped beam stacks and a lever transmission with the spring stiffnesses k_v, k_L , respectively.

deflection d (Fig. 3.18). Finally, the energy equilibrium of to thermally induced elastic energy and the deformation energy due to the deflection of the structure is calculated, yielding the temperature dependent deflection of the V-shaped beam stack. With the length of the lever h_L , the deflection x_h of the tip of the actuator is calculated.

3.5.1 Spring Stiffness of the Lever Transmission

The deflection of the lever transmission is calculated with the static Euler⁸-Bernoulli⁹ beam theory

$$w(x)'' = -\frac{M(x)}{EI} \quad , \quad (3.33)$$

with w the transverse deflection, E the Young's modulus, I the areal moment of inertia, and M the bending momentum. The lever transmission is modeled with two beams, referred to as beam #I and beam #II, connected by a torsional rigid, stiff-jointed framework (Fig. 3.19). The point symmetry (P_{symm}) is used to simplify the model by splitting the transmission into two parts. The point of symmetry is modeled with a hinge condition, since there is only a rotation and momentum in this

⁸Leonhard Euler, Swiss mathematician and physicist, 1707-1783

⁹Daniel Bernoulli, Swiss mathematician and physicist, 1700-1782

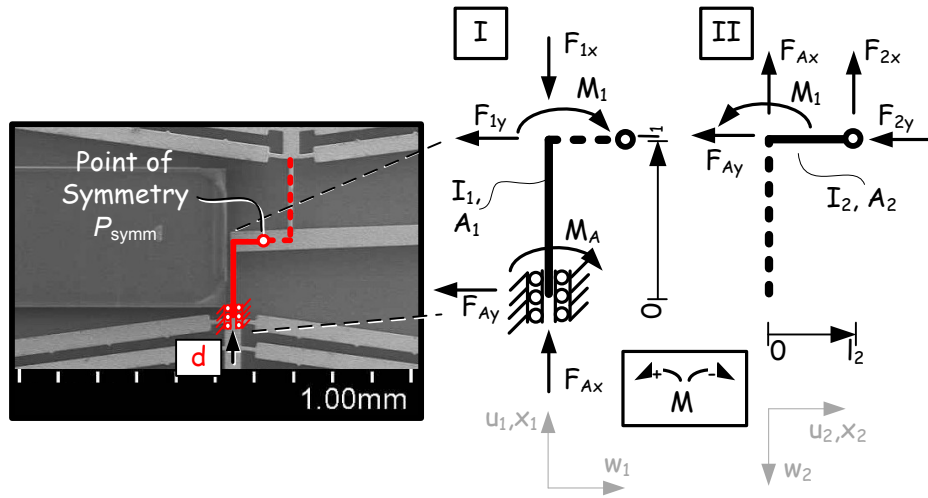


Figure 3.19: Schematics of the model for calculating the spring stiffness of the lever transmission. To simplify the model the point of symmetry is modeled as a hinge. Furthermore, the geometry is split into the vertical beam #I and horizontal beam #II, both connected by a torsional rigid, stiff-jointed framework.

point is zero. The vertical beam (#I) is fixed with a rigid condition and a defined deflection d is applied. The static equilibrium condition is stated by

$$\begin{aligned} F_{Ax} - F_{1x} &= 0 \quad , \\ F_{Ay} + F_{1y} &= 0 \quad , \\ -M_A - M_1 - F_{Ay} \cdot l_1 &= 0 \quad , \\ -F_{Ay} - F_{2y} &= 0 \quad , \\ F_{Ax} + F_{2x} &= 0 \quad , \\ M_1 - F_{Ax} \cdot l_2 &= 0 \quad , \end{aligned} \tag{3.34}$$

with the momentum M_1 to be

$$M_1(x_1) = F_{Ay} \cdot x_1 - F_{Ay} \cdot l_1 - F_{Ax} \cdot l_2 \quad . \quad (3.35)$$

Substitution of Eq. 3.35 into Eq. 3.33 leads to

$$\begin{aligned} w_1(x_1) &= \frac{1}{EI_1} \left(-\frac{F_{Ay}}{6} x_1^3 + \frac{F_{Ay} \cdot l_1 + F_{Ax} \cdot l_2}{2} x_1^2 \right) + \bar{A}_1 \cdot x_1 + \bar{A}_2 \quad , \\ w_2(x_2) &= \frac{1}{EI_2} \left(-\frac{F_{Ax}}{6} x_2^3 + \frac{F_{Ax} \cdot l_2}{2} x_2^2 \right) + \bar{B}_1 \cdot x_2 + \bar{B}_2 \quad . \end{aligned} \quad (3.36)$$

The corresponding in-plane deflections u in accordance to Hooke's¹⁰ law are calculated to be

$$\begin{aligned} u_1(x_1) &= -x_1 \cdot \frac{F_{Ax}}{EA_1} + d \quad , \\ u_2(x_2) &= x_2 \cdot \frac{F_{Ay}}{EA_2} + B \quad , \end{aligned} \quad (3.37)$$

where \bar{A}_1 , \bar{A}_2 , \bar{B}_1 , \bar{B}_2 , and B are integration constants. With the boundary conditions

$$w_1(0) = 0, \quad w_1'(0) = 0, \quad w_2(l_2) = 0 \quad u_2(l_2) = 0 \quad , \quad (3.38)$$

and the connection conditions

$$w_1(l_1) = u_2(0), \quad w_1'(l_1) = w_2'(0), \quad w_2(0) = -u_1(l_1) \quad , \quad (3.39)$$

the equation system Eq. 3.34, Eq. 3.36, and Eq. 3.37 can be solved, yielding to the spring stiffness of the lever transmission

$$k_L = \frac{2E \left[\frac{1}{3} \frac{l_1}{l_2} + \frac{I_1}{A_2} \frac{1}{l_1^2} \right]}{\left[\frac{2}{9} \frac{1}{I_2} l_2^2 l_1 + \frac{1}{6} \frac{1}{I_1} l_1^2 l_2 + \frac{2}{3} \frac{1}{A_1} \frac{l_1^2}{l_2} + \frac{2}{A_2} \frac{l_2^2}{l_1} + \frac{2}{3} \frac{1}{A_2} \frac{I_1}{I_2} \frac{l_2^3}{l_1^2} + \frac{2}{l_1} \frac{1}{A_2} \frac{I_1}{A_1} \right]} \quad . \quad (3.40)$$

The deflection of the tip of the lever x_h , in dependency of the deflection d , can be calculated with the slope

$$w_2'(l_2, d) = \left[\left(\frac{1}{EI_2} \frac{l_2^2}{6} - \frac{l_1}{l_2} \frac{1}{EA_1} \right) k_L + \frac{1}{l_2} \right] \cdot d \quad , \quad (3.41)$$

and the length of the lever h_L to be

$$x_h(d) = w_2'(l_2, d) \cdot h_L \quad . \quad (3.42)$$

3.5.2 Spring Stiffness of V-shaped Beam

Mirror symmetries (mirror symmetry B and C) can be exploited to simplify the model for calculating the spring stiffness of a single beam of half of the V-shaped stack. The beam is split into two halves (mirror symmetry C) and the model only considers one half, where one end is clamped and the other end is modeled by a sliding condition (Fig. 3.20).

¹⁰Robert Hooke, English natural philosopher, architect and polymath, 1635 - 1703

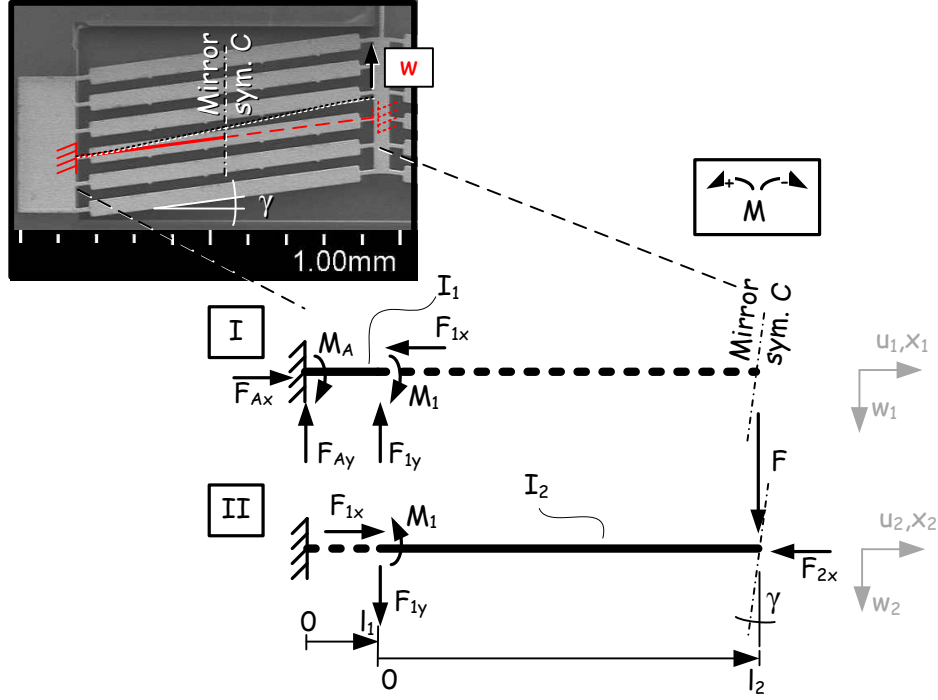


Figure 3.20: Model for calculating the spring stiffness of the V-shaped beam stack. Due to a mirror symmetry C , only half of the beam length is modeled. One side is fixed and the open end is modeled with a sliding condition, considering the inclination angle γ of the beam.

Beam # I and beam # II define the small hinge beam with a area momentum of inertia I_1 and the rest of the beam with I_2 . The static equilibrium condition is written as

$$\begin{aligned}
 F_{Ax} - F_{1x} &= 0 \quad , \\
 F_{Ay} + F_{1y} &= 0 \quad , \\
 -M_A - M_1 - F_{Ay} \cdot l_1 &= 0 \quad , \\
 -F - F_{1y} &= 0 \quad , \\
 -F_{2x} + F_{1x} &= 0 \quad , \\
 M_1 + F_{1y} \cdot l_2 &= 0 \quad ,
 \end{aligned} \tag{3.43}$$

with the momentum M_1 and M_2 to be

$$M_1(x_1) = F_{Ay} \cdot x_1 + M_A, \quad M_2(x_2) = -F_{1y} \cdot x_2 - M_1 \quad . \tag{3.44}$$

Substitution of Eq. 3.44 into Eq. 3.33 leads to

$$\begin{aligned} w_1(x_1) &= \frac{1}{EI_1} \left(-\frac{F_{Ay}}{6} x_1^3 - \frac{M_A}{2} x_1^2 \right) + \tilde{A}_1 \cdot x_1 + \tilde{A}_2 \quad , \\ w_2(x_2) &= \frac{1}{EI_2} \left(\frac{F_{1y}}{6} x_2^3 + \frac{M_1}{2} x_2^2 \right) + \tilde{B}_1 \cdot x_2 + \tilde{B}_2 \quad , \end{aligned} \quad (3.45)$$

and the corresponding in-plane deflections in accordance to Hooke's law

$$\begin{aligned} u_1(x_1) &= -\frac{F_{1x}}{EA} \cdot x_1 \quad , \\ u_2(x_2) &= -\frac{F_{2x}}{EA} \cdot x_2 - \frac{F_{1x}}{EA} \cdot l_1 + \tilde{B} \quad , \end{aligned} \quad (3.46)$$

where \tilde{A}_1 , \tilde{A}_2 , \tilde{B}_1 , \tilde{B}_2 , and \tilde{B} are integration constants. With the boundary conditions

$$w_1(0) = 0 \quad w_1'(0) = 0 \quad u_1(0) = 0 \quad , \quad (3.47)$$

and the connection conditions

$$\begin{aligned} w_1(l_1) &= w_2(0) & w_1'(l_1) &= w_2'(0) \\ u_1(l_1) &= u_2(0) & u_2(l_2) &= \tan(\gamma)w_2(l_2) \quad , \end{aligned} \quad (3.48)$$

the equation system Eq. 3.43 can be solved, leading to a spring stiffness for the vertical deflection of the V-shaped beam of

$$k_V = \frac{E}{\frac{1}{l_1} l_1 l_2 (l_2 + l_1) + \frac{1}{3} \left(\frac{l_2^3}{I_2} + \frac{l_1^3}{I_1} \right)} \quad . \quad (3.49)$$

The connection condition $u_2(l_2) = \tan(\gamma)w_2(l_2)$ takes into account the inclination of the beams, whereas the boundary condition $w_1'(0) = 0$ neglects it in order to simplify the equation system.

3.5.3 Energy Equilibrium

Thermal Energy

When the V-shaped beam is heated up and the beam is restricted to deflect by \bar{w} , the thermally induced elastic energy stored in a single beam element is given by

$$U_{\text{thermal}} = \int_0^{\bar{w}} \ln \left(\frac{l_0 + u}{l_T} \right) E A d w \quad , \quad (3.50)$$

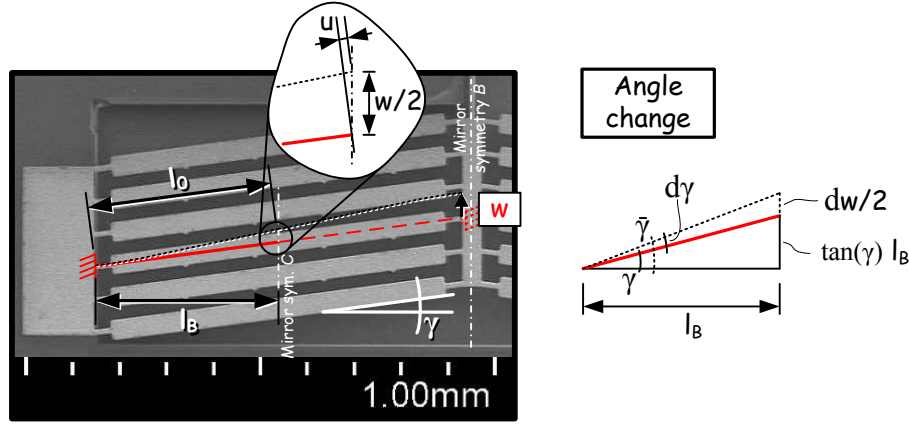


Figure 3.21: The thermal energy is modeled, exploiting the symmetry C of the beam. Only half of the beam length is considered and, therefore, the total deflection w is halved. The angle γ changes due to the deflection w .

where $u = \sin(\gamma)w/2$ the elongation of the beam depending on the total deflection w . This considers that only half of the beam (l_0) was taken into account. The total deflection w is halved when only half of the beam is taken into consideration (Fig. 3.21, mirror symmetry C). With the elongated length $l_T = \exp(\alpha\Delta T) \cdot l_0$, the total thermally induced energy is calculated as

$$U_{\text{thermal}}(w) = 2 \cdot n \cdot \int_0^{\bar{w}} \ln \left(\frac{l_0 + \sin(\gamma) \frac{w}{2}}{\exp(\alpha\Delta T) \cdot l_0} \right) E A d w \quad , \quad (3.51)$$

where n is the number of parallel beams and A the cross section area of the V-shaped beam. The factor 2 results from the mirror symmetric second part of the V-shaped beam stack (Fig. 3.21, mirror symmetry B). The hinge is neglected for this energy consideration. In absence of other forces and energies, the beam elongates until it reaches a length of l_T , so that the thermally induced elastic energy is minimal. Since the beam acts against the elastic deformation energies, the maximum elongation l_T is decreased. Hence, the elastic energies of the V-shaped beam stack and the lever transmission have also to be calculated.

Elastic Energy

The elastic energy U_E of a linear mechanical spring is calculated in general for the deflection w and the spring stiffness k as

$$U_E = \frac{k w^2}{2} . \quad (3.52)$$

Due to the symmetry, the elastic energy of the total V-shaped beam system for a defined deflection w is accordingly given by

$$U_V(w) = 2 \cdot 2 \cdot n \cdot \frac{k_V \left(\frac{w}{2}\right)^2}{2} , \quad (3.53)$$

where n is the number of beams. Since the derived spring stiffness k_V is only calculated for half of the beam length (mirror symmetry *C*), the deflection w is also halved and a factor of 2 considers the second beam half. The second factor of 2 originates from the second part of the V-shaped beam stack (mirror symmetry *B*). The elastic energy of the lever transmission is calculated to be

$$U_L(w) = \frac{k_L w^2}{2} . \quad (3.54)$$

Composed Model

Now, the single energy contributions have to be combined. In accordance to sec 2.3, the system will minimize its total energy U_{tot} until it reaches a minimum energy, stated by

$$\frac{dU_{\text{tot}}(w)}{dw} = 0 \quad (3.55)$$

The total energy consists of the thermal energy (Eq. 3.51) and the elastic energies of the deformed shape of the structure $U_V(w) + U_L(w)$ (Eq. 3.53, Eq. 3.54).

$$U_{\text{tot}}(w) = U_{\text{thermal}}(w) + U_V(w) + U_L(w) \quad (3.56)$$

Substitution of Eq. 3.56 into Eq. 3.55 leads to

$$2 \cdot n \cdot \ln \left(\frac{l_0 + \sin(\gamma) \frac{w}{2}}{\exp(\alpha \Delta T) \cdot l_0} \right) EA + 2 \cdot n \cdot k_V \left(\frac{w}{2} \right) + k_L w = 0 . \quad (3.57)$$

Rearrangement and Taylor approximation of $\sin(\gamma) \frac{w}{2} \ll 1$ up to $\mathcal{O} \left(\left(\sin(\gamma) \frac{w}{2} \right)^2 \right)$ results in the deflection w of the V-shaped beam stack to be

$$w = \frac{2 \cdot l_0 \cdot \alpha \Delta T}{\sin(\gamma) + \frac{l_0}{E \cdot A} k_{\text{comp}}} , \quad (3.58)$$

with

$$k_{\text{comp}} = k_V + \frac{k_L}{n} \quad (3.59)$$

the composed spring stiffness of the V-shaped beam and the lever transmission. The approximation is valid for small elongations u . Up to now, it was assumed that the angle γ will not change for any deflection of w .

Iteration: Considering that the angle γ is a function of the deflection w , the differential form of Eq. 3.58 reads

$$dw = \frac{2 \cdot l_0 \cdot \alpha dT}{\sin(\gamma + d\gamma) + \frac{l_0}{E \cdot A} k_{\text{comp}}} \quad , \quad (3.60)$$

with the differential angle

$$d\gamma = \arctan\left(\frac{l_B \cdot \tan(\gamma) + \frac{dw}{2}}{l_B}\right) - \gamma \quad , \quad (3.61)$$

and l_B as the projected length of l_0 to the horizontal ($l_B = \cos(\gamma)l_0$, Fig. 3.21). Substituting Eq. 3.61 into Eq. 3.60, a Taylor approximation for $dw \ll 1$ up to order $\mathcal{O}(dw^2)$ and rearrangement leads to the equation

$$\begin{aligned} 0 = & dw dw \\ & + \overbrace{\frac{2}{\cos(\gamma)^3} \left(\sin(\gamma) + \frac{l_0}{E \cdot A} k_{\text{comp}} \right)}^p l_B \cdot dw \\ & \underbrace{\frac{4}{\cos(\gamma)^3} l_0 \cdot l_B \cdot \alpha dT}_q \quad . \end{aligned} \quad (3.62)$$

Solving this quadratic equation, in accordance to

$$dw_{1,2} = -\frac{p}{2} \pm \sqrt{\frac{p^2}{4} - q} \quad , \quad (3.63)$$

and Taylor approximation for $\alpha dT \ll 1$ up to second order gives the solutions for dw to be

$$\begin{aligned} dw_1 = & \frac{2 \cdot l_0 \cdot \alpha dT}{\sin(\gamma) + \frac{l_0}{E \cdot A} k_{\text{comp}}} \\ & - \frac{2 \cdot l_0 \cos(\gamma)^2 (\alpha dT)^2}{\left(\sin(\gamma) + \frac{l_0}{E \cdot A} k_{\text{comp}} \right)^3} \quad , \end{aligned} \quad (3.64)$$

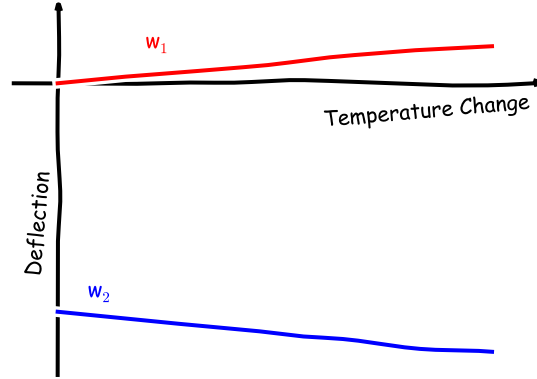


Figure 3.22: Deflection w_1 and w_2 in dependence of a temperature change ΔT .

and

$$\begin{aligned}
 dw_2 = & -\frac{l_0}{\cos(\gamma)^2} \left(\frac{l_0}{E \cdot A} k_{\text{comp}} + \sin(\gamma) \right) \\
 & - \frac{2 \cdot l_0 \cdot \alpha dT}{\frac{l_0}{E \cdot A} k_{\text{comp}} + \sin(\gamma)} \\
 & + \frac{2l_0 \cos(\gamma)^2 (\alpha dT)^2}{\left(\frac{l_0}{E \cdot A} k_{\text{comp}} + \sin(\gamma) \right)^3} \quad . \quad (3.65)
 \end{aligned}$$

The second solution w_2 is skipped since it describes the case when the angle of the V-shaped beam changes sign (Fig. 3.22). Therefore, only the solution w_1 is taken into account. Eq. 3.64 can be integrated

$$\begin{aligned}
 \int dw_1 = & \int \frac{2 \cdot l_0 \cdot \alpha dT}{\sin(\gamma) + \frac{l_0}{E \cdot A} k_{\text{comp}}} \\
 & - \int \frac{2 \cdot l_0 \cos(\gamma)^2 (\alpha dT)^2}{\left(\sin(\gamma) + \frac{l_0}{E \cdot A} k_{\text{comp}} \right)^3} \quad , \quad (3.66)
 \end{aligned}$$

finally yielding the temperature dependent deflection of the V-shaped beam stack to be

$$\begin{aligned}
 w_1(\Delta T) = & \frac{2 \cdot l_0 \cdot \alpha \Delta T}{\sin(\gamma) + \frac{l_0}{E \cdot A} k_{\text{comp}}} \\
 & - \frac{l_0 \cos(\gamma)^2 (\alpha \Delta T)^2}{\left(\sin(\gamma) + \frac{l_0}{E \cdot A} k_{\text{comp}} \right)^3} \quad . \quad (3.67)
 \end{aligned}$$

This deflection can now be set equal to d in Eq. 3.41 and the deflection at the tip of the lever can be calculated with Eq. 3.42 (compare Fig. 3.18).

Force

The blocking force of the actuator when the movement of the tip of the geometry is restricted, is approximated by the axial force of the V-shaped beam. The V-shaped beam is heated up and a force is applied that compresses the beam to its original length. This force is directly proportional to the force pushing against the lever transmission when the tip of the structure is fixed and the bending of the lever beam is neglected.

When the geometry of Fig. 3.20 is compressed by Δl , the force equilibrium is given by $F_1 = F_2$, where

$$F_1 = EA_1 \frac{-x}{l_1(T)} \quad , \quad (3.68)$$

and

$$F_2 = EA_2 \frac{x - \Delta l}{l_2(T)} \quad . \quad (3.69)$$

The equilibrium results in a deflection x to be

$$x = \frac{l_1(T) A_2 \Delta l}{l_1(T) A_2 + l_2(T) A_1} \quad . \quad (3.70)$$

When $l_i(T)$ is the elongated length of the beam at elevated temperatures

$$l_i(T) = l_{0,i} \cdot (1 + \alpha \Delta T) \quad , \quad (3.71)$$

and the geometry is compressed to its initial length, where Δl is stated by

$$\Delta l = (l_{0,1} + l_{0,2}) \cdot \alpha \Delta T \quad , \quad (3.72)$$

the resulting compressive force is calculated as


$$F_1 = -E \frac{(l_{0,1} + l_{0,2}) \alpha \Delta T}{\left(\frac{l_{0,2}}{A_2} + \frac{l_{0,1}}{A_1} \right) (1 + \alpha \Delta T)} \quad . \quad (3.73)$$

This is the in-plane force for the V-shaped beam. Multiplied with $\sin(\gamma)$, this force yields in the resulting force F_V (Eq. 3.74) that pushes against the lever transmission.

$$F_V = E \frac{(l_1 + l_2) \alpha \Delta T}{\left(\frac{l_2}{A_2} + \frac{l_1}{A_1} \right) (1 + \alpha \Delta T)} \cdot \sin(\gamma) \quad , \quad (3.74)$$

The force at the tip is defined by the lever transmission to be

$$F_{\text{tip}} = 2 \cdot n \cdot \frac{F_V}{h_L} \frac{d_{\text{off}}}{2} \quad , \quad (3.75)$$

where $d_{\text{off}}/2$ is the length l_2 from the lever transmission (Fig. 3.19) and the factor of 2 arises from mirroring the V-shaped beam stack (mirror symmetry A). 

"I have not failed. I've just found 10,000 ways that won't work."

Thomas A. Edison

"Inside every small problem is a large problem struggling to get out."

Second Law of Blissful Ignorance

4 Manufacture or Dos and Dont's



MINIATURIZING structures has become very important in the last decades. By reducing the size of a system it becomes more sensible, consumes less power, and can be easily integrated. This integration came to a level, that nowadays smart-phones have more computational power than the Apollo moon mission in 1969 [87]. A huge amount of different micro fabrication technologies were investigated and established, resulting in structure sizes for state of the art ICs (integrate circuits) of 18 nm. Also a large field of processes have become available for the manufacturing of MEMS devices.

This chapter summarizes the approaches for manufacturing the temperature threshold sensor from a historical point of view. Subsequently, the results, drawbacks, and problems for different approaches are listed and discussed.

4.1 Technologies based on SU-8

SU-8 is an epoxy based photo polymer. It was chosen as active material for the actuator due to its excellent coefficient of thermal expansion of $\alpha_{\text{SU-8}} = 50 \text{ ppm/K}$ [88]. It is well established and known for manufacturing MEMS devices, at which it is used as bonding material between Si or glass chips, for micro structures, or for micro-fluidic channels [89–96].

SU-8 comprises three components: Epoxy resin, solvent, and photo acid generator (PAG). The epoxy resin polymerizes and builds up the desired structure. It consists of four polymerized Bisphenol-A molecules with eight epoxy rings. The molecules are dissolved in γ -Butyrolactone. After spin coating the layer, this solvent is evaporated by a drying step at elevated temperatures. The PAG acts as catalyst for the photochemical reaction during exposure. Triarylium-sulfonium salt is used as PAG, which releases H^+ -ions. These H^+ -ions break the epoxy rings, which then can polymerize with other broken epoxy rings. This cross linking releases additional H^+ -ions, that can again break chemical bonds, leading to a chain reaction. But the polymerization takes place at very slow rates at room temperature, due to the slow diffusion of the relatively large molecules. Therefore, a post exposure bake (PEB) is necessary to increase the mobility and diffusion of the molecules. The cross linking only occurs in regions that are exposed to light and the H^+ -ions are released from the PAG. At high temperatures ($>200^\circ\text{C}$), also the thermal energy is sufficient for breaking the epoxy rings and to start the cross linking reaction. Hence, high temperatures can be used for more interconnections and cross linking within the layer. A hard bake (HB) is carried out after the development of the layer. The unexposed and not cross linked material can be developed with KOH (potassium hydroxide) or PGMEA (propylene glycol methyl ether acetate) prior to the final hard bake.

4.1.1 SU-8 with SU-8 Technology

In the first approach, SU-8 is used as active material for the micro structures and as sacrificial layer to release and separate the structures from the substrate.

In a first step, a 100 nm thick titanium layer is evaporated and patterned by a lift-off process on a silicon (100) wafer. In well defined regions, the Ti acts as adhesive layer for the later deposited SU-8 structure. At first, the SU-8 layer is spun at a maximum rotation of 4200 rpm for 40 sec and dried for 40 min at 95°C on a hot plate (Sawatec). This layer acts as sacrificial layer and only the anchor regions are exposed to UV-light (EVG620 Maskaligner, 365 nm wavelength) for 30 sec. This exposure leads to a photochemical reaction and the SU-8 starts to polymerize and, therefore, the exposed regions become insoluble to the developer. A 16 h post exposure bake at 60°C evaporates the residual solvent in the layer and supports the polymerization process. After the PEB, the SU-8 layer is 20 μm in height. A 2 μm thick Cu layer is evaporated on top of the

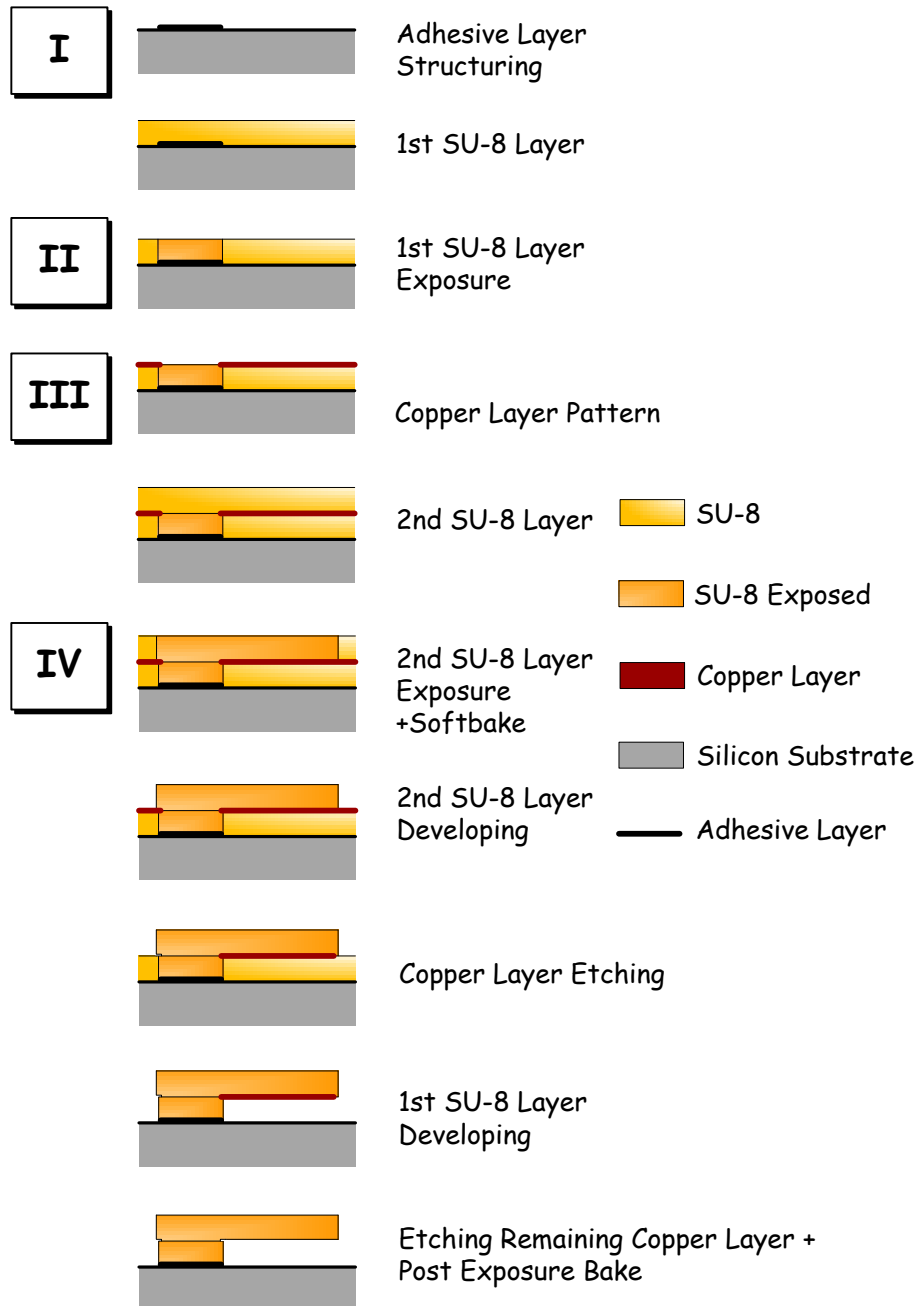


Figure 4.1: Process flow of the SU-8 on SU-8 technology. An adhesive layer and a sacrificial SU-8 layer define the anchor region where the micro structure is fixed to the substrate. The structure is formed by an additional SU-8 layer. A Cu layer separates both layers. After structuring and developing of the 2nd layer, the Cu is etched and the 1st layer can be developed. Again, the residual Cu is removed to release the structures.

SU-8. This Cu layer protects the underlying SU-8 from UV-light during the exposure and structuring of the second SU-8 layer. The Cu layer is patterned by a lift-off process to establish a direct contact between both SU-8 layers in the anchor regions. The second SU-8 layer forms the final micro structures. It is spun at a maximum speed of 4200 rpm for 40 sec and dried at 60°C for 20 h on a hotplate (Sawatec). The low temperature is chosen to prevent further polymerization of the underlying sacrificial SU-8 layer. The structures are defined by a lithographic step, where the layer is exposed through a mask with UV-light for 45 sec (MA150, 365 nm wavelength). The post exposure bake supports the polymerization and is carried out at 60°C for 16 h (hotplate, Sawatec). The layer is developed with PGMEA for 4 min, where the unexposed regions dissolve in the developer. The copper layer is etched with 20% Na₂S₂O₈ (sodium persulfate) for 10 min. Afterwards, the sacrificial SU-8 layer is developed with PGMEA. The residual copper between the two SU-8 layers is again etched with sodium persulfate (20% in water). The detailed process flow can be found in Fig 4.1, where roman numbers indicate the lithographic step for patterning the adhesive, the SU-8, and the Cu layer.

Results

It was found that the sacrificial SU-8 layer is too soft in compare to the Cu layer. After depositing the Cu layer, the intrinsic compressive stress leads to a buckling of the layer. This buckling imposes an unpredictable stress within the micro structures and also hampers the lithographic processes. Figure 4.2a depicts a micrograph of the buckled surface after the Cu layer was applied; Fig. 4.2b shows the wafer after finishing the process. There are still some areas, where the Cu layer is insufficiently removed. This is due to upcoming bubbles and voids for small feature size during the etch step. There are also some adhesion problems between the Si substrate and the SU-8 structures. The optical micrograph (Fig. 4.2c) reveals that some structures are deformed and peeled off of the adhesive layer.

Due to the buckling of the Cu layer, a different approach was searched for.

4.1.2 Cu with SU-8 Technology

A stiffer material had to be used as sacrificial layer to get rid off unwanted buckling. Therefore, Cu was chosen as sacrificial layer.

A 100 nm thick Ti adhesive layer is evaporated and patterned with lift-

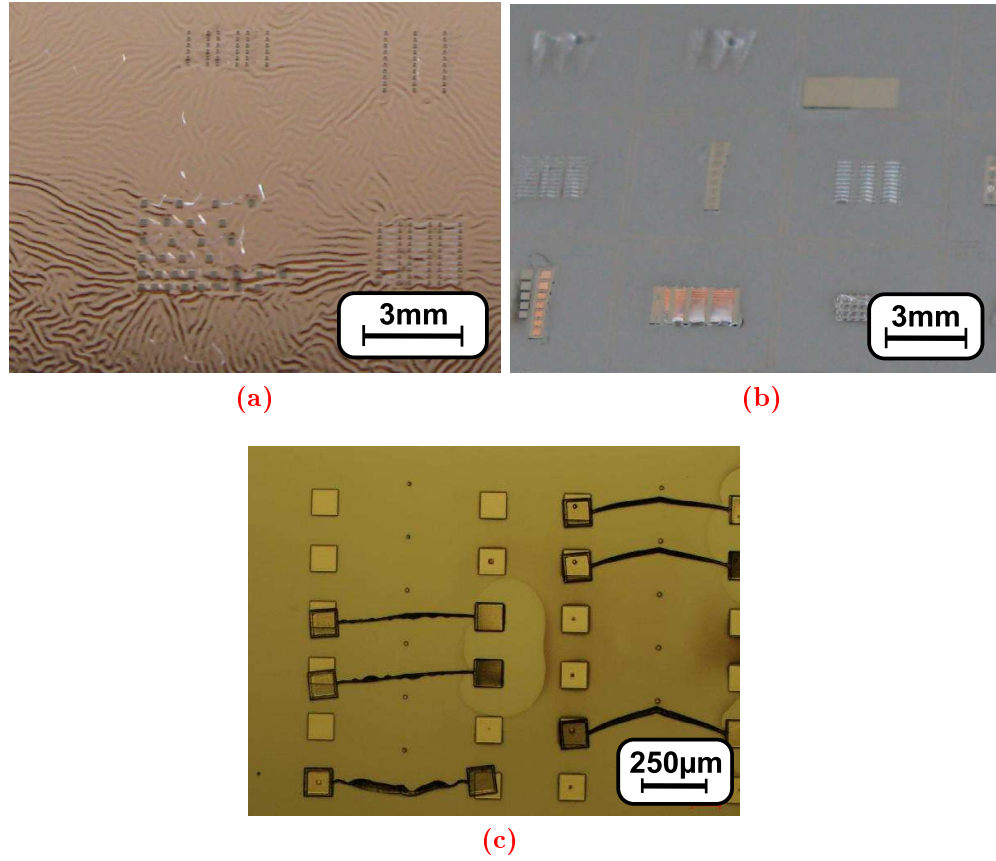


Figure 4.2: Optical micrograph of the wafer. (a) After the copper layer is applied, the layer buckles due to a low stiffness of the underlying SU-8 layer and the intrinsic compressive stress. The observable rectangular areas are the anchor regions of the structures. (b) After finishing of the fabrication there are still areas left where the copper was insufficiently removed. (c) The interface between the adhesive layer and the SU-8 breaks and the structures get misshaped due to an unpredictable stress distribution within the buckled copper layer.

off onto the Si (100) substrate wafer. This pattern defines the anchor regions of the structures. The sacrificial Cu layer is also evaporated and patterned by a lift-off process. As adhesive promoter for the Cu, a 50 nm thick Ti layer is evaporated and, immediately afterwards, the 2 μm thick Cu layer. In the anchor regions, the first adhesive 100 nm thick Ti layer is kept free as bonding interface between the Si substrate and the SU-8 micro structures. The SU-8 layer is spun at a maximum speed of 3600 rpm for 40 sec and dried on a hot plate (Sawatec) at 95°C for 25 min. The resulting structure is 30 μm in height. The lithography is carried out in two steps. At first, only the anchor regions are exposed to UV-light. In a second step, the layer is exposed through a mask that carries the whole structures. Both are done with the mask aligner MA150 and exposed to the UV-light (365 nm) for 30 sec. In this way, the adhesion to the substrate is increased, because the anchor regions are double exposed and, therefore, a stronger and faster polymerization in this regions is induced. The aspect ration is also increased, because areas with small feature sizes are not overexposed, minimizing the polymerization due to stray light and diffusion. The whole layer is post exposure baked at 60°C for 16 h (hot plate, Sawatec) and developed with PGMEA for 3 min. Afterwardes, the structures are flood exposed without any mask for 1 min to harden the layer and to increase the cross linking within the layer. The hard bake is carried out on a Sawatec hot plate for 60 min at 200°C. The Cu layer is etched with 20% $\text{Na}_2\text{S}_2\text{O}_8$ to release the structures, rinsed with isopropanol, and dried on a spinner at 1500 rpm. Figure 4.3 summarizes the process, where roman numbers corresponds to the mask for patterning the adhesive Ti, SU-8, and Cu layer.

Results

There are still some adhesive problems at the corners of the anchor regions. But the structure manufacturing was in general successful. First structures are realized as V-shaped beams with different length and inclined angles. The tip deflection, due to shrinkage of the material is measured with an optical microscope. The SU-8 is dissolved in γ -Butyrolactone and during the drying step, this solvent vanishes. Furthermore, the cross linking within the layer leads to a change in volume. This results in a significant shrinkage of the material. The measured deflections are compared to the specified dimensions of the design and the shrinkage of the structures is calculated, giving $\epsilon_{\text{shrink}} = 0.86 \pm 0.28\%$ in total length. Figure 4.4 shows the optical measurement compared to the specified dimensions on the mask.

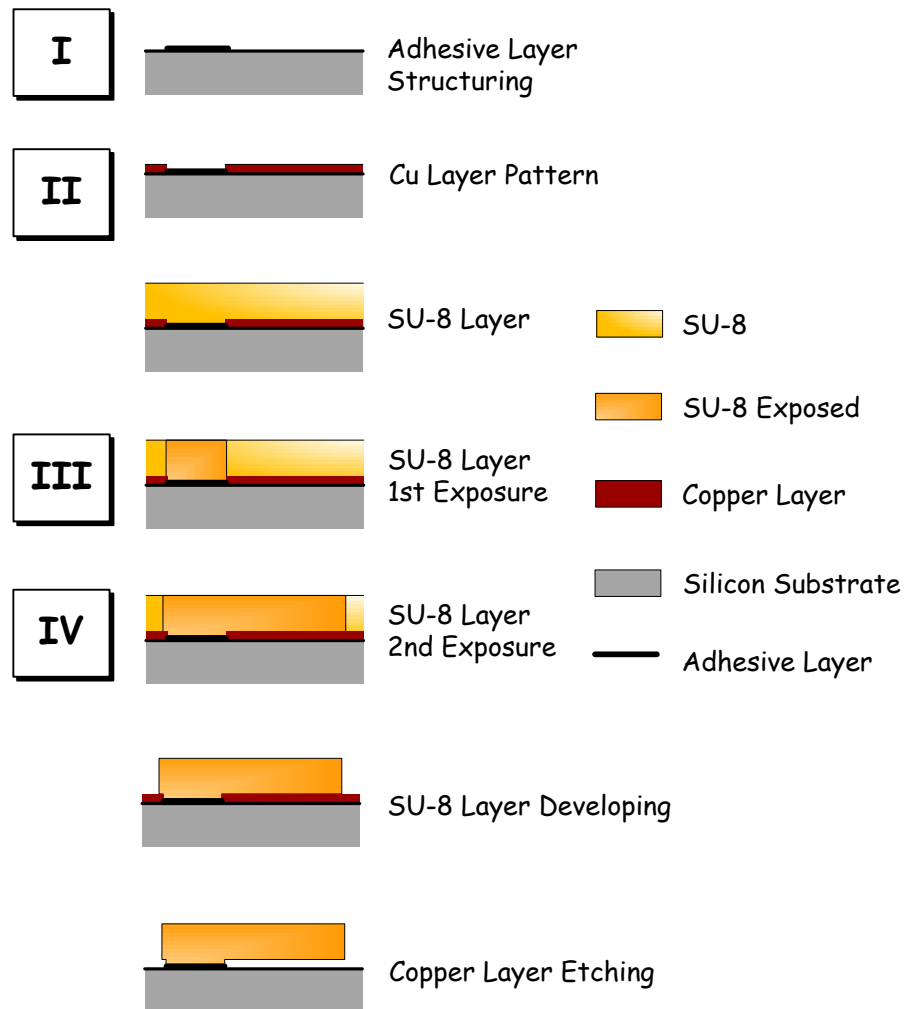


Figure 4.3: Process flow of the structures with SU-8 on a Cu sacrificial layer. After applying and patterning an adhesive and sacrificial Cu layer, the SU-8 is deposited. This layer is structured by lithography and finally, the copper is etch to release the structures.

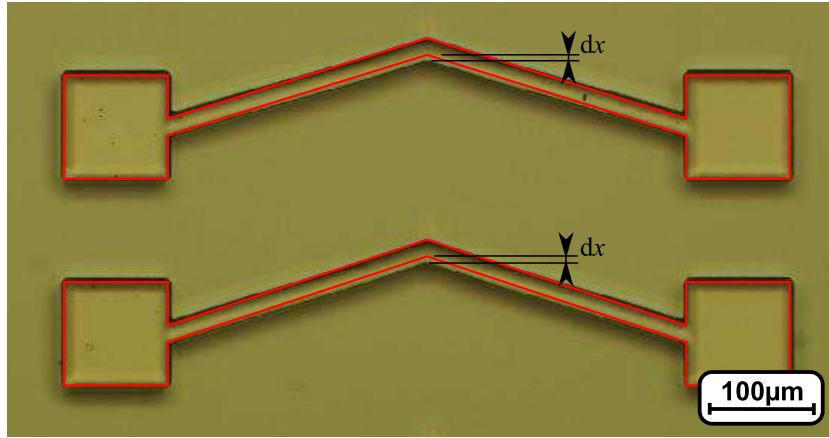


Figure 4.4: Optical micrograph of the deflection and the shrinkage of the material. V-shaped beams with different inclination angle are manufactured and the resulting geometry is compared to the specified dimension on the mask. The deflection of the tip dx is measured and the shrinkage of the material is calculated.

One of the most tantalizing problems during fabrication is stiction. Figure 4.5 depicts interference fringes, indicating that some structures are stuck to the substrate. This problem can be solved either, by increasing the sacrificial layer height, by increasing the structure height, or by completely removing the substrate underneath the structures. Increasing the height of the sacrificial layer means an increased evaporation time of the sacrificial Cu layer. The evaporation rate of Cu is about 10-15 Ångström¹/sec, therefore, increasing the Cu layer height leads to evaporation times of several hours. While for scientific issues this is no problem, apart of the thermal stress for the machine, this will increase the cost of the product for industrial manufacturing. Also the etch time of the Cu has to be increased, which can lead to an unwanted etching of the SU-8 too, or unexpected chemical reactions. Increasing the SU-8 layer height reduces the aspect ratio and, therefore, the minimal feature size of the design. Removing the Si substrate is the easiest way to solve the stiction problem and is realized in the next approach.

4.1.3 SU-8 Technology Backside Released²

Removing the substrate underneath the movable parts of the structures has a few advantages over the previously described approaches. On the

¹Anders Jonas Ångström, Swedish physicist, 1814-1874.

²The section is partly published in [97].

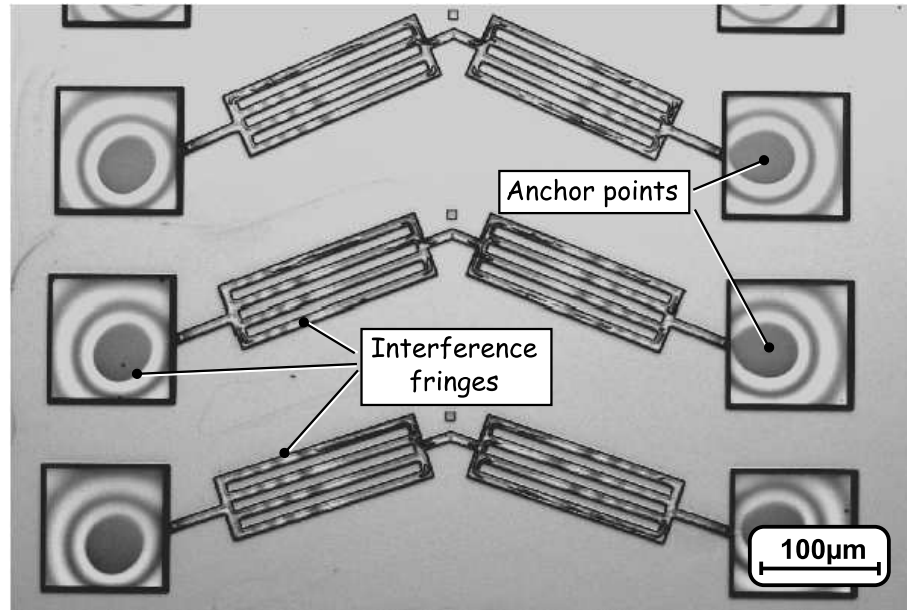


Figure 4.5: Optical micrograph of the SU-8 micro structures. The image is converted to gray scale for a better visibility. The interference fringes in the anchor regions indicate that there is still an insufficient adhesion to the substrate. Interference fringes can be also observed along the length of the bent beams, indicating stiction.

one hand, the stiction probability is reduced to zero and, on the other hand, there is no need for a sacrificial layer anymore. This reduces the number of masks needed.

At first, a 5 nm thick Ti layer is evaporated as adhesive layer for the SU-8 layer. It is spun at a maximum speed of 3600 rpm for 40 sec and dried on a hotplate (Sawatec) at 95°C for 25 min. This procedure results in an SU-8 layer height of 30 µm. The layer is exposed to UV-light at a wavelength of 365 nm for 40 s (MA150) through a mask, holding the structure designs. The post exposure bake is carried out at 90°C for 10 min (hotplate, Sawatec). The layer is developed by rinsing with PGMEA for 3.5 min and afterwards rinsed by isopropanol and DI water to remove the residual developer. Optical inspection of the wafer reveals that there are still adhesion problems at the structure boundaries. But the adhesion is in principle sufficient for the further progress. After the development step, the layer is hard baked at 200°C for 1 h (hotplate, Sawatec). The structures are spray coated with AZ4562 resist and dried at 95°C for 10 min, three times. This layer acts as mechanical support for the structures and as protection from contaminations. The photore-

sist AZ6624 is spun at the backside of the wafer at a maximum speed of 2500 rpm for 40 sec and dried at 107°C for 5 min, two times. This resist is patterned by lithography (UV-light 365 nm, 20 sec, EVG601) and acetone as developer, defining areas beneath the topside micro structures where the Si substrate will be removed. The Si is removed by a plasma etch process (Bosch process with 500 cycles of etching and sidewall passivation, Oxford Instruments). The plasma etch process also etches the 5 nm thick Ti adhesive layer and, therefore, there is no need for an extra wet etch step to remove this otherwise remaining thin membrane. At this point, the structures are only supported by the applied protection layer. After the wafer is cut into single dies, the protection layer is removed by rinsing the individual dies with acetone and isopropanol. The dies are carefully dried by an N₂ flow over the surface. The residual resist is removed with an O₂ plasma (STS, 10 min, 200 W, 150 mTorr). Figure 4.6 summarizes the process steps and roman numbers indicate the lithographic steps for structuring the SU-8 and the Si substrate.

Results

After measuring the shrinkage of the material, a new set of mask is required. Thermal actuators are designed and manufactured with the process described in this subsection, where the initial deflection due to the shrinkage of the material is considered. Optical inspections of the structures exhibit the appearance of cracks in the SU-8 layer at areas with high mechanical deformations, especially at the regions of the coupling bars. But this cracks doesn't seem to affect the functionality of the devices (Fig. 4.7).

The structures are characterized with a custom made temperature stage (see subsec. 5.1.1 for details). A temperature cycle ranging from +30°C down to -30°C, starting at +20°C is applied in steps of 10°C. Each temperature is constant for a specific time. During the initial temperature of +20°C, the measurement chamber is purged with N₂. The whole structure is sensitive to the surrounding humidity and the material shrinks during that purging [98, 99]. This leads already to a deflection of -60 µm within the first 17 min. When heating to +30°C, the material expands, resulting in a total deflection of -53 µm, which is almost constant over the threshold time. The structure is constantly cooled down in the further progress. During each cooling step of 10°C, the material contracts and the total deflection decreases directly compared to the last measured deflection of the previous temperature. But the deflection is not

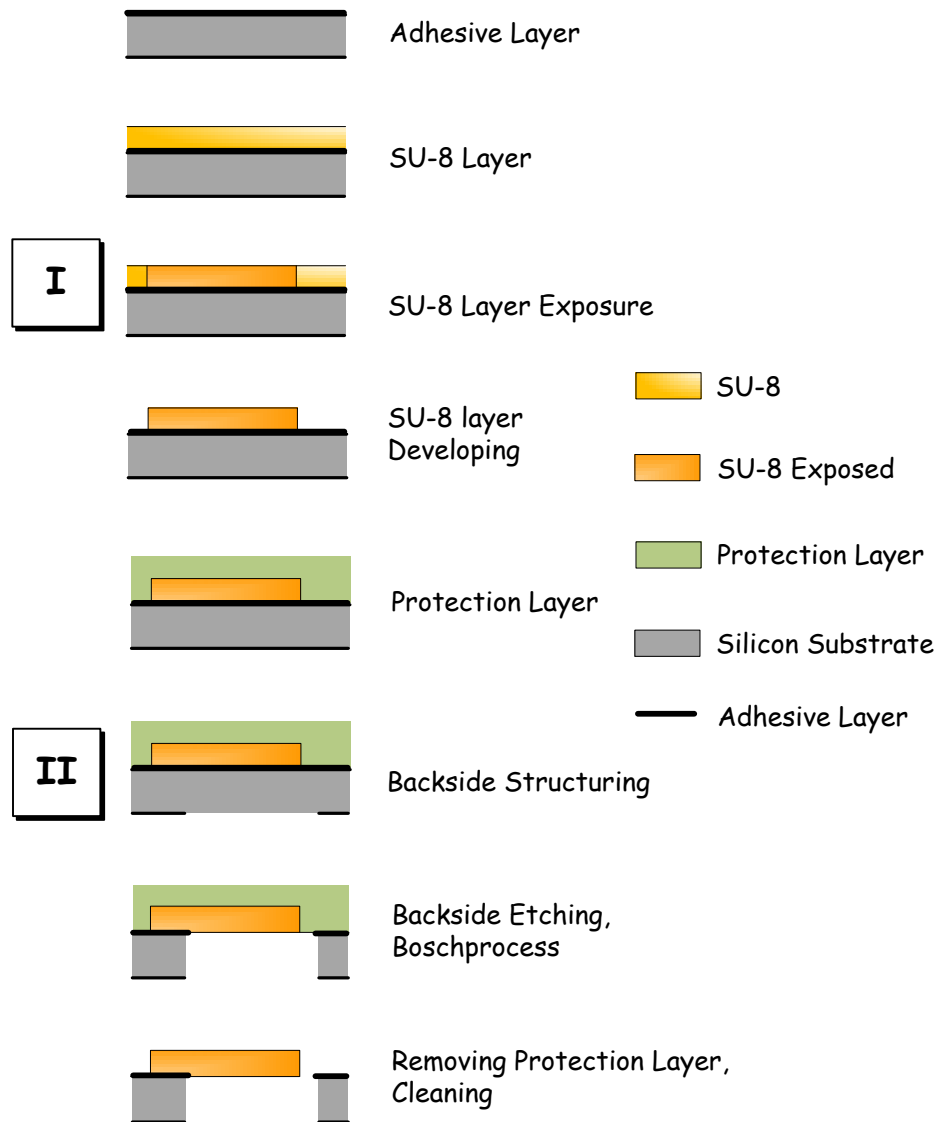


Figure 4.6: Process flow for manufacturing of SU-8 micro structures with a backside release. After applying an adhesive layer, the SU-8 layer is directly patterned on this adhesive layer. A protection layer is applied as mechanical stabilization. The Si substrate beneath the structures is partly etched by a plasma Bosch process from the backside. Afterwards, the protection layer is removed and, finally, the structures are cleaned. Only two lithographic steps are needed, reducing the complexity and costs for the manufacturing of the devices.

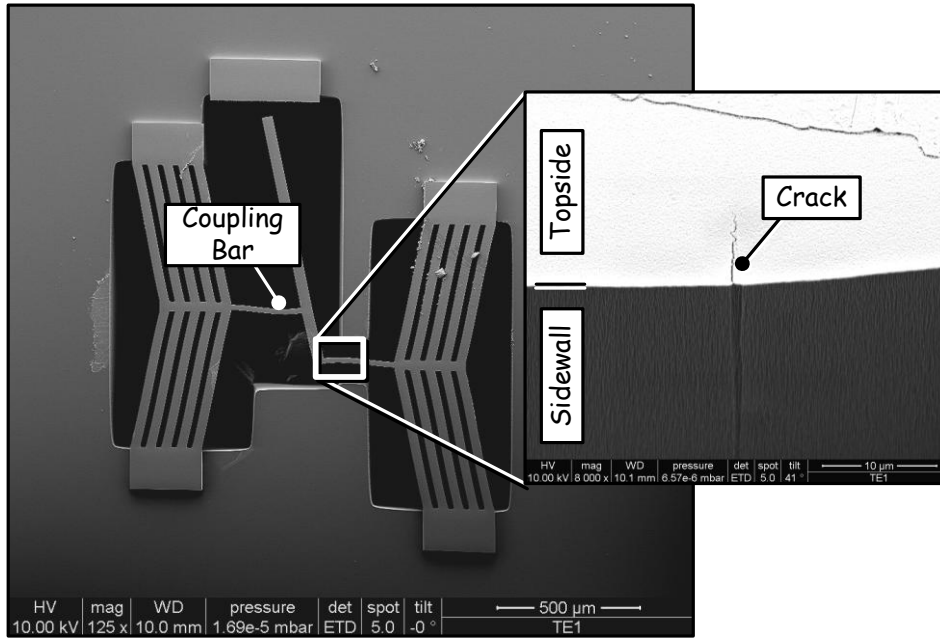
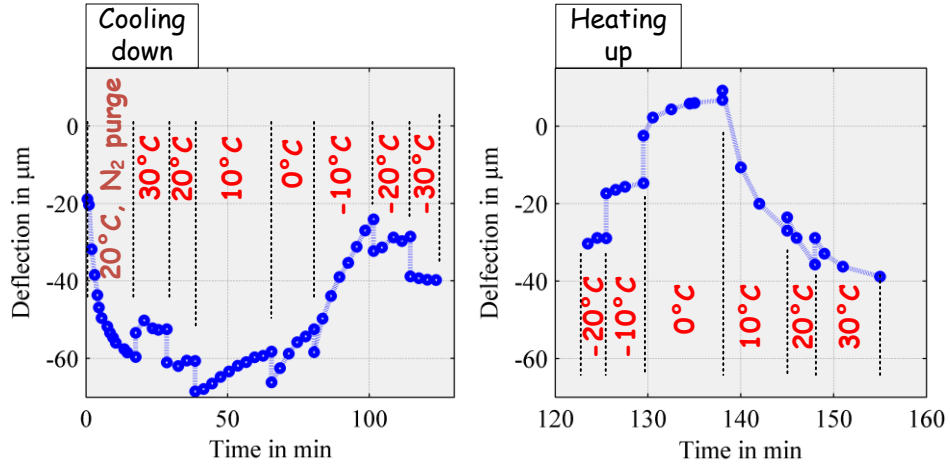


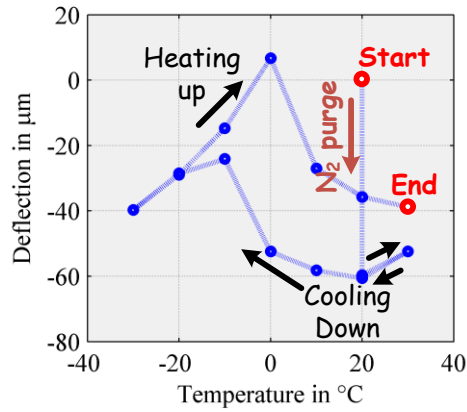
Figure 4.7: Scanning electron microscope micrograph of the SU-8 structures. The inlay shows the coupling bar and the sidewall of the layer, where small cracks can be observed after finishing the manufacturing process. These cracks appear in the regions of largest mechanical stress.

constant over time. A creeping or relaxation happens and the material deflection changes over time [100, 101]. This results in an increasing deflection during the cooling down and decreasing deflection during the heating up of the sample. The change-rate raises for lower temperatures and is largest during the -10°C temperature step. During the cooling down from $+20^{\circ}\text{C}$ to -10°C , a kind of phase change happens and the deflection at the end of the -10°C step is much higher than the initial deflection after purging with N_2 . Instead of a constant shrinkage of the material with decreasing temperature, the material expands in the range from $+20^{\circ}\text{C}$ to -20°C . The creeping rate changes sign at -30°C and becomes almost a flat. By plotting the last measured deflection just before a new temperature is set, the non-linear behavior of the SU-8 can be clearly observed. Instead of an expected linear decrease during cooling down, which corresponds to a linear coefficient of thermal expansion, the material expands. A massive creeping can be observed above 0°C during the heating up (Fig. 4.8a+b).

This non-linear behavior was totally unexpected and massively disturb



(a)



(b)

Figure 4.8: Deflection of the tip of an SU-8 structure evaluated at different temperatures. (a) Each temperature was kept constant for an specific time during cooling down and heating up. The SU-8 exhibits a non-linear thermo-mechanical behavior in the temperature range from +20°C down to -20°C. (b) The plot depicts the deflection right before the temperature was changed.

the functionality of the device. For sure, there could be found some designs that take advantage of this effect. The sensitivity to moisture means that a hermetical sealing is needed to guarantee a proper operation of the sensor. This sealing increases the cost and complexity and such packages are often not longer CMOS compatible. Hence, another technology was searched for the realization of a thermal actuator, resulting in the use of Ni instead of SU-8.

4.2 Technologies based on Ni

In the last century, the progress in the field of micro fabrication was enormous [102]. Aside of physical and chemical vapor deposition also electroplating became feasible for the fabrication of MEMS devices [103, 104]. Ni has already proved to be a “good” material for a thermal actuator (see sec. 3.4). There are plenty of publications, reporting Ni as material for micro structures. Due to the problems with the SU-8, an alternate technology process with Ni was given a chance. At first, a professional provider was chosen to prove the functionality of the design for the thermal actuator. In the next step, a technological process was established in-house and the know-how of a local company (Happy Plating GmbH, Austria [105]) was used for electroplating Ni.

4.2.1 Metal MUMPs Technology³

Europractice is a consortium of companys, offering aplenty of processes to prototype ASICs and MEMS for scientific issues [108]. Among these, there is MEMSCAP offering a Metal MUMPs (Multi User Multi Projects) process, to prototype MEMS devices with electroplated Ni [109–113].

The process has very strict design rules, where the most disappointing one is the minimum feature size of 8 μm . The material has an intrinsic stress of 1000 MPa, which has to be taken into account during the design of the structures. There is also a stress gradient along the height of the Ni layer, leading to an out-of-plane bending towards the substrate. A schematic cross-section view of the relevant layers is given in Fig. 4.9. A silicon substrate is used with an $\text{Si}_3\text{N}_4/\text{SiO}_2$ top cover. The top cover acts as electrical insulation. The top cover is also used to define openings, where trenches with 25 μm depth are formed with a KOH wet etch

³The section is partly published in [106, 107].

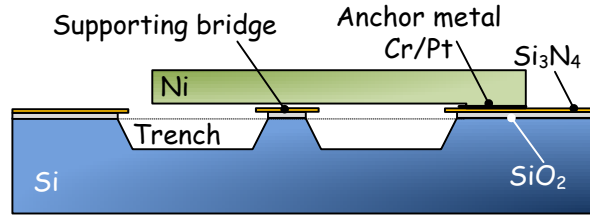


Figure 4.9: Schematic cross-section of the relevant layers to realize Ni MEMS with the electroplating process offered by MEMSCAP.

process at 50°C. The trenches beneath the structures are required to prevent stiction problems. The Ni layer is 20 μm thick. If the thermal actuator should meet a latch or a counterpart, the out-of-plane bending must be reasonable smaller than this layer thickness. Therefore, supporting bridges are formed that keep the structures in-plane. A die size of $10.000 \times 10.000 \mu\text{m}^2$, with an effective design area of $8.000 \times 8.000 \mu\text{m}^2$ can be filled with structures. Special care must be taken that 30-40% of the area is filled with Ni structures to ensure a homogeneously layer growth. The whole area is densely packed with several design variations. Furthermore, rectangular dummy areas are defined in between the designs to meet the requested fill factor. More detailed information about the process and the constraints can be found in the Metal MUMPs Handbook [114]. Figure 4.11 shows an SEM micrograph of the manufactured structures.

The electrical insulation layer is needed to separate the leads of the resistive readout of the sensor's state.

Results

The functionality of the supporting bridges is evaluated with a light interference method (Polytec, MSA400). The topography of structures with and without those bridges are compared (Fig. 4.10). A beam with an approximate length of 1 mm bends 15 μm towards the substrate. The total layer height is 20 μm and, therefore, there is a not negligible risk, that the latch of the thermal actuator will miss its counterpart. The supporting bridge don't interfere with the movement of the structure. There is no interconnection between the bridge and the Ni and the lever can easily slide along the bridge. Figure 4.11 depicts a detailed SEM micrograph of the region of the bridge. The Ni lever is horizontal and also the sidewall of the layer can be seen, because the image is taken at an inclined angle. The surface of the bridge runs perpendicular to the

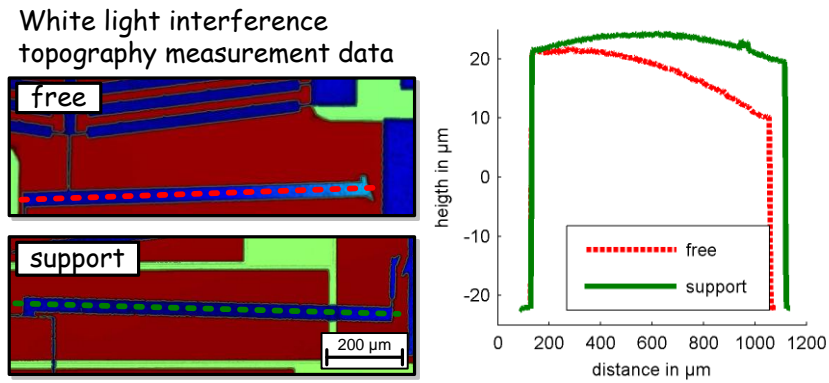


Figure 4.10: Topography measurements of the manufactured structures with and without supporting bridges. The supporting bridges keep the lever in-plane. Otherwise it bends about $15\text{ }\mu\text{m}$ out-of-plane towards the substrate.

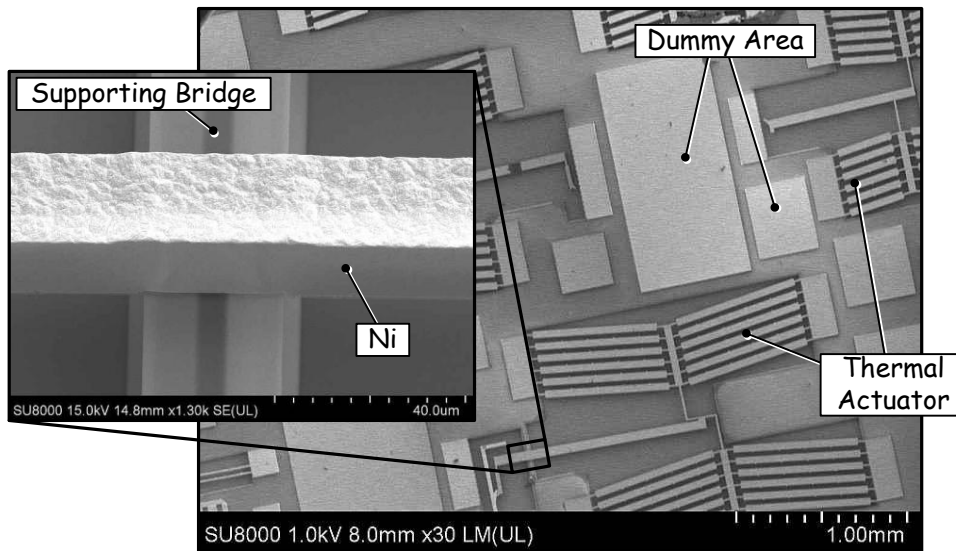


Figure 4.11: SEM micrograph of manufactured structures and detailed view of the region of the supporting bridge.

Ni lever.

Several drawbacks are associated with this technological process. On the one hand, there are only two runs available per year, with the risk of a cancellation when there are too few participants. When a design is sent in at a specific deadline, one has to wait a few months, until the manufactured prototype is delivered. The design has to be characterized and investigated, leaving little time for a redesign and an iteration process.

until the next layout deadline. The design rules limit the possibilities in the design of the structures, so does the stress gradient and the supporting bridges needed. Therefore, alternative manufacturers were searched for.

4.2.2 Electroplated Ni Technology⁴

The Happy Plating GmbH in Wr. Neustadt has a large know-how in electro-chemistry and electroplating techniques. A technological process was set up and established that includes the processes available at the VUT (Vienna University of Technology) and Happy Plating.

A Si(100) wafer is utilized as substrate. The surface of the wafer is oxidized with a 240 nm thick SiO₂-layer by a plasma enhanced chemical vapor deposition at 120°C. This oxid acts as electrical insulation for the electrical readout of the devices and also as etch stop for a subsequent plasma etch process. A resist (AZ5214) is spun on the surface at a maximum rotation speed of 3000 rpm for 40 sec and dried at 107°C for 5 min on a hotplate (Sawatec). This resist is exposed to UV-light (365 nm, Maskaligner, MA150) through the mask, holding the anchor areas of the structure to the substrate. The resist is developed with AZ826MIF by spray development for 60 sec. 50 nm chromium and 200 nm copper are evaporated and structured with a lift-off process. This metal layers act as adhesive layer between the Si substrate and the electroplated Ni. After finishing the lift-off and removing the resist, the whole wafer is coated with 2 nm Ti and 400 nm Cu. The titanium improves the adhesion of the Cu layer, which serves as seed layer for the electroplating process. A special galvanic resist (AZ125nXT) defines the structures and openings for the galvanic process. The resist is applied in two layers, each spun at a maximum velocity of 3000 rpm for 30 sec and dried at 120°C for 6 min on a hotplate (Sawatec). To prevent sticking of the wafer to the mask during the exposure within the mask aligner, Aquatar is spun on the wafer at 1500 rpm. This liquid reduces the adhesion of the surface of the resist. Afterwards, the resist is exposed to UV-light (365 nm, MA150) for 200 sec through a mask, defining the final Ni structures, and is spray developed with AZ826MIF for 50 sec. The rim of the wafer is kept free, so that the seed layer can be contacted for the galvanic process.

The following electroplating of the Ni is carried out at the laboratories of Happy Plating GmbH. The wafer is mounted on a wafer holder

⁴The section is partly published in [103, 115].

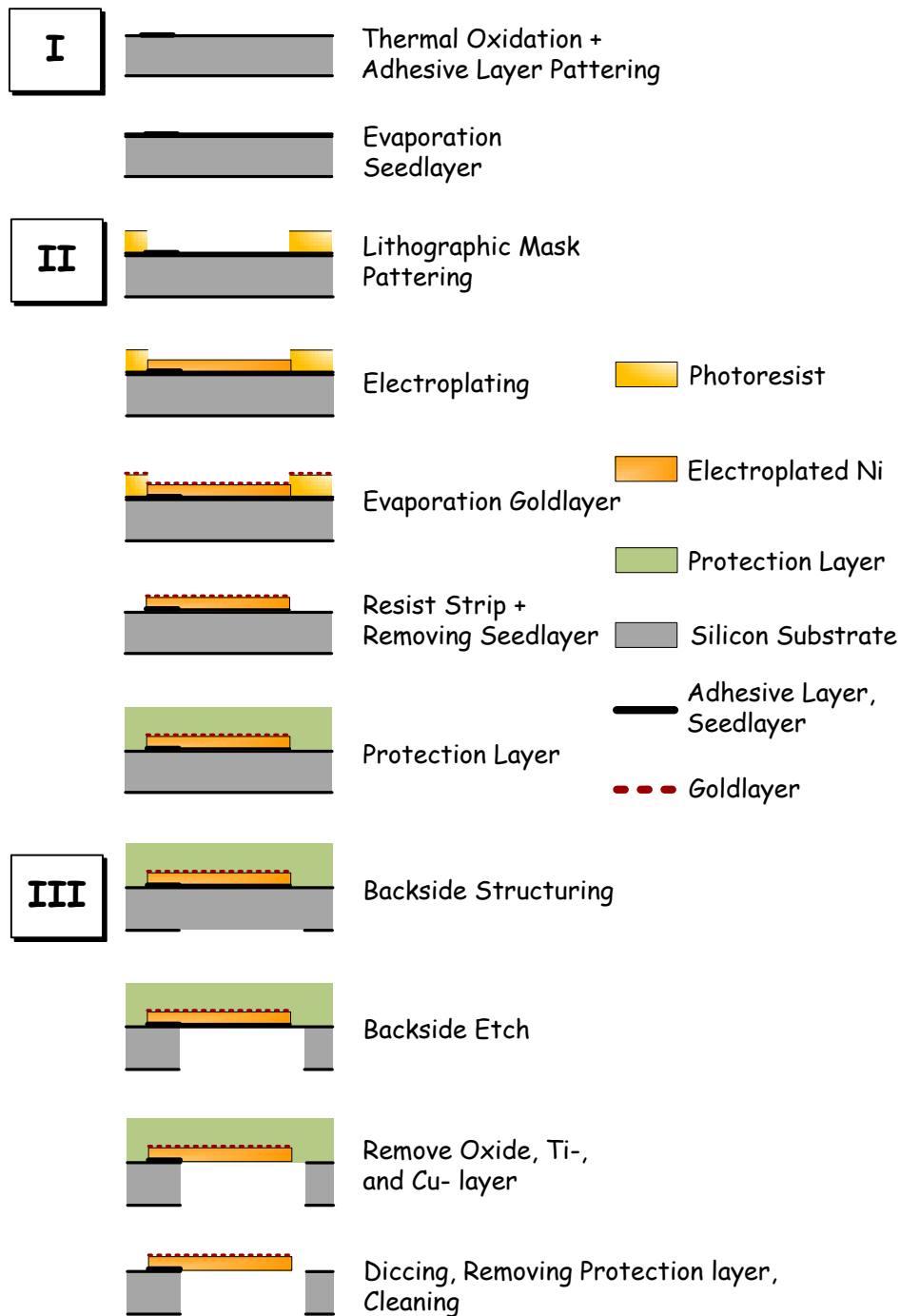


Figure 4.12: Process flow of structures with electroplated Ni. After applying the adhesion/seed layer and structuring the galvanic resist, the Ni is deposited with an electroplating process. The silicon substrate is etched from the backside to release the structures .

with circular arranged spring supported electrical connections. It is pre-treated in a 1,0 vol% sulfuric acid and rinsed with DI water to remove organic contaminations and surface oxides and to improve the electroplating process. Subsequently, the wafer holder is mounted in the galvanic bath (nickel sulfamate electrolyte, 1.27 mol/l Ni with a conductivity of 0.2 S/cm). The bath is heated up to 42°C. The anode is an insoluble iridium coated titanium sheet and is placed coplanar to the wafer surface in a distance of 10 cm. The current for the plating process is pulsed with a frequency of 80 Hz. A computer controlled pulse reverse power supply system (Plating Electronic pe86) applies a maximum current density of 1.1 A/dm². The ratio cathodic/anodic pulse current density varied from 1 to 0.2. For a homogenous layer growth, the current density is ramped up over 45 min until the maximum current density is reached. This peak current is kept for 1 h 15 min, resulting in a Ni height of 35-38 µm. Care must be taken, that the Ni height is smaller than the height of the resist. Otherwise, the overgrow will lead to undefined structure geometries.

When the galvanic process is finished, the whole wafer is coated with 50 nm Cr and 120 nm Au. The Cr acts again as adhesive layer and the Au is used later on for the wire bond for the electrical readout. The galvanic resist exhibits an almost vertical sidewall slop that allows for a lift-off of the thin metal layer. Subsequently, the resist is removed with Technistrip P1316 at 65°C, supported by an ultrasonic bath for 3 min. The Cu seed layer is removed with 20% sodium persulfate, dissolved in water, and the etch solvent is applied for 3 min. The residual solvent is removed by rinsing with DI water. The front side of the wafer is coated by spray coater with AZ4562 four times. After each coating step, the layer is hard baked at 90°C for 3 min (hotplate Sawatec). When the final layer is applied, the whole resist is hard baked at 90°C for 10 min. This resist protects the surface from contaminations and acts as mechanical support for the structures during the release from the backside and the wafer cutting.

The backside of the wafer is cleaned with an O₂ plasma for 10 min (STS, 200 W, 150 mTorr). A photoresist (AZ6624) is spun two times at 3000 rpm for 40 sec on the backside. It is exposed to UV-light (365 nm, EVG601) for 20 sec with a mask, defining the openings beneath the structures. It is developed with AZ826MIF for 30 sec. The Si substrate in this openings is etched with a DRIE process (BOSCH process, 1300 cycle, Oxford Instruments). The etching stops on the silicondioxide layer. The SiO₂ and the 2 nm Ti layer is removed in a chemical wet etch step using buffered hydrofluoric acid (HF). The residual Cu seed layer beneath the

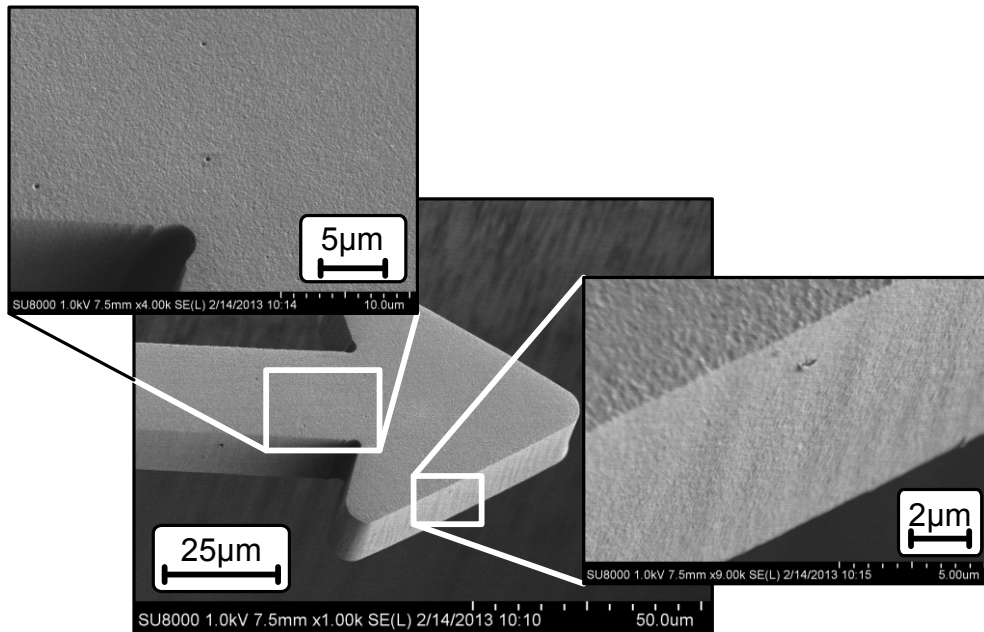


Figure 4.13: SEM micrographs of the manufactured structures. The plated Ni is homogenous, smooth and pore free.

structures is again etched with 20% sodium persulfate. Subsequently, the wafer is cut and the protection layer is removed with a 5% potassium hydroxide solvent. A number of single dies is bonded to a print by thermal wire bonding with gold wires. Figure 4.12 summarizes the process, where the roman numbers indicate the number of the masks needed to pattern the adhesive layer, the galvanic resist, and the backside.

Results

The manufacturing of thermal actuators was successfully with the described technology. After solving some minor problems, described subsequently, it was possible to manufacture micro structures made of Ni, up to a layer height of 38 μm. The surface of the plated Ni is smooth and dense, also the sidewalls, which are almost perpendicular to the wafer surface. The material is homogenous and pore free. Small features are well mapped from the lithographic mask to the resulting structures, indicating a uniform layer growth. Figure 4.13 highlights this by scanning electron microscope images of the manufactured structures, with detailed view of surface and sidewall of the Ni layer.

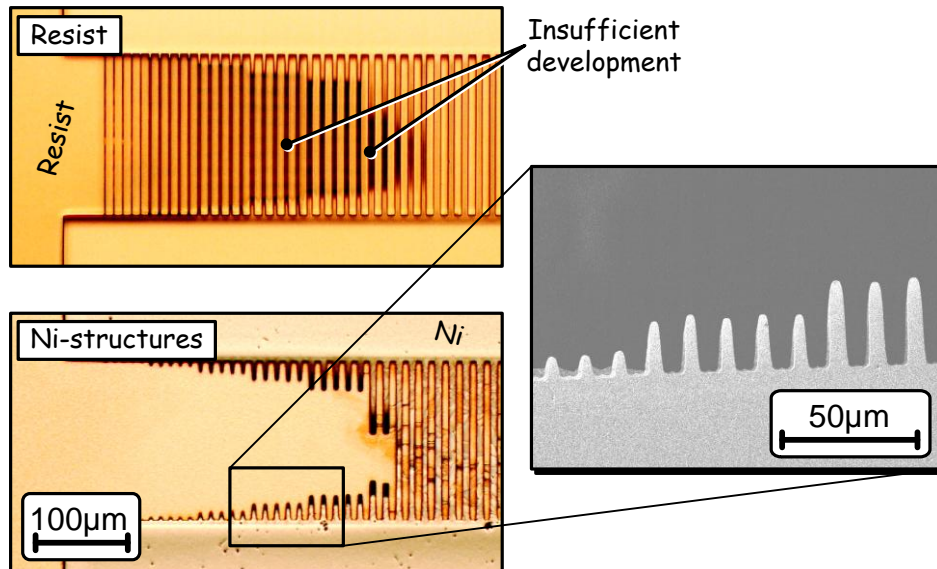


Figure 4.14: Optical micrograph of the resist and the electroplated structures, as well as an SEM image of the manufactured Ni-structures. The quality of the lithography becomes insufficient for a beam width, smaller than 6μm, indicated by the dark areas between the parallel beams. The galvanic process fills the small remaining stumps, as depicted in the SEM image.

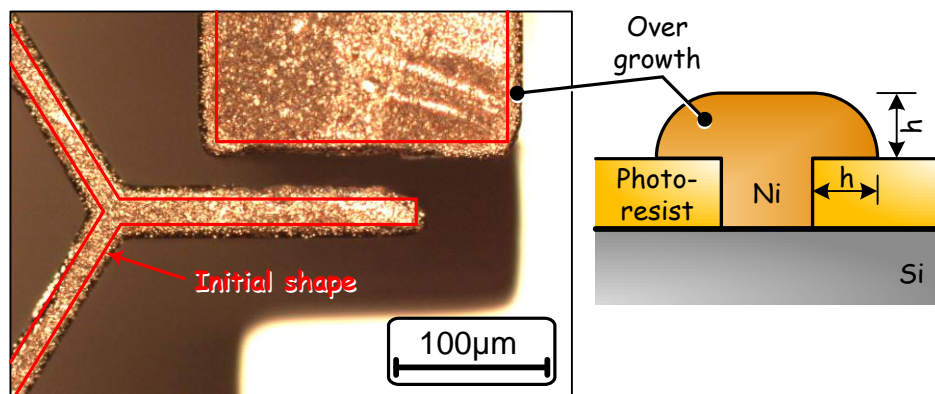


Figure 4.15: Optical micrograph of a structure with over grown Ni. The picture on the right hand side shows a schematic cross-section.

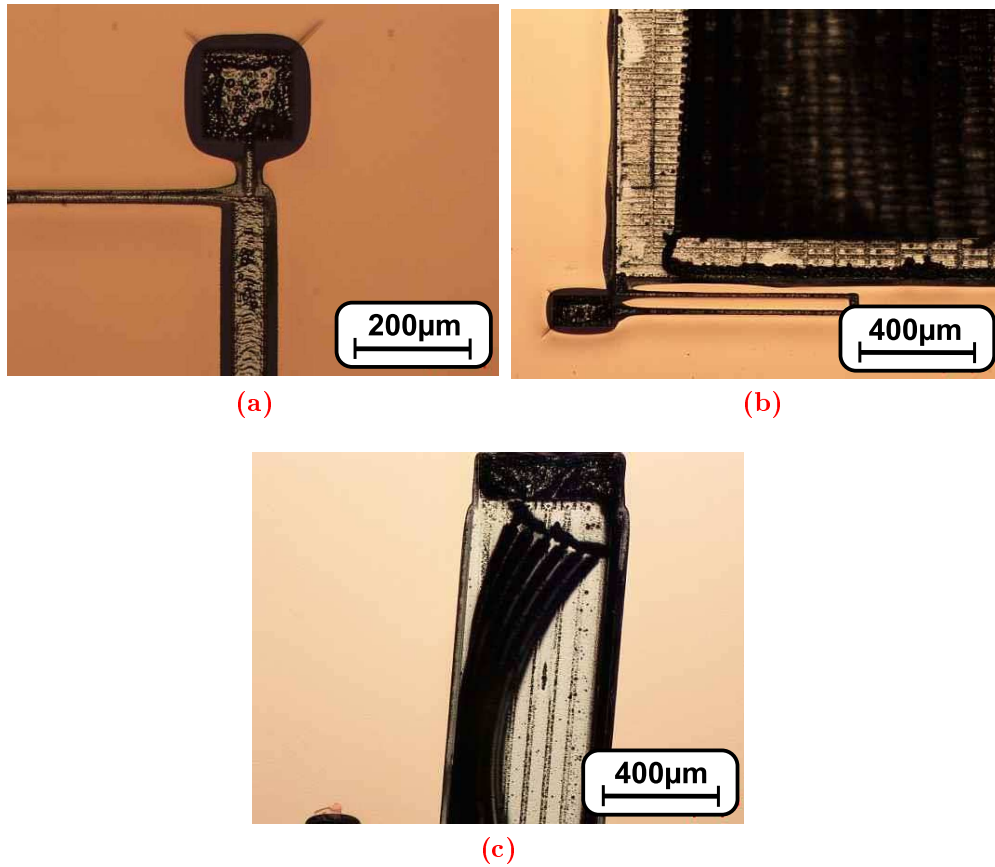


Figure 4.16: Optical micrographs of structures after the electroplating process. (a) The Cu layer is under etched beneath the resist due to adhesion problems of the resist. (b) and (c) The resist is partly peeled-off during the electroplating due to a weak adhesion and, subsequently, the whole structure is peeled-off. A fresh Ni layer grows beneath the lifted structures.

Aspect ratio: It was found, that the aspect ratio is limited by the lithography of the galvanic resist, rather than by the electroplating process itself. Parallel beams with increasing width were designed to investigate the limits of the process. Five beams are grouped up and the width of the beams in each group is increased in steps of $1\text{ }\mu\text{m}$. The quality of the lithography becomes insufficient for beam width, smaller than $6\text{ }\mu\text{m}$ (Fig. 4.14). Two of the five $6\text{ }\mu\text{m}$ width beams are insufficient developed. The galvanic process fills also the stumps, smaller than $6\text{ }\mu\text{m}$. The total resist height is $40\text{ }\mu\text{m}$, resulting in an aspect ratio of 1:5.7 for a beam width of $7\text{ }\mu\text{m}$, limited by the lithographic process. Figure 4.14 shows an optical micrograph of the structured resist, and an image of the electroplated beams after removing of the resist. The detail depicts an SEM micrograph of the stumps for beam width smaller than $6\text{ }\mu\text{m}$.

Layer height: It is important that the Ni height is smaller than the resist height and the Ni layer is sufficiently high for thermal actuators ($>20\text{ }\mu\text{m}$). If the duration of the electroplating process or the current density is chosen too long or high, respectively, the Ni will grow above the resist. The Ni-growth is isotropic, so once the height of the resist is reached, the Ni will also grow perpendicular to the surface, leading to a mushroom shaped geometry. The broadening of the structure is equal to the height h that the Ni layer exceeds the resist. Figure 4.15 depicts an optical micrograph of a structure with such an over grow. The initial shape of the geometry is marked by red lines, at which the over grown regions are partly broken-off, resulting in jagged edges. The deposition time was varied and the corresponding layer height was measured with white light interferometry (MSA400) to determine the deposition rate.

Adhesion: The adhesion of the resist to the substrate has to be sufficiently large. The growing Ni layer imposes compressional forces during the electroplating process that act against the adhesion and try to peel-off the resist from the substrate. When the interface fails, the galvanic bath creeps under the resist, leading to undefined electrochemical conditions. It was observed that the Cu seed layer is etched (Fig. 4.16a) in such situations. Also whole structures can be peeled-off the substrate. Underneath these structures, a fresh, smooth Ni layer is grown (Fig. 4.16b and c). The peeled-off structures lead to undefined current densities and, therefore, to unwanted partly increased or decreased deposition rates. This problem can be solved by using a chemical, which promotes the adhesion strength between resist and substrate. ◀◀

"No matter what the experiment's result, there will always be someone eager to: (a) misinterpret it. (b) fake it. or (c) believe it supports his own pet theory."

Finagle's Second Law

"Count what is countable, measure what is measurable, and what is not measurable, make measurable."

Galileo Galilei

5 Characterization Methods or The Art of Reproducible Results

WHETHER a measured value is plausible or not depends strongly on the chosen method and the quality of the measurement setup. Providing reproducible conditions and precise quantities that have to be measured is the most important task in metrology. Hence, a lot of resources were allocated to the design of proper measurement setups, especially for the temperature control chamber needed in the project. There are often commercial solutions on the market for different measurement tasks, but they are commonly too expensive or too restricted for scientific applications.

The characterization methods used for measuring different material parameters, the temperature dependent deflection of the actuators, and the electrical readout setup are summarized and explained in the following chapter.

5.1 Deflection

The temperature dependent deflections of the structures are measured by applying a set of temperature levels to the structures, taking snapshots of the occurring deformations, and quantifying the deflections by image processing.

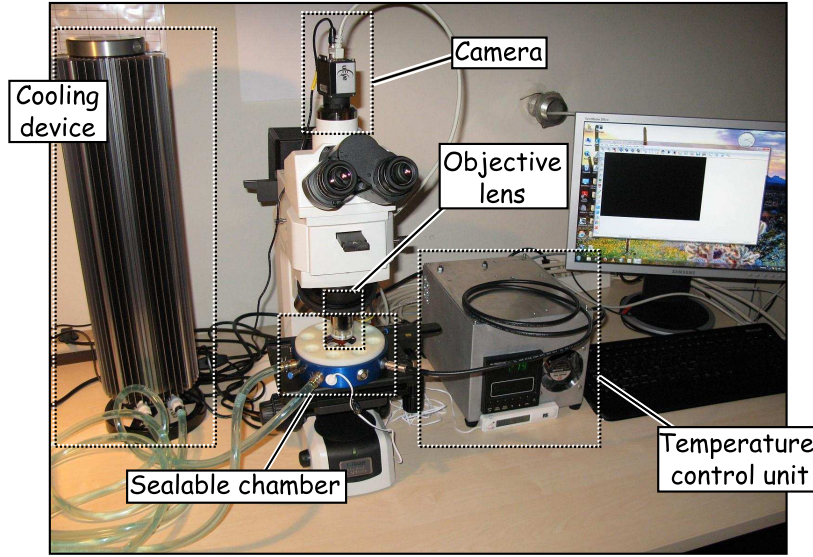


Figure 5.1: Test setup with sealable chamber, microscope with long working distance objective lens, camera, cooler/heater, and temperature control unit.

5.1.1 Temperature Setup¹

A temperature control chamber is constructed to quantify the deflections of the structures. The temperature is set by a Peltier-element and the deflection is recorded via an optical microscope and a video camera. The mechanical part of the setup consists of a sealable, a circular shaped aluminum chamber with an optical inspection window, a Peltier-element supplied by a temperature control unit, a cooling device, a microscope with a suitable objective lens, and a camera. The entire setup is depicted in Figure 5.1. The chamber is gas-tight to obtain reproducible environmental conditions down to temperatures below 0°C and it can be purged with N_2 to prevent water condensation on cold surfaces. It exhibit an outer diameter of 130 mm and the topside is closed by a polypropylene (PP) cap, featuring a 6 mm thick inspection window (Fig. 5.2). The bottom of the chamber holds a serpentine cooler that is connected to a commercial, passive water cooling device (Zalman, Reserator 1 Rev. 2).

A two stage Peltier-element (Global Component Sourcing, ET2-196-19-14) with a PID temperature control unit is used to heat up and cool down the test specimen. The Peltier-element has a thermal power out-

¹The section is partly published in [97].

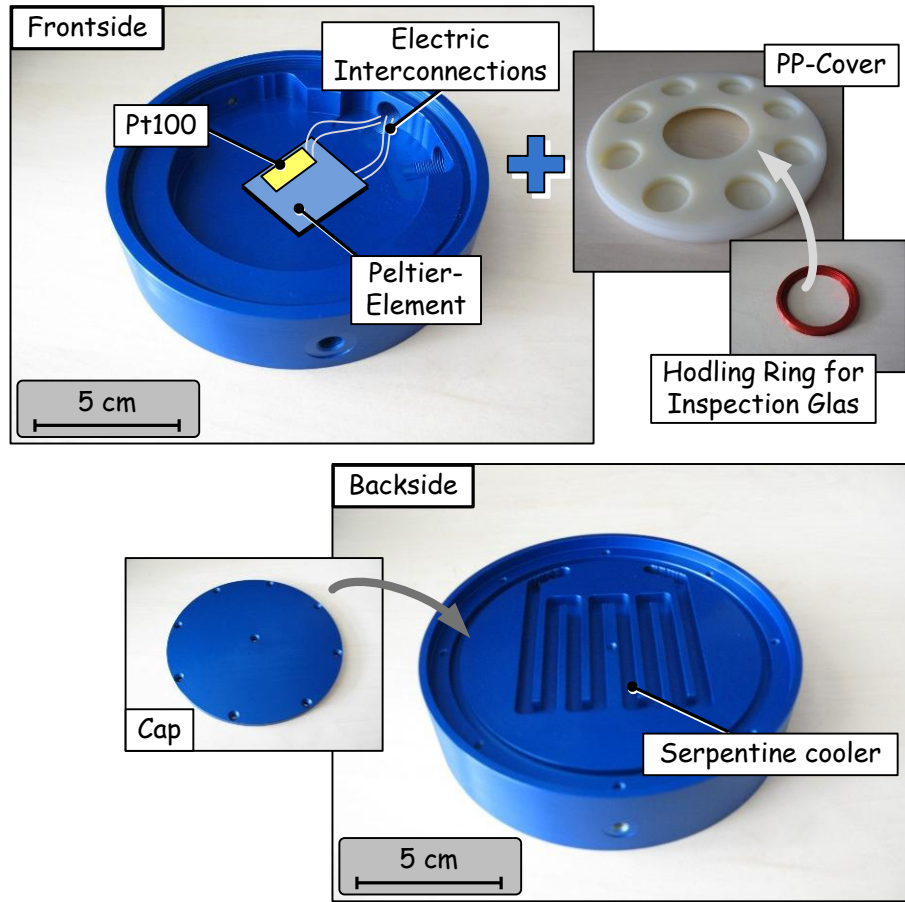


Figure 5.2: Photography of the chamber that is manufactured of aluminum and closed with a polypropylene cap. The bottom of the chamber holds a serpentine cooler.

put of 51.6 W and can generate a theoretical temperature difference of 80°C between its top and bottom side at a maximum current of 8.5 A. The electrical interconnections have six braids that can carry a maximum current of 6 A each. Hence, four braids (two for positive and two for negative connections) are used for powering the Peltier. A single communicating loop controller (Eurotherm 820) is used as control for the Peltier-element, where a Pt-100 resistance thermometer delivers the input for the control loop. The Pt-100 is located on the topside of the Peltier-element, next to the test specimen. The bottom side of the Peltier is set to room temperature with a commercial water cooling device and a cooling serpentine inside the bottom of the chamber. The overall height of the sealed chamber is 3.5 cm and is used in combination

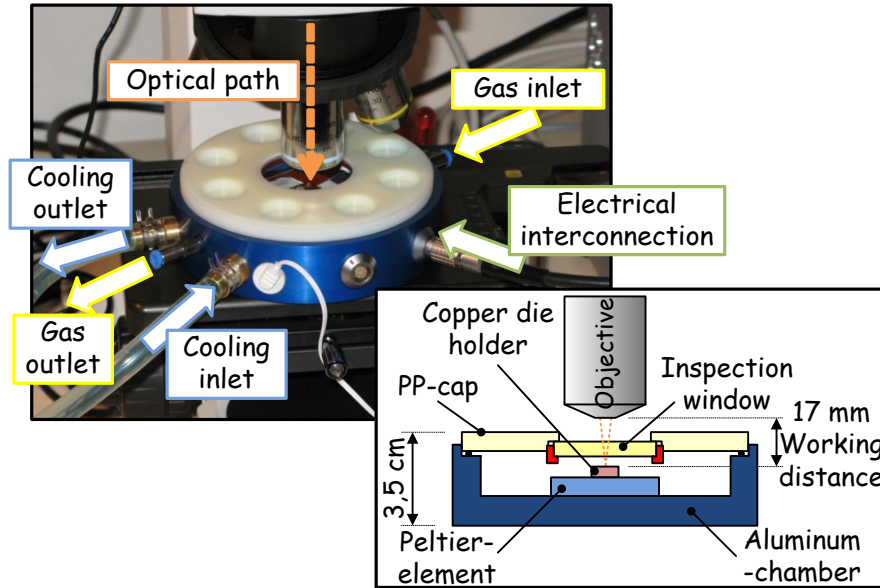


Figure 5.3: Detailed view of the chamber beneath the microscope with its water, gas, and electrical connections. The cross section reveals the total height of the chamber of 3.5 cm.

with a Nikon microscope (Nikon Eclipse LV150) and an objective lens with an extra long working distance (Nikon, CFI Plan SWLD50x EPI). A detailed view of the chamber beneath the microscope and a cross section is depicted in Fig. 5.3.

The chamber is loaded with the test die, closed, and purged with N_2 for 1 min to get rid of residual humidity. The temperature is changed in steps of 10°C between $+40^\circ\text{C}$ to -30°C . A dwell time of 30 seconds is waited for each temperature before an image is taken with the camera system (IDS GigE μEye SE). This ensures that the Peltier-element has reached the desired temperature and a homogenous temperature distribution on the topside of the structure. A temperature cycle is applied, starting at $+20^\circ\text{C}$, heating up to $+40^\circ\text{C}$, cooling down to -30°C and heating up again to $+20^\circ\text{C}$. In this way, possible hysteresis effects can be uncovered.

Residual Humidity: When the measurement chamber is insufficiently purged with N_2 , the residual humidity can condense on cold surfaces. Figure 5.4 shows a set of images of the topside of the Peltier-element at -20°C . After the condensation of water is observed (0 min), the chamber is purged again with nitrogen. At first, the water condensation increases. It can be assumed that some dead volumes of the inlet pipe and valves

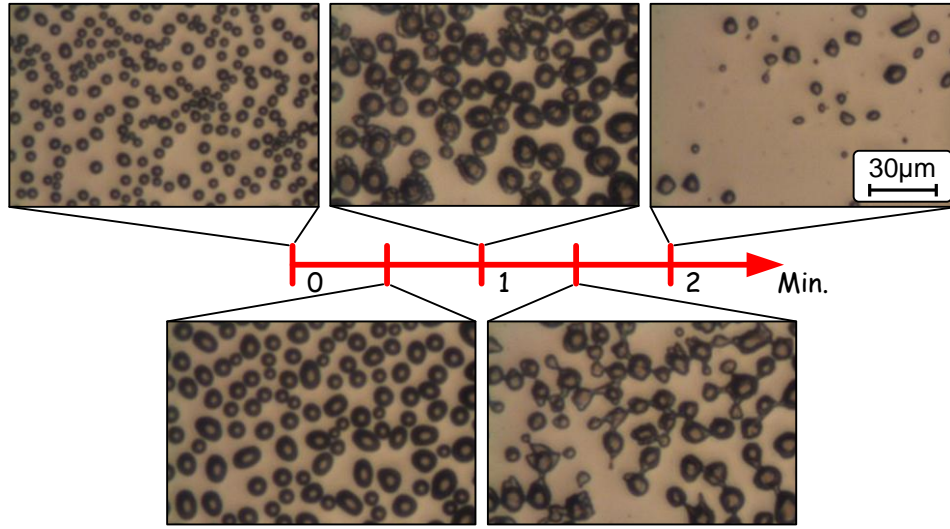


Figure 5.4: Insufficiently N_2 flushing leads to condensation of water on the cold surface of the Peltier-element. Further purging with nitrogen leads in the first minute to an increase of the condensed water before the frozen ice sublimates and vanishes.

holds a higher humidity. After one minute, freezing of the droplets can be observed. Subsequently, the frozen water sublimates and vanishes.

The Mollier²-diagram reveals that the absolute humidity must be higher than 1 g/kg water in dry air to start condensation on a surface at -20°C and 1 bar air pressure. After the re-purging with N_2 , the absolute humidity drops below this level. Otherwise the frozen water would not sublimate.

5.1.2 Image Processing³

The deflection of the tip of the structure is measured by calculating the pixel shift between images of the tip of the structure that are taken at different temperatures (Fig. 5.5). A combination of Matlab and Python scripts is used for the evaluation of the pixel shift. Specific areas (regions of interest) are marked manually in the images that define fixed areas and areas with the movable tip of the structures. For an image, taken at a specific temperature, the sum of the differences of the grey values D_1 of the actual picture and a reference image (taken at room temperature) is calculated. The region of interest is shifted pixel wise about p_k along

²Richard Mollier, German physicist, 1863-1935.

³The image processing bases on the work of [116].

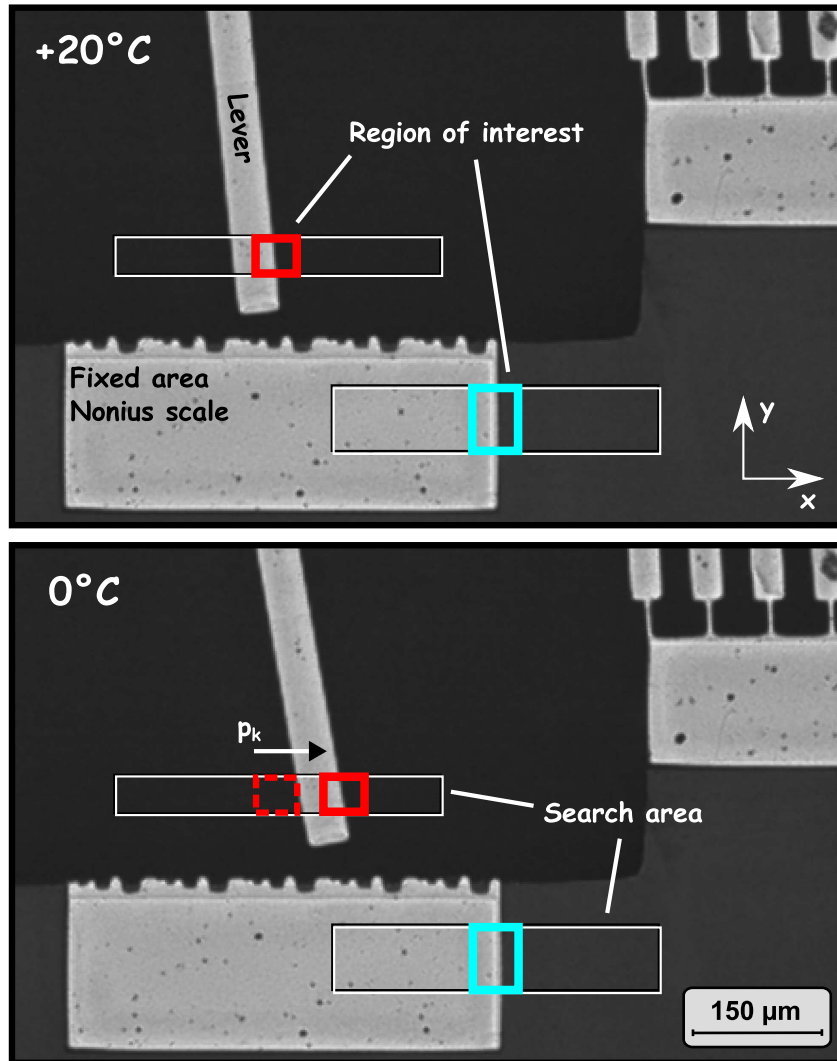


Figure 5.5: Micrographs of the tip of a Ni structure at the reference temperature of $+20^{\circ}\text{C}$ and at 0°C . The deflection is quantified by the pixel shift of the moving lever.

the x -direction and the difference in the sum of the gray values $D_1(p_k)$ is calculated for each shifted pixel to be

$$D_1(p_k) = \sum_{x_i y_j} G_1(x_i, y_j) - \tilde{G}_1(x_i - p_k, y_j) \quad , \quad (5.1)$$

where x_i and y_j is the pixel number in x and y -direction and G_1, \tilde{G}_1 are the gray values of the pixels. The minimum difference indicates the deflection of the tip. It is assumed that both image sections are as similar as possible when the minimum in the difference D_1 is reached. To increase the resolution of the method, the zero point is interpolated between the values of p_k where D_1 changes its sign. In this way, the spatial resolution of the method can be increased.

The whole chamber drifts relative to the microscope due to forces caused by the water, gas, and electrical connections. Also a mechanical drift of the test specimen on the Peltier-element is observed. The test specimen is located on a Cu die holder and the holder is connected to the Peltier with a thermally conductive paste. The viscosity of the past reduces at higher temperatures, resulting in a slow moving of the die holder. Hence, a rough 2D search of the pixel shift of the fixed area is carried out. The images are cropped accordingly to remove this drift. Afterwards, the movement of the lever in x -direction is evaluated with a higher resolution. Again, also the movement of the fixed area is evaluated, even it is almost negligible. The difference between the movements of the fixed area and the lever reveals the effective deflection of the tip.

5.2 Intrinsic Stress⁴

The active material (Ni, SU-8) has a non negligible intrinsic stress due to the fabrication processes. At first, the structure is fixed to the substrate, but when the substrate is etched away the intrinsic stress is released, leading to an initial deformation. This deformation has to be taken into account during the design. Hence, test structures are used to quantify these initial intrinsic stresses for each individual technological approach. For the very first approach, V-shaped beams with different tilting angles are utilized for the evaluation of the stress (Fig. 4.4). Later on, already existing mask and designs are exploited for this purpose. Figure 5.6 depicts a micrograph of a deflected tip compared to its designed initial

⁴The section is partly published in [103, 106, 107, 115].

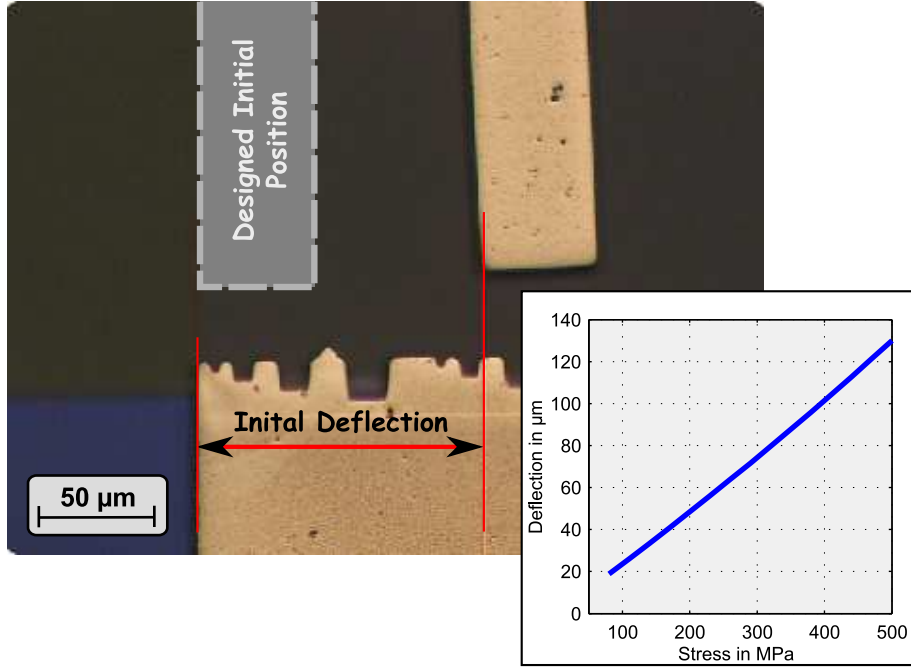


Figure 5.6: Micrograph of the tip of a released Ni structure at a temperature of 21°C. The intrinsic stress leads to an initial deflection compared to the designed initial position. FEM simulations are carried out, where the intrinsic stress is varied until the measured deflection is reached.

position and a diagram of the simulated deflections at different stress levels.

An image at the constant clean room temperature of 21°C is taken after the fabrication process of the devices. Afterwards, the deformed shape is compared to the proposed design. In a 2D COMSOL model the intrinsic stress is adapted to achieve the measured deformation. This stress is used further on to adapt the design for the corresponding technological processes. Due to Hooke's law, the intrinsic stress is directly proportional to the Young's modulus. Hence, also the Young's modulus of the material used as actuator has to be determined.

5.3 Young's Modulus⁵

The Young's modulus is estimated by measuring the resonance frequency of cantilevers. A set of cantilevers with different lengths l is designed,

⁵The section is partly published in [103, 115].

where the length is incrementally increased. A piezoelectric shaker excites the cantilevers sinusoidal with frequencies in the range from 1 kHz to 1.5 MHz. The excitation amplitudes and the vibrations of the cantilevers are measured with a laser Doppler⁶ vibrometer (MSA400, Polytec). The MSA400 also provides the electric power and signal for the piezoelectric shaker (Fig. 5.7). In this way, the resonance frequency of the first, second, and third vibrational mode of the cantilevers is evaluated. The results are compared to an analytical model of the natural frequency and the ratio E/ρ in the model is adapted to fit the measurement, where ρ is the density and E the Young's modulus of the cantilevers. The Euler-Bernoulli beam theory describes the i -th natural frequency of a single clamped cantilever by

$$f_i = \frac{1}{2\pi} \left(\frac{\gamma_i}{l} \right)^2 \sqrt{\frac{E}{\rho} \frac{h^2}{12}} \quad (5.2)$$

where γ_i is 1.875, 4.694, and 7.855 for the first, second, and third mode, respectively, and h is the height of the cantilever. The difference between the natural frequency and the measured resonance frequency is neglected. Another approximation is the fixed density of the material, which is taken from [86]. Hence, instead of adapting the ratio of E/ρ , only the Young's modulus is varied.

5.4 Stress Gradient⁷

Some of the technological processes lead to a vertical stress gradient within the height of the structures. It is caused by inhomogeneous process parameters during the growth of the structures, atomic lattice mismatch, and inherent surface stress of the material [117]. The stress gradient results in an out-of-plane bending of the structures and, hence, can be quantified by measuring these out-of-plane deflections. Again, cantilevers with different length are utilized and the deflections are extracted from topography measurements. A white light interference method, offered by the MSA400, gathers the topographic profiles at room temperature. The bending of the beams is numerically approximated by a third order polynomial fit and the radius R is calculated by a numerical second order derivation of the fitted data. The stress gradient Γ in Pa/m is given by

$$\Gamma = \frac{E}{R(1 - \nu)} \quad , \quad (5.3)$$

⁶Christian Andreas Doppler, Austrian mathematician and physicist, 1803-1853.

⁷The section is partly published in [103, 106, 107, 115].

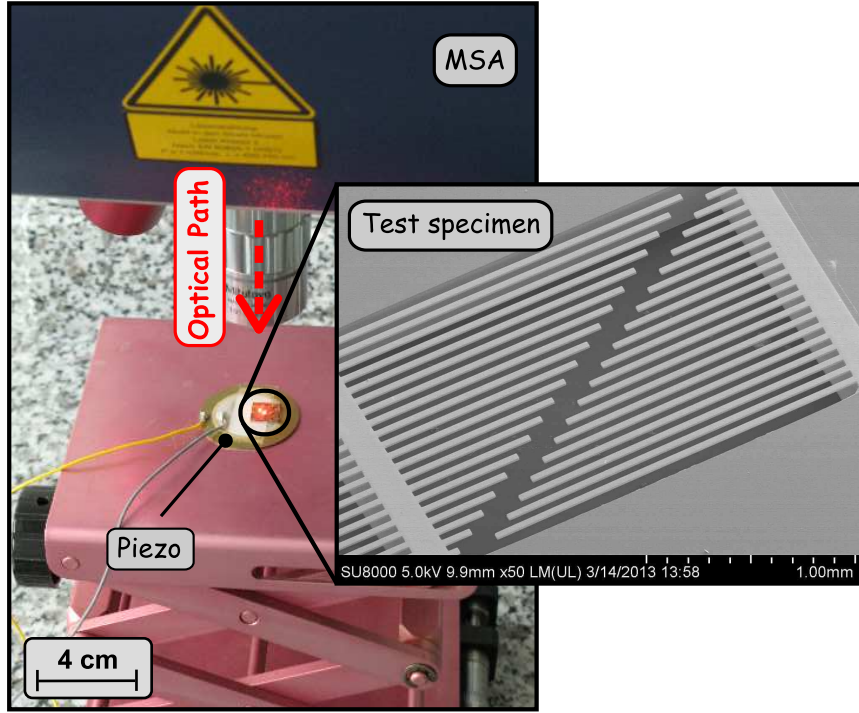


Figure 5.7: The laser Doppler vibrometer of the micro system analyzer is used in combination with a piezoelectric shaker and powering unit to excite and measure the resonance frequency of cantilevers.

as stated in [118].

Figure 5.8 depicts a raw data set of the topography measurements of the cantilever array.

5.5 Coefficient of Thermal Expansion⁸

The coefficient of thermal expansion (CTE) is indirectly quantified by numerical simulations. After measuring the deflection of the structure's tip at a set of temperature differences, the values are compared to numerical simulations. The geometry is modeled as 2D shape as stated in subsec. 3.2.2, including also the intrinsic stress. The simulated deflections at a specific temperature difference are compared to the measured deformations. Subsequently, the CTE in the FEM simulation is varied, until the values of the measurements are met.

⁸The section is partly published in [103, 106, 107, 115].

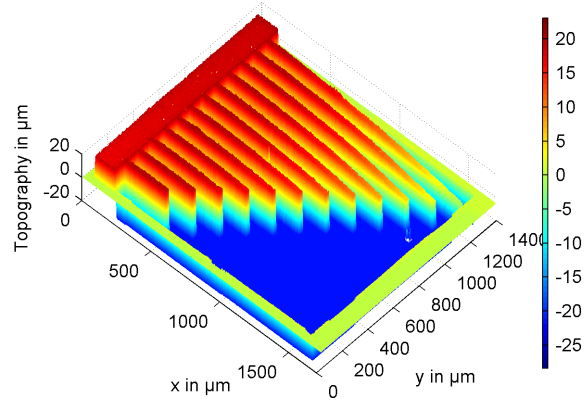


Figure 5.8: Topography measurement with the MSA reveals the of out-of-plane deflections of a set cantilevers.

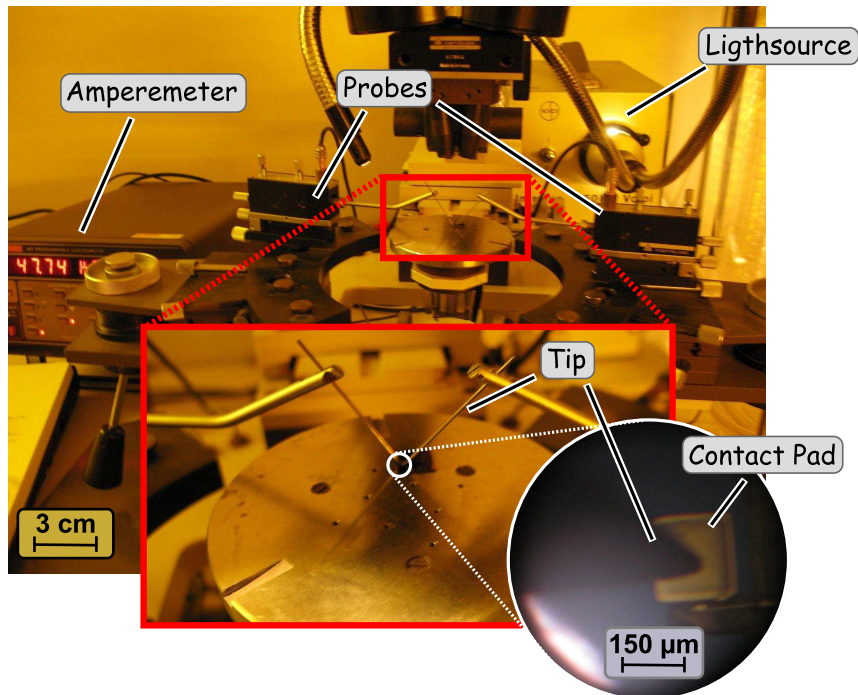



Figure 5.9: Optical micrograph of the micro-manipulator stage. The test specimen is contacted by the tips of the manipulator arms and the resistivity is measured.

5.6 Electrical Read Out

An electrical resistivity measurement is chosen as read out for the threshold sensor. When the threshold temperature is exceeded, an irreversible contact between two movable parts of the structure is established. To detect whether this contact is established or not, the electrical resistivity between the two parts is measured. After applying a full thermal measurement cycle, where the irreversible contact occurs, the test specimen is transferred to a micro-manipulator stage. The micro-manipulator probes are softly attached to the surface of special designed probing areas and the electrical resistivity between them is measured with a nano ampere-meter (Keithly 617, programmable electro-meter). A constant voltage of 50 mV is applied between the tips of the probes and the current is measured down to a range of pA. Hence, a difference of several orders of magnitude in the resistivity can be measured between a short- and open circuit condition. An optical micrograph of the stage is depicted in Fig. 5.9. The small inlays gives a detailed view on the tips of the micro-manipulator arms and a view through the ocular of the attached microscope. 

"When working toward the solution of a problem it always helps if you know the answer."

Rule of Accuracy

"2 is not equal to 3 - not even for large values of 2."

Grabel's Law

Achievements and Performance 6 or What You Expect and What You Get



SOMETIMES, the results of measurements are exactly what the operator has expected. But in general, there are surprising circumstances that have not been taken into account, which lead to strange results and a lot of headache by trying to figure out what had happened. During scientific projects the first things that have to be adapted are the initially proposed solutions and working plans. There are always newer and better ideas or inputs how to solve a specific problem, or unexpected challenges forces a change of the direction of the project.

This chapter discusses several thermal actuator designs, realized by different technological approaches, and their thermal performances. Also the characterization results of the material parameters are shown. In the end, the performance of the resulting temperature threshold sensors are depicted.

6.1 SU-8 Actuators¹

SU-8 as active material for a thermal actuator was a very promising approach because of its high CTE of $\alpha_{\text{SU-8}} = 50 \text{ ppm/K}$. But, as found

¹The section is partly published in [97].

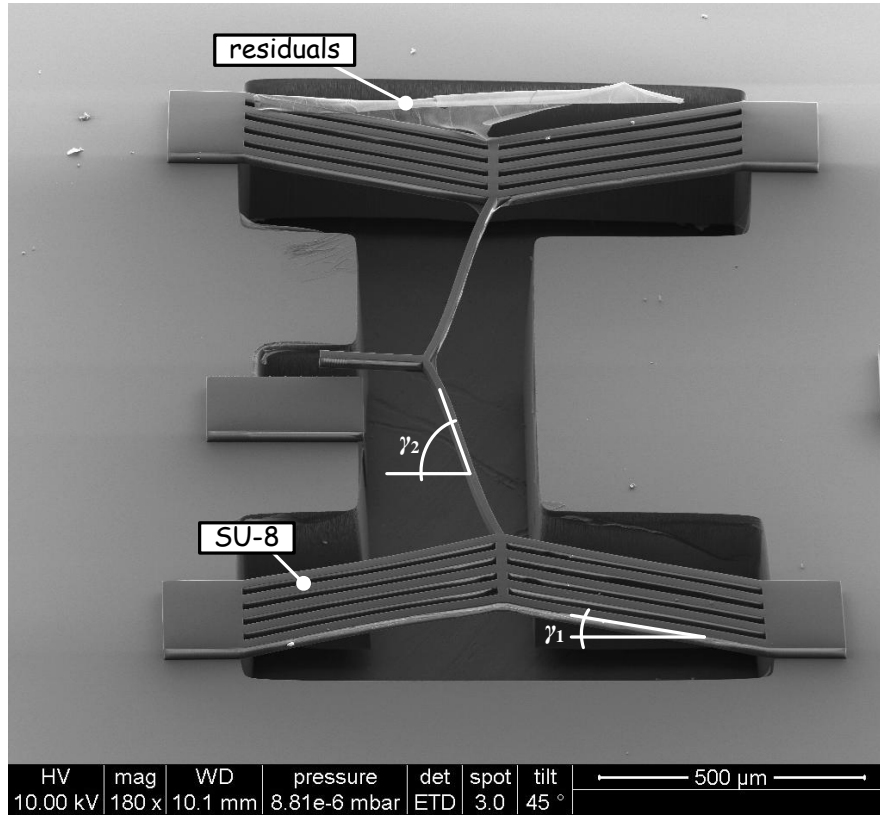


Figure 6.1: SEM micrograph of an SU-8 structure. The residuals can be removed by an O₂-plasma cleaning process and do not affect the behavior of the actuator.

in the experiments, it exhibits some unexpected non-linearity that complicates its usage for thermal actuators. These non-linearities make it extremely challenging and nearly impossible to design suitable geometries.

6.1.1 Design

The design is based on V-shaped beam stacks with cascaded V-shaped single beams (Fig. 6.1). Functional devices could be achieved by removing the substrate beneath the SU-8 structures as described in sub-sec. 4.1.3.

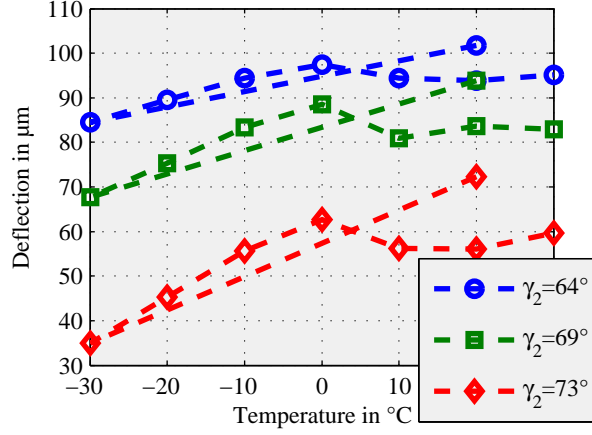


Figure 6.2: Temperature dependent deflection of the tip of SU-8 structures with different angles of γ_2 .

6.1.2 Thermal Performance

The thermal measurements reveal a non-linear behavior around 0°C. The SU-8 process relies on water dissolvable solutions and it is reported that SU-8 swells and shrinks with the water content [119, 120]. As depicted in Fig. 4.8, the material exhibits a strong shrinkage when the chamber is purged with N_2 , indicating residual water within the material. The condensation of water droplets and the growing of ice crystals was observed during the thermal measurements, even after purging the measurement chamber with N_2 . This effect indicates residual water that is released from the SU-8. The water content within the material seems also be responsible for the non-linear behavior in the range of 0°C, where H_2O exhibit a phase transition between fluid and solid. Figure 6.2 depicts thermal measurements of the fabricated structures with different inclination angles γ_2 at a set of temperatures. The temperature is changed in steps of 10 K and held for 1 min before the deflection is measured. After capturing an image at +20°C, the device is cooled down to −30°C and successively heated up to +30°C. It can be seen that there is a non-linearity occurring around 0°C.

6.1.3 Resonance Measurements

The resonance frequency of a set of cantilevers with lengths in the range from $l = 350 - 550 \mu m$ is measured as depicted in Fig. 6.3. The height of the material is evaluated with an optical white light interference method

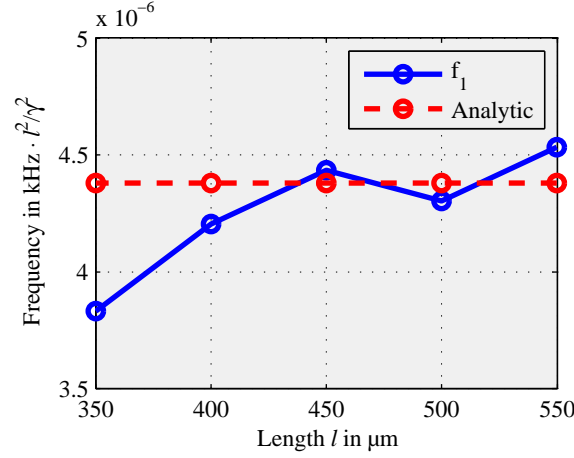


Figure 6.3: The measured primary resonance frequency of SU-8 cantilevers with different lengths is scaled with l^2/γ^2 and compared to an analytical model of the 1st natural frequency mode.

to be $h = 52 \mu\text{m}$. In accordance to Eq. 5.2, the Young's modulus is adapted to meet the measured frequencies, while the density is set to be $\rho = 1190 \text{ kg/m}^3$. A Young's modulus of $E_{\text{SU-8}} = 4 \text{ GPa}$ is calculated, which is in good agreement to the reported Young's modulus of the material [88, 121].

6.2 Ni Actuators

Due to the disappointing results with SU-8 as active actuator material, a commercially available process offered by Europractice is used for a proof of concept of the thermal actuators. The design iteration after proofing the concept is fabricated with the galvanic process of Happy Plating, whereas the rest of the manufacturing process is carried out at the laboratories of the Vienna University of Technology.

6.2.1 Europractice²

The design of the structures manufactured with Europractice relies on V-shaped beam stacks (Fig. 6.4), connected to a lever transmission via coupling bars. Two different kind of transmissions are designed. For the first one, the coupling bars are directly connected to the lever (**B**-type,

²The section is partly published in [106, 107].

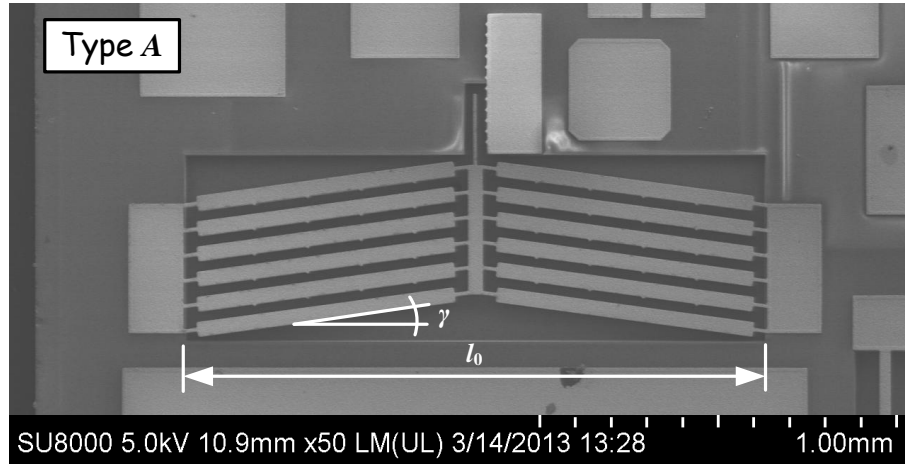


Figure 6.4: SEM micrograph of a single V-shaped beam stack (**A**-type).

Fig. 6.5) and for the second one the coupling bars are connected via a thin bridge and the lever is pinned to this bridge (**C**-type, Fig. 6.5).

The maximum occurring mechanical stress is a limiting factor in the designs and it is evaluated by means of numerical simulations. The offset between the V-shaped beam stacks l_2 strongly influences the maximum stress. This stress occurs commonly in the coupling bars and increases for smaller offset values. Figure 6.6 depicts the occurring maximum stress in dependence of the offset between two V-shaped beam stacks at a temperature difference of 40 K, compared to the corresponding simulated force-displacement product. The stress decreases for larger offset values. It reaches a minimum value above an offset of 110 μm for the depicted example. For such an offset, the maximum stress occurs no longer in the region of the coupling bar. Due to the numerical model, the stress occurs in the anchor regions, where a fixed boundary meets a free boundary and large shear stresses arise. On the other hand, the force-displacement product increases for smaller offsets until it reaches a maximum. Further decreasing of the offset results in stronger compression of the coupling bars and, hence, a break down of the lever transmission.

Actuators with different lengths and lever transmissions are compared to a single V-shaped beam stack (**A**-type). The corresponding geometry parameters, measured deflections, and simulated forces are summarized in Tab. 6.1. The measured deflections are compared to results of the analytical model and FEM simulations, where the CTE is adapted to meet the measurements. The effective CTE is found to be $\alpha_{\text{eff},\text{Ni}} = 11.7 \pm$

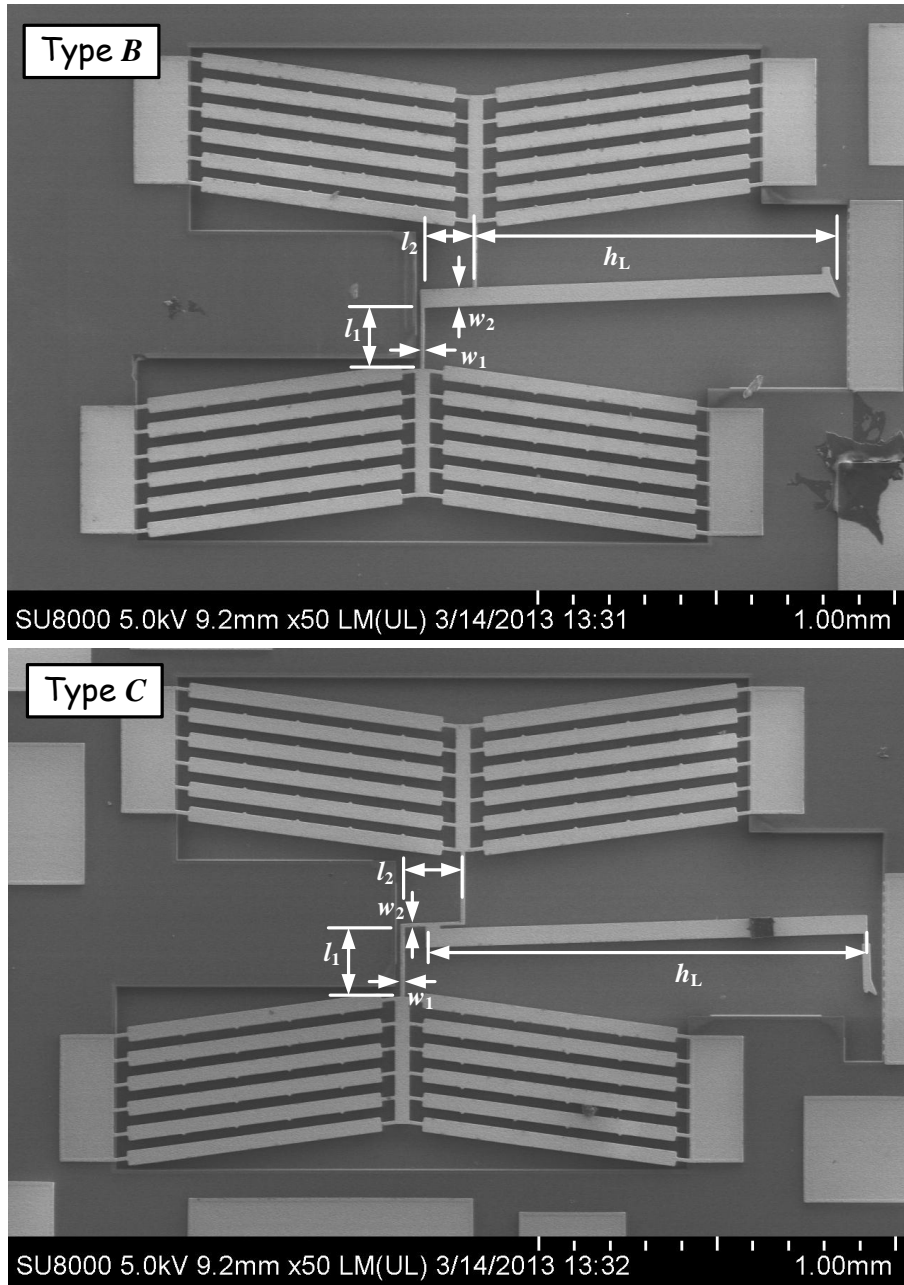


Figure 6.5: SEM micrographs of a directly coupled actuator (B-type) and a bridge coupled actuator (C-type).

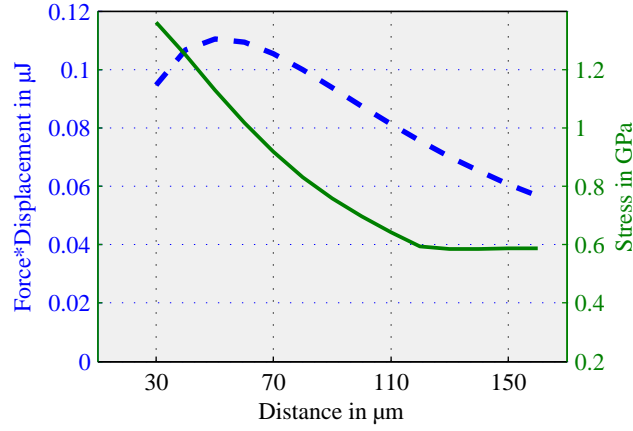


Figure 6.6: Maximum mechanical stress in dependency of the offset distance l_2 , compared to the corresponding work that the actuator can provide.

0.7 ppm/K. Considering the CTE of the Si substrate ($\alpha_{\text{Si}} = 2.6$ ppm/K, [86]) leads to a CTE of the plated Ni of $\alpha_{\text{Ni}} = 14.3$ ppm/K, which is in good agreement to that of bulk Ni ($\alpha_{\text{Ni,Bulk}} = 13.4$ ppm/K, [86]).

Figure 6.7a-c depict the measured deflection of the tip of an **A**, **B** and **C**-type actuator, compared to the numerically simulated and analytically calculated deflections. The actuators exhibit a linear temperature dependent deflection without observable hysteresis effects. Hence, it can be assumed that the stress levels are below the yield strength of the material.

The camera system has a resolution of 220 nm/px. Due to the small deflections of the single V-shaped beam stack (**A**-type), the relative measurement errors are larger.

The force-displacement product is a measure of the work the actuator can provide (Fig. 6.7d). This work is approximated by the numerically simulated displacements and forces. For the **A**-type actuator, this work is multiplied by a factor of two, for a better comparability with the other types, because those actuators comprise also two **A**-type structures.

The resonance frequency of a set of cantilevers with lengths in the range from 300 μm to 1300 μm is measured (Fig. 6.8). The height of the material is measured with an optical white light interference method and is found to be $h = 19.5 \mu\text{m}$. In accordance to Eq. 5.2, the Young's modulus is adapted to meet the measured frequencies. A Young's modulus of

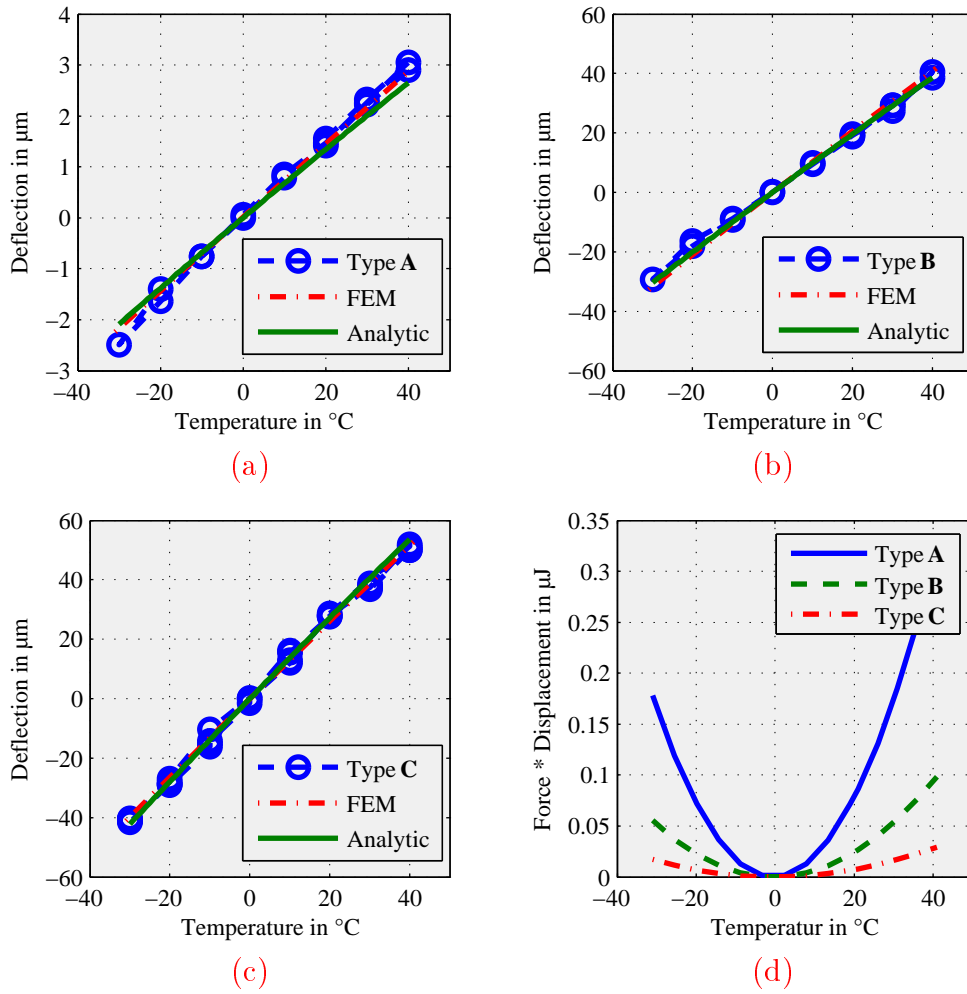


Figure 6.7: (a-c) The measured deflections of **A**, **B** and **C**-type actuators with a span of $1600\mu\text{m}$, compared to the analytically calculated and numerically simulated results. (d) The product of the simulated deflections times the simulated force is a measure for the work the actuator can provide.

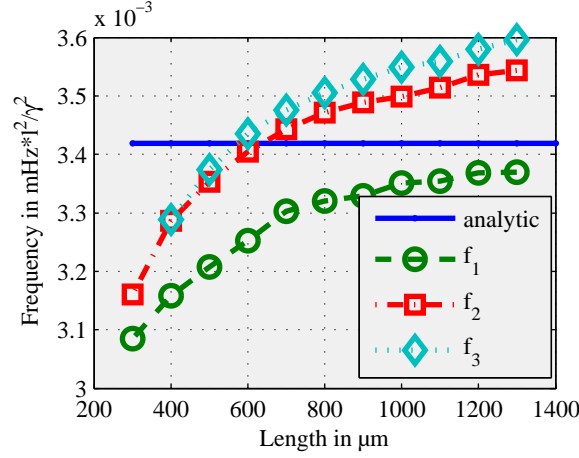


Figure 6.8: The measured values of the first, second, and third resonance frequency are scaled with l^2/γ^2 and compared to an analytical model. The Young's modulus in the model is adapted to meet the measurements.

$E = 160$ GPa is calculated, which is in good agreement to the reported Young's modulus of the material when a density of $\rho = 8900$ kg/m³ is assumed [122]. The initial deformation at +20°C is measured and the corresponding intrinsic tensile stress is varied in an FEM simulation to meet the measured deflections and is found to be $\sigma_{\text{intr}} = -200 \pm 44$ MPa. With a Young's modulus of $E = 160$ GPa, this leads to an initial shrinkage of $\epsilon = 0.13 \pm 0.03\%$.

The vertical stress gradient is calculated with Eq. 5.3 by measuring the curvature of a set of cantilevers with different lengths (Fig. 6.9). The measured topographic data is approximated with a polynomial fit of third order. The mean curvature and standard deviation is calculated with the fitted data, resulting in a vertical stress gradient of $\Gamma = 6.27 \pm 0.57$ MPa/μm.

As summarized in Tab. 6.1, doubling the span of the V-shaped beam stack doubles the thermal sensitivity and blocking forces. The lever transmission of the **B** and **C**-type actuators increases the thermal sensitivity by more than a factor of 13 compared to the **A**-type single V-shaped beam stack, but at the tradeoff of a reduced blocking force. The deformation of the coupling bars acts as a kind of energy loss and the overall force-displacement product of the **B** and **C**-type actuators is significantly reduced compared to the **A**-type single V-shaped beam stack. Furthermore, the **C**-type actuators have a higher thermal sensitivity but

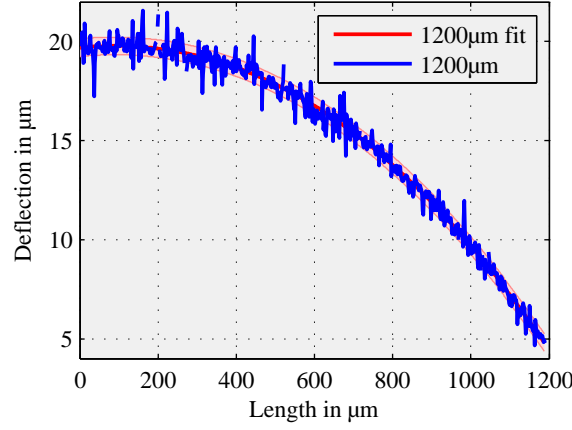


Figure 6.9: Deflection of a set of cantilevers, measured (blue) and fitted (red) by a polynomial fit of third order. The plot depicts the measured topography and the fitted data with the corresponding error bar of a 1200 μm long cantilever.

type	Design parameter						Performance			
	span	coupling bar width	coupling bar length	bridge width	bridge length	lever length	thermal sensitivity	blocking force	area	area specific work
	l_0 μm	w_1 μm	l_1 μm	w_2 μm	l_2 μm	h_L μm	d_T $\mu\text{m}/\text{K}$	F_T $\mu\text{N}/\text{K}$	A μm^2	W_{Area} $\mu\text{J}/\text{K}^2\text{m}^2$
A_I	800	-	-	-	-	-	0.04	744.3	1133×450	58.4
B_I	800	8	185	50	120	824	0.52	64.2	1430×1260	18.5
C_I	800	10	150	10	150	900	0.53	20.1	1557×1175	5.8
A_{II}	1600	-	-	-	-	-	0.07	1309.0	1927×510	93.2
B_{II}	1600	8	175	50	150	1095	1.03	56.3	2147×1369	19.7
C_{II}	1600	10	200	8	170	1220	1.31	13.4	2296×1364	5.6

Table 6.1: Geometric parameters and thermal performance of devices manufactured with the Europractice Ni-process. The inclination angle γ of the V-shaped beam stacks is 8° .

a reduced blocking force compared to the type **B** actuator and the overall force-displacement product is also lower at comparable chip areas.

6.2.2 Happy Plating³

The design of the electroplated Ni structures that were manufactured in cooperation with Happy Plating is similar to the structures of Europractice. It is adapted in accordance to the higher aspect ratio that can be achieved. Furthermore, several design variations were added to the mask set. To reduce the required chip area, only one V-shaped beam stack is connected to the lever transmission. One end of the lever is fixed via a hinge to an anchor block and the V-shaped beam stack pushes against the lever in order to achieve a lever transmission. Actuators with the topology optimized design, as described in subsec. 3.2.1, are realized and measured. Figure 6.10 depicts scanning electron micrographs of these **D**, and **E**-type actuators.

Table 6.2 summarizes the design, geometry parameters, and thermal performance of the different actuators. The inclination angle of the V-shaped beam stack for all these designs is $\gamma = 4^\circ$.

Figure 6.11a-b depicts the thermal deflection of the **D_{II}**-type actuator. It can be seen that the displacement exhibit a linear behavior, but the simulated blocking force follows a nonlinear curve with decreasing slope for increasing temperatures. The calculation of the blocking force in Tab. 6.2 assumes a linear slope between -30°C and 0°C . The **E**-type actuators exhibit a linear deflection as well as a linear simulated blocking force (Fig. 6.11c-d).

The offset length l_2 has a major influence on the lever transmission and hence on the thermal sensitivity. The optimal offset to gain the highest thermal force-displacement product is computed by means of numerical simulations. However, the occurring maximum mechanical stress has to be below the yield strength of the material. Hence, two similar structures are designed, only differing in their offset length l_2 . The measurements of the deflections of the tip of the structures revealed no observable hysteresis effects. It can be assumed that the yield stress of the material for the different designs is not exceeded in the temperature measurement range from -40°C up to $+50^\circ\text{C}$.

The resonance measurements (Fig. 6.12) revealed a Young's modulus of $E = 163 \text{ GPa}$, when a density of $\rho = 8900 \text{ kg/m}^3$ is assumed. The height

³The section is partly published in [103, 115].

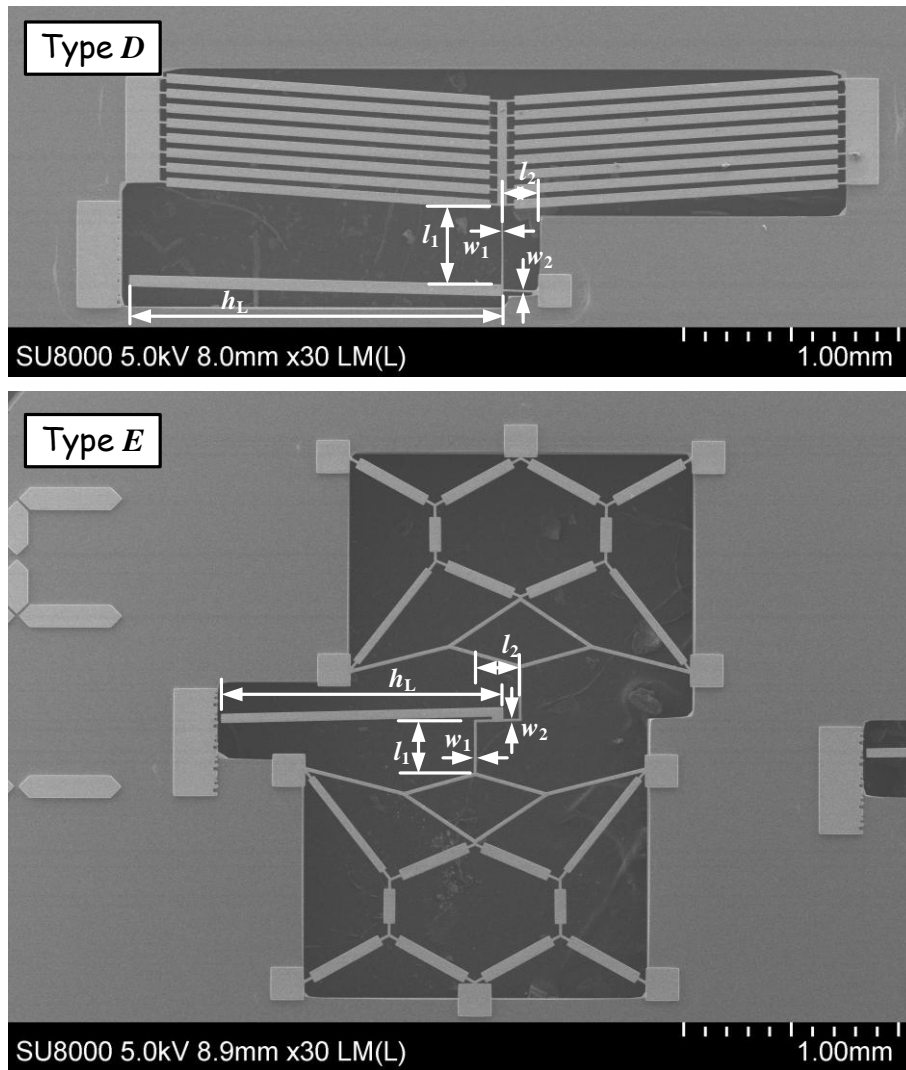


Figure 6.10: SEM micrographs of a Type D actuator and a topology optimized actuator (Type E).

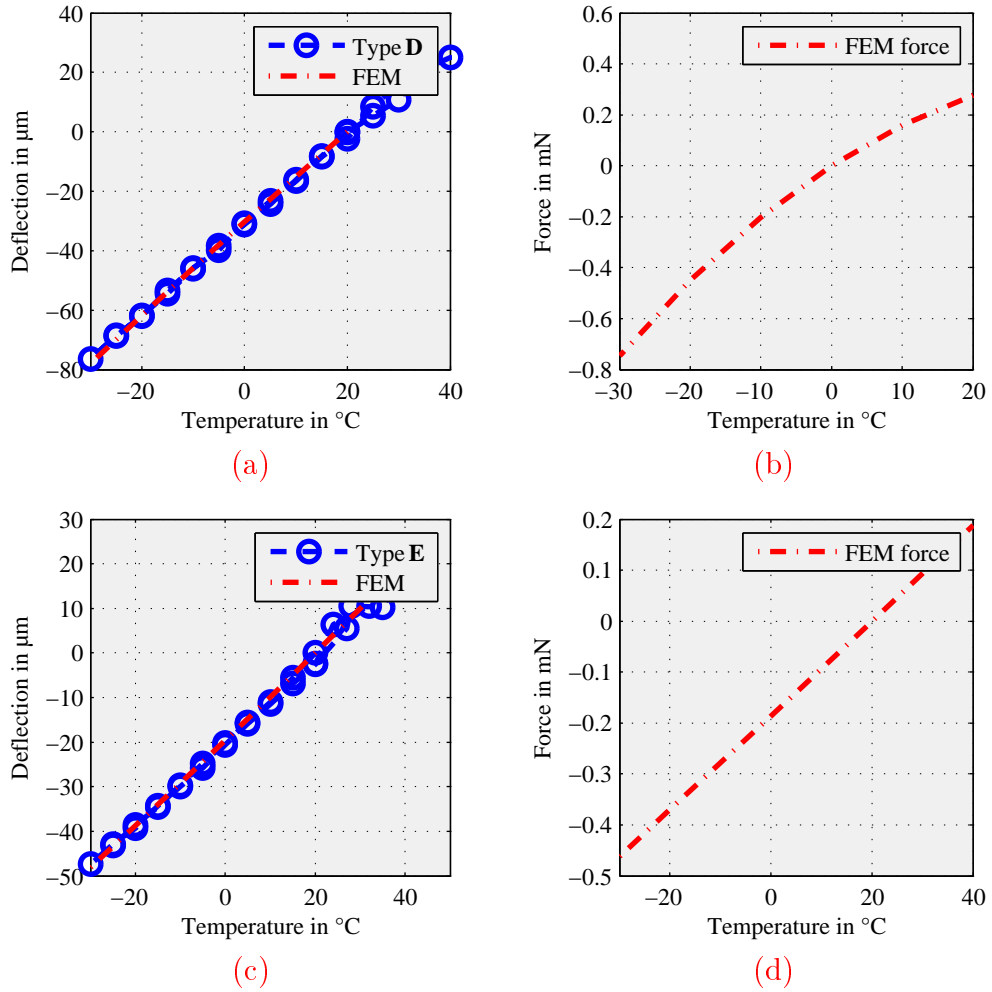


Figure 6.11: (a) Displacement and (b) simulated force of the $\mathbf{D_{II}}$ -type actuator. (c) and (d) depict the displacement and simulated blocking force of the $\mathbf{E_I}$ -type actuator.

type	Design parameter						Performance			
	span	coupling bar width	coupling bar length	bridge width	bridge length	lever length	thermal sensitivity	blocking force	area	area specific work
	l_0	w_1	l_1	w_2	l_2	h_L	d_T	F_T	A	W_{Area}
	μm	μm	μm	μm	μm	μm	$\mu\text{m}/\text{K}$	$\mu\text{N}/\text{K}$	μm^2	$\mu\text{J}/\text{K}^2\text{m}^2$
B_{III}	1600	10	475	50	100	1105	2.99	43.1	2125x1860	32.6
B_{IV}	1600	10	475	50	200	1105	1.54	57.5	2135x1860	22.4
B_{V}	1600	7	475	50	80	1113	3.62	33.6	2125x1866	30.8
B_{VI}	1600	7	475	50	150	1072	2.18	49.3	2125x1852	27.3
B_{VII}	3200	10	475	50	160	1868	5.34	33.9	3720x1996	24.4
B_{VIII}	3200	10	475	50	240	1832	4.03	35.8	3770x1970	19.4
D_{I}	3200	7	375	7	170	1750	3.00	26.2	3531x1107	20.1
D_{II}	3200	7	375	7	300	1750	1.53	20.5	3519x1107	8.05
D_{III}	1600	7	475	7	100	1450	2.47	23.6	2420x1138	21.2
D_{IV}	1600	7	475	7	150	1450	1.75	20.8	2420x1151	13.1
E_{I}	1000	10	238	10	160	936	0.96	9.5	1670x2418	2.3
E_{II}	1590	10	238	10	210	1288	1.89	8.1	2345x2770	2.4

Table 6.2: Design parameters and thermal performance of devices manufactured with the Happy Plating Ni-process (subsec. 4.2.2).

of the Ni cantilevers is measured to be $h = 16.1 \mu\text{m}$.

Furthermore, the measurements revealed a vertical stress gradient of $\Gamma = 2.64 \pm 0.36 \text{ MPa}/\mu\text{m}$ which is lower than that of the commercially available process offered by Europractice. The comparison of the topographic data (Fig. 6.9 and 6.13) shows also the smoother Ni surface of this process compared to that of the Europractice ordered devices. The intrinsic stress and the effective CTE are simulated to be $\sigma_{\text{intr}} = 142 \pm 26 \text{ MPa}$ and $\alpha_{\text{eff,Ni}} = 11.6 \pm 0.9 \text{ ppm/K}$, respectively. The corresponding initial shrinkage of the material is calculated to be $\epsilon = 0.087 \pm 0.016\%$.

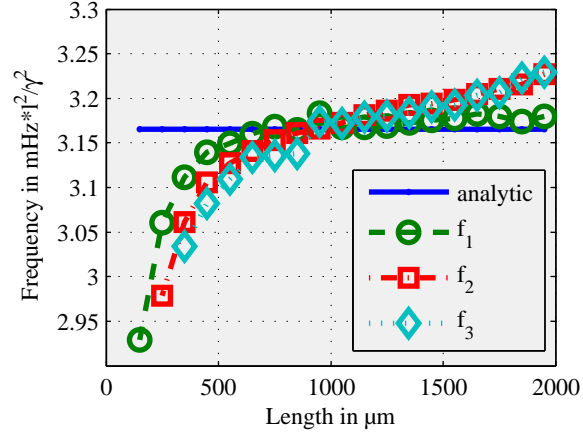


Figure 6.12: Measured first, second, and third resonance frequency of Ni cantilevers of different length, scaled with l^2/γ^2 and compared to the analytical model. The Young's modulus in the model is adjusted to meet the measurements.

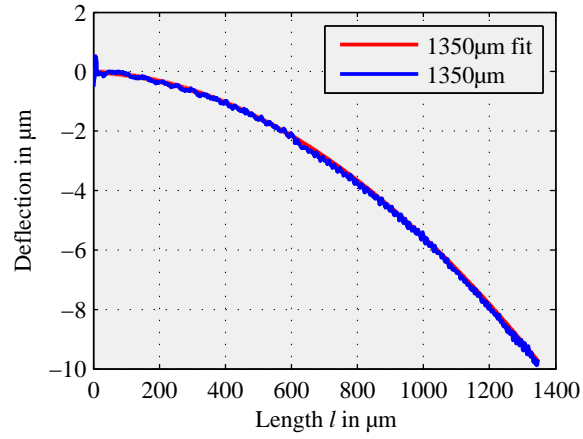


Figure 6.13: Deflection of a set of cantilevers, measured (blue) and fitted (red) by a polynomial fit of third order. The plot depicts the measured topography and the fitted data with the corresponding small error bar of a 1350 μm long cantilever.

6.3 Thermal Threshold Sensor

The actuators are an essential part of a thermal threshold sensor, but they have to be combined with latching mechanisms to form the threshold sensor. The latching mechanism itself is designed as a barbed hook with a taper angle of 30° . Hence, an irreversible connection is established when the latch is triggered. A principle drawback is the difficulty to design and manufacture the resulting sharp edges. Problems can originate from cracks in the photoresist due to mechanical stresses. To avoid poorly defined dimensions due to the resolution limit of the photolithographic mask and the manufacturing process, the edges have to be rounded with a radius of $4\text{ }\mu\text{m}$. Detailed views of such latching triangles are depicted in Fig. 6.14 and Fig. 6.17.

The offset between a latch and its counterpart, the thermal sensitivity of the actuator, and the initial deformation arising from the manufacturing process, define the activation and release (threshold)- temperature of the sensor. The minimal feature size is specified by the aspect ratio of the manufacturing process. The overlap between one latch and its counterpart has to be sufficiently large to secure a lock. To increase the reproducibility of the threshold temperature, the overlap has to be decreased due to the unknown coefficient of friction. The friction increases the force needed to push the latch and its counterpart along each other. Hence, an increase in the overlap also increases the work needed to trigger the latch. A tradeoff between a secure lock and the work needed to actuate the latch has to be found.

Two different concepts for the threshold sensor are evaluated. One is formed with a bistable beam (Concept A, Fig. 6.14) and the second relies on independent cantilevers holding the latching mechanism (Concept B, Fig. 6.17).

6.3.1 Concept A

For the first concept, the thermal actuator is located next to a bistable beam and the latching mechanisms are connected to this bistable beam. At first, both subsystems act independently of each other. During a cool-down phase, the first latch #1 is activated. When the device is heated up again, the actuator pushes against the bistable beam until it snaps into the second stable position. Figure 6.15 depicts a set of micrographs of the bistable beam during the transition into its second stable position. The images are taken after the device was initially cooled down and the

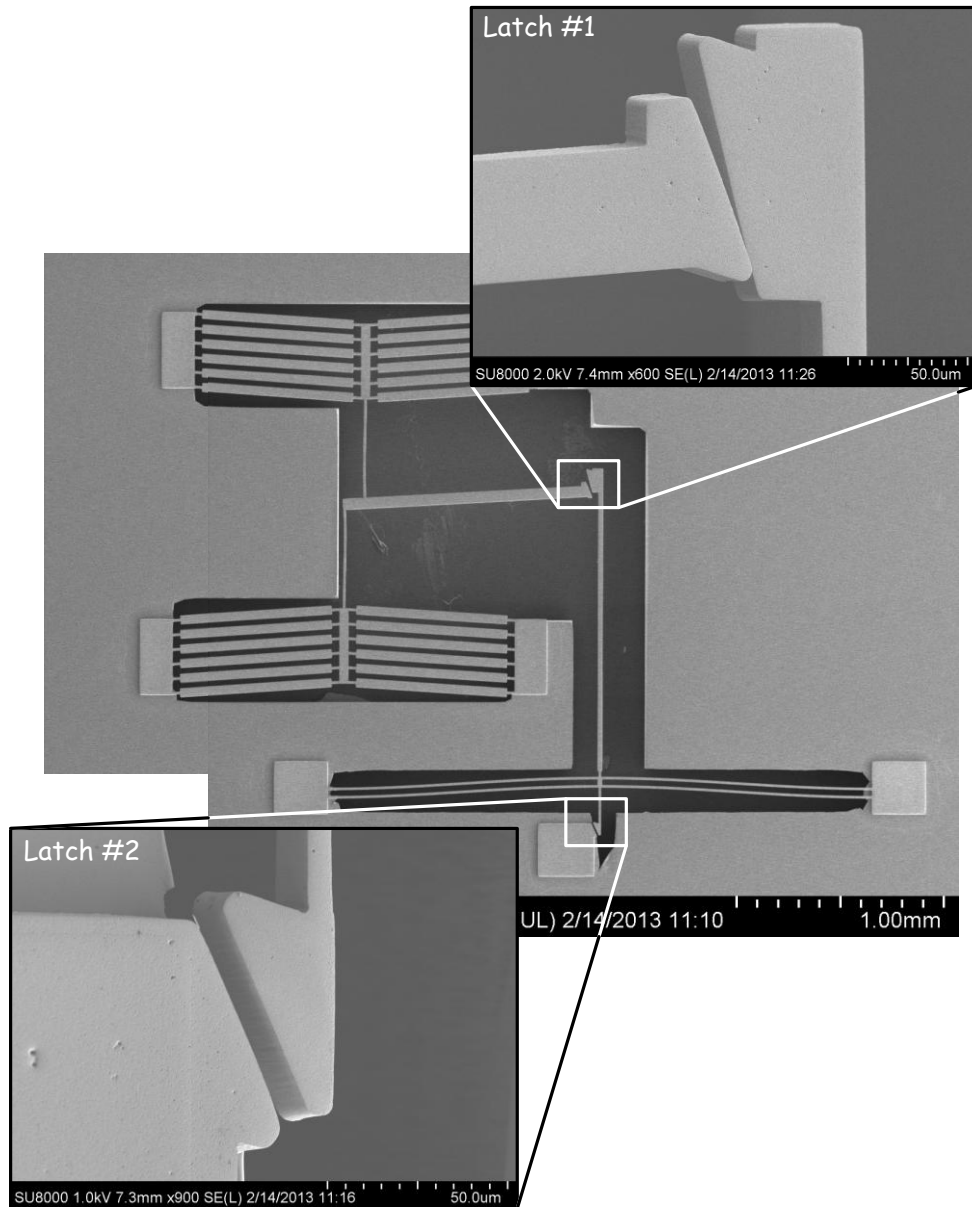


Figure 6.14: SEM micrograph of a threshold sensor comprising the thermal actuator of type B_V and a bistable beam. The inlays depict a detail view of the latch #1 and #2.

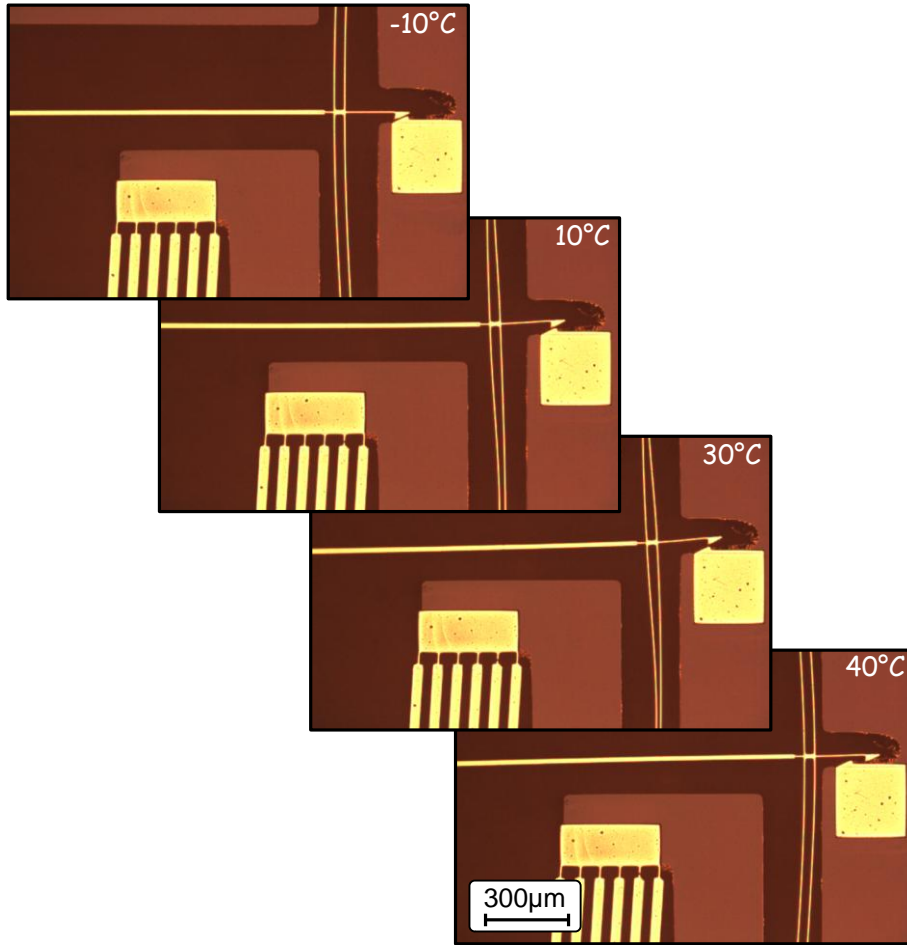


Figure 6.15: Deflection of the bistable beams during heat up of the device, after an initial activation of latch #1.

first latch was triggered already. During the following heating up of the device, the actuator pushes the bistable beam into its second stable position. The point of support, where the actuator pushes against the bistable beam, exhibits a small offset regarding the symmetry of the bistable beam. This eccentric load causes a deformation of the bistable beam, following its second snapping/bending mode (compare Fig. 3.15). Above +30°C the bistable beam snaps through, activating latch #2.

The bistable beam elongates and shrinks with rising and falling temperatures. When the device is cooled down the shrinkage leads to a decreasing apex height h_a (subsec. 3.3.3). This apex height has a major influence on the stabilization of the second stable position. Once a critical minimal

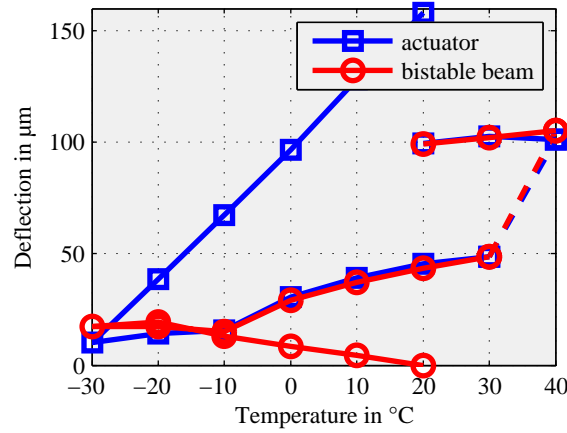


Figure 6.16: Deflection of the thermal actuator and the bistable beam at a full temperature cycle between -30°C and $+40^{\circ}\text{C}$, starting at $+20^{\circ}\text{C}$.

apex height is passed, the bistable beam would switch into its primary position. But this transition is prevented by the latch #2. Furthermore, it forms a short circuit that can be exploited to measure the state of the device.

Figure 6.16 depicts the deflection of the actuator's tip and the bistable beam at a full temperature cycle. Starting at $+20^{\circ}\text{C}$, the device is cooled down and both subsystems act independently from each other. The deflection of the bistable beam due to the thermally induced shrinkage of the material can be observed. Below a temperature of -20°C , the first latch is triggered and during the raise of the temperature, the actuator pushes against the bistable beam. The transition of the bistable beam into its second stable position occurs above a temperature of $+30^{\circ}\text{C}$, indicated in a jump (dashed line) in the measured deflection.

6.3.2 Concept B

The second configuration relies on cantilevers, holding the latch mechanisms and two actuators facing each other (Fig. 6.17). Two beams are connected perpendicular to the cantilever and carry the latching triangles. The connection is established by a kind of hinge with a thin beam.

Figure 6.18 depicts a set of micrographs which reveal the movement and the functional principle of the device. When the device is cooled down,

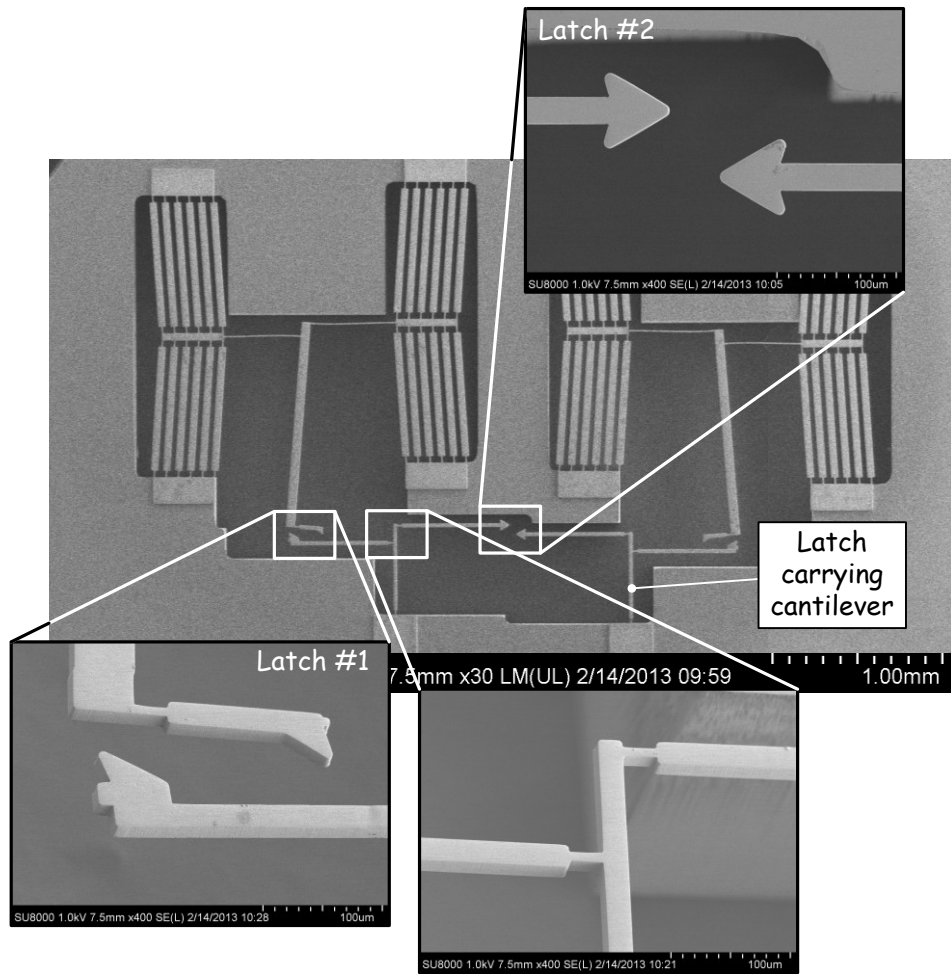


Figure 6.17: SEM micrographs of the thermal threshold sensor comprising a thermal actuator (type B_{VI}) and separate cantilevers, holding the latch mechanisms. The inlays depict a detailed view of latch #1 and #2 and their suspension to the cantilever.

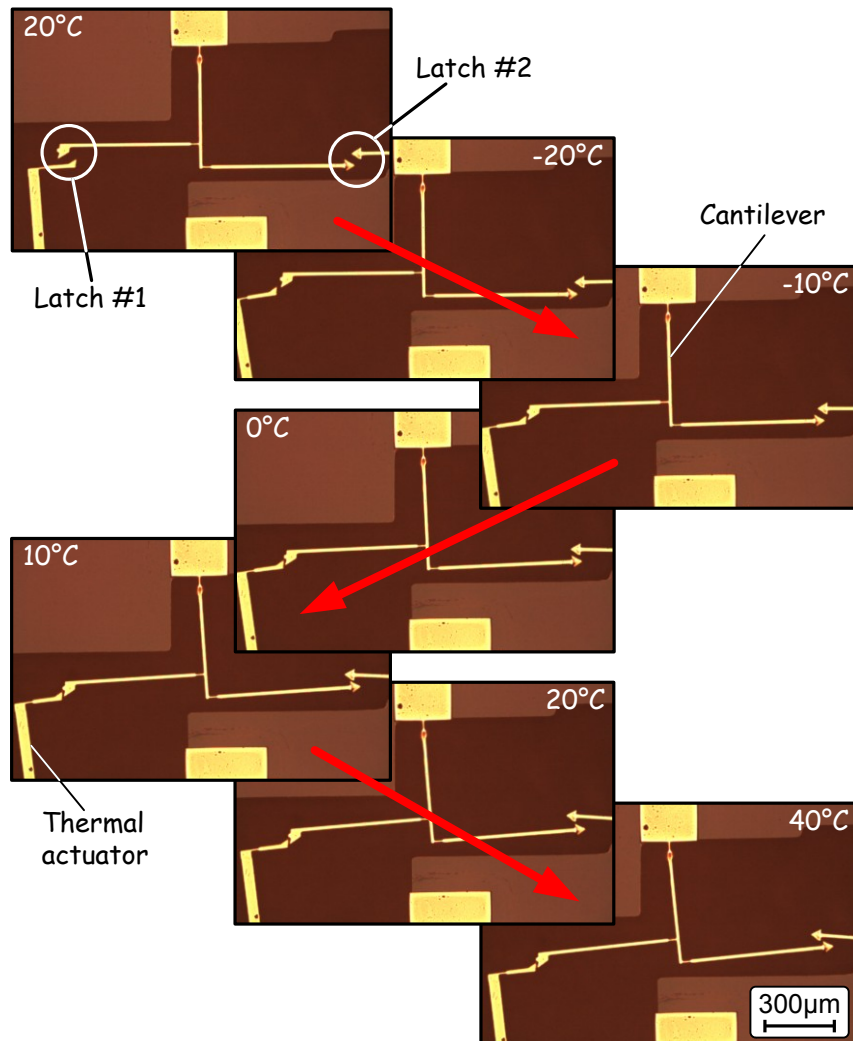
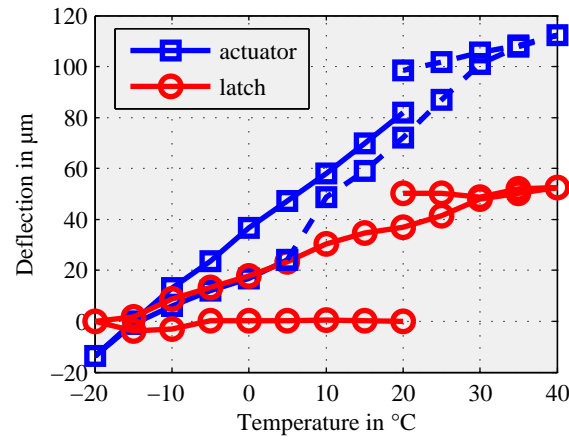


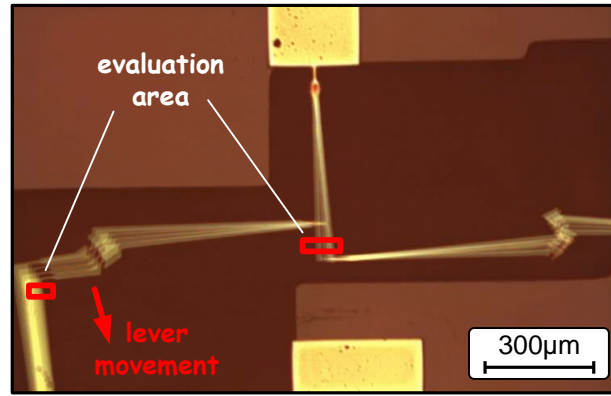
Figure 6.18: Micrographs of the device at different temperatures showing the deflection of the active parts (latch #1 and #2, thermal actuator, latch carrying cantilever).

the lever of the actuator moves to the left until the first latch is triggered at -20°C . When the device is heated up, the actuator pushes against the latch carrying cantilever. Above a temperature of $+30^{\circ}\text{C}$ the second latch is activated and an irreversible contact is established due to the barbed hooks.

As depicted in Fig. 6.19a, both subsystems act independently from each other during the cool-down, but when the temperature of -5°C is exceeded, the deflection of the actuator seems to be larger than of the



(a)



(b)

Figure 6.19: (a) Deflection of the actuator and the latch holding cantilever during a full temperature cycle starting at +20°C. (b) Overlay of the deflections at a set of temperatures indicating a transverse movement of the lever.


cantilever pushed by it. This is due to the different locations where the movement of the parts is evaluated, as depicted in Fig. 6.19b. The micrograph is an overlay of images taken at a set of temperatures. It can be observed that the lever of the actuator also moves in a transverse direction. At a temperature of -5°C the second latch gets into contact with its counterpart. Due to the transverse movement, the different evaluation areas, and the fact that the measurement evaluation script only considers a horizontal movement, the slope of the deflection of the actuators appears increased.

6.3.3 Readout

The different concepts have in common, that once latch #2 is activated, it forms an electrical short circuit. This connection remains, even when the device is cooled down again. For proof of concept, only a micro manipulator and an ampere-meter was necessary to measure the resistivity before and after the contact of the second latch was established (sec. 5.6).

The currents in the open condition are measured to be in the range of $i_o = 20 - 950 \mu\text{A}$ for a voltage of 50 mV. An SiO_2 insulation should separate individual parts with different electrical potentials. But from the standard deviation it can be assumed that this insulation layer is insufficient or contaminations lead to some unexpected short circuits.

Once a contact at latch #2 is established, the current in this short circuit condition is measured to be $i_{sc} = 0.5 - 3.7 \text{ mA}$ (at 50 mV), limited only by the measurement range of the ampere-meter of $i_{\max} = 3.7 \text{ mA}$. Also when it seems in the micrographs that a contact between the latch and its counterpart is established, some of the samples exhibit a short circuit current of only $\sim 500 \mu\text{A}$, which is lower than the open circuit condition of some of the other samples. This can be contributed again to contaminations. The samples are manufactured in a clean room but the measurements and investigations are commonly carried out under normal laboratory conditions. Hence, it cannot be excluded that some contaminations prevent a proper electrical contact.

Nevertheless, aside from some spikes, a clear transition between open and short circuit condition can be measured, once the threshold temperature is exceeded. 

"Progress happens so fast today, that one, who declares something totally unfeasible, is being interrupted by someone else, who has already done it."

Albert Einstein

"A conclusion is the place where you got tired thinking."

Martin H. Fischer

7 Conclusion and What the Future Brings



THE scientific journey that begun with the basic idea of how to monitor the temperature of reefer cargo comes to an end with this chapter. The distance covered is reviewed and summarized. The goals achieved are highlighted and the results are discussed. Also an outlook into the future is given that shows how the solution of the problem can be improved by applying recent developments or by adding subsystems that could not be considered due to the limited time and costs of the project.

7.1 Conclusion

The needs for passive threshold sensors are given in medical and nutrition industry for a continuous observation of transport- and storage-temperature of individual cargo. The basic idea is to combine RFID technology for individual observation with a passive sensing element. Electrical power is transferred via the RFID antenna and a readout-unit, e.g., handheld RFID reader. The power is interimly stored in a capacitance, the state of the device is checked, and a corresponding response is transmitted to the readout-unit.

The sensing element has to be completely passive and easily applied to the cargo. A challenging constrain is that the device is manufactured and

stored between room temperature and elevated temperatures. It has to be activated when it is applied to the reefer cargo and has to remember whether a specific threshold temperature is exceeded. The threshold temperature is commonly in between the activation temperature and the fabrication temperature. On the long term, the complete device should be miniaturized and all subsystem should be merged together in a single sensor grain. Hence, the fabrication processes of the MEMS subsystem have to be CMOS compatible.

Due to the constrain of a passive device, an intrinsic physical material parameter has to be exploited to monitor the temperature that does not need external powering. The thermal expansion of a material can be used to convert thermal energy, due to changes in the temperature of the cargo, into mechanical energy. Hence, a thermal actuator with a large temperature dependent deflection is designed, forming in combination with a sophisticated latch mechanism the thermal threshold sensor element. The present work focuses on this mechanical transducer. Different designs for thermal actuators featuring large temperature dependent deflections were investigated. Generic designs, based on V-shaped beam stacks and adequate lever transmissions were compared to topology optimized designs. The topology optimization was carried out by means of numerical simulations. Care must be taken that the yield strength of the material is not exceeded. The lever transmission results in some energy losses. Hence, the thermally induced energy cannot be fully transformed into mechanical energy. The lever transmission has to be tuned adequately to the V-shaped beam stacks and the required output. Numerical simulations are carried out to predict the behavior of the designs. The temperature dependent deflection is simulated, taking into account the intrinsic stresses and the initial deformations due to the manufacturing process. The blocking force of the actuator is approximated by fixing the tip of the structures in the simulations. The force-displacement product is a measure for the work the actuator can provide and how efficiently the thermal energy is converted into the mechanical energy.

The numerical simulated and measured performance of the structures is compared to an analytical model. The analytical model calculates the deformation of the beams, defined by the static Euler-Bernoulli beam theory, and the energy equilibrium of the thermally induced energy in combination with the deformation energy. Even when some rough approximations were assumed, the model fits very well with the measured and simulated deflections.

Several approaches were investigated to manufacture the devices. At first, SU-8 was utilized, due to its high coefficient of thermal expansion. This material exhibits an unexpected non-linear behavior around 0°C. It can be assumed that this is caused by residual water in the resist. Hence, alternative approaches have been searched for. Ni was selected as active material, owing to its material properties and its long term stability. A commercially available multi-user-multi-project process and a self designed process were exploited to manufacture the MEMS devices. Both approaches use electroplated Ni as active material on a Si wafer. The structures are defined by photo-lithography and formed with electroplated Ni. The substrate wafer beneath the structures is partly etched to release the structures. The self designed process results in much smoother surfaces and less intrinsic stresses compared to the commercially available process.

A self tailored chamber in combination with a microscope and a camera system allows for the investigation of the deflection of the structures at different temperatures in the range from -40°C up to $+50^{\circ}\text{C}$. A purging step with nitrogen prevents the condensation of residual water on cold surfaces.

The resonance frequencies of a set of cantilevers with different lengths are measured with a laser Doppler vibrometer. A simple analytical formula of an Euler-Bernoulli beam was applied to recalculate the Young's modulus of the material. This calculation is only an approximation, since the exact density of the material is uncertain (derived from literature) and the analytic formula Eq. 5.2 is only valid for beams with a specific length to width ratio. It can be observed that the resonance frequency differs drastically from the analytic values for shorter beam lengths. A more complex theory must be applied, such as, e.g., Timoshenko¹ beam theory or plate theories.

White light interference methods are applied to measure the topology of the devices and to calculate the vertical stress gradients. Intrinsic stresses and the coefficients of thermal expansion were measured by optical means and adjusted in numerical finite element simulations to fit the measurements.

Thermal actuators with a large temperature dependent deflection were designed and manufactured. The resulting thermal performance are depicted in Fig. 7.1. The upper graph depicts the simulated blocking force

¹Stepan Prokopovych Tymoshenko, Ukrainian engineer, 1878-1972.

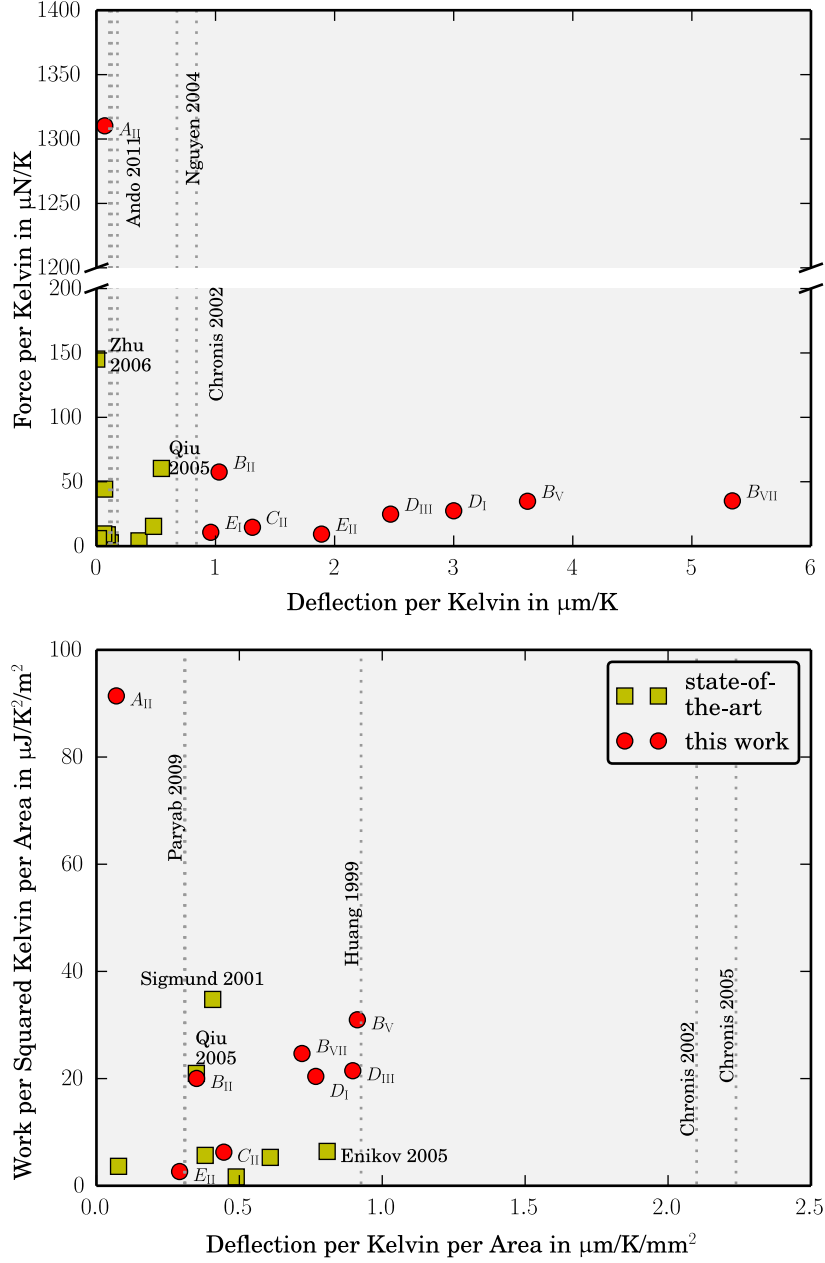


Figure 7.1: Overview of the performance of the investigated designs compared to state-of-the-art actuators. Vertical dashed lines mark the deflections per Kelvin and area-specific deflections of relevant publications that miss data concerning the available actuation forces.

per Kelvin versus the deflection per Kelvin, whereas the lower graph shows the area-specific work (force-displacement product per area) vs. the area specific deflection per Kelvin. This work measures how efficient the actuator transforms thermally induced energy into mechanical work. The single V-shaped beam stack (**A_{II}**) has the highest area specific work, but at the expense of a very low thermal deflection. Compared to state-of-the-art actuators, the temperature dependent deflection could be increased by a factor of more than five with still an area specific work, beating standard thermal actuators. The topology optimized actuators (**E**-type) exhibit also a higher temperature dependent deflection than state-of-the-art devices, but the area-specific work is lower. This is disappointing since they should be designed to offer high area-specific work. But the optimization is not applied in a proper way. At first, an area is designed to exhibit a high deflection at a specific point. This deflection is manually increased by applying a lever transmission. Instead of aiming for a high deflection, the work should have been optimized to convert it into an in-plane deflection with the lever transmission.

Two different approaches for the required latching geometries were chosen. Both approaches comprise two latches, at which the first is activated when the device is cooled down and the second one is activated when the device is heated up again, exceeding a certain threshold temperature. The latches are either attached to a bistable beam (concept A) or to independent cantilevers (concept B) that are pushed by the actuator. Once the structures are activated and the threshold temperature is exceeded, a contact is irreversibly established that can be read out by a resistance measurement. A difference between open and short circuit condition of several orders of magnitude can be expected. With the equipment used, only a minimum resistance of 13 m Ω could be resolved. In the open circuit condition a resistance of >120 Ω was measured. Table 7.1 summarizes activation and threshold temperatures of the realized prototypes. The observed transition temperatures differ from the intended temperatures due to measurement errors. Also the fabrication causes intrinsic stresses and, hence, initial deformations that influence the activation temperatures. Furthermore, the coefficients of friction were neglected and also the deformation of the cantilevers of concept B. Hence, higher forces and temperatures are needed to trigger the latches. The influence of the thermal expansion of the bistable beam was misinterpreted during the design process, resulting in a higher threshold temperature.

Activation and threshold temperatures are reproducible within a range of

	measured		intended	
	activation	threshold	activation	threshold
Ep: A	-10	40	-15	20
Ep: B	-10	45	-10	20
Hp: A	-20	25	-10	10
HP: B	-25	35	-10	20

Table 7.1: Measured activation and threshold temperatures of the prototypes, compared to the intended temperatures. EP: Europractice; HP: Happy Plating; A: Latch-concept A; B: Latch-concept B.

5 K. Furthermore, no long term instability was observed during storage of one month under labor conditions.

These results provide a proof of concept of the passive MEMS temperature threshold sensor.

7.2 Outlook

There is an ongoing scientific progress in technological processes that also lead to enhanced designs. The thermal actuators can be improved by an increased aspect ratio of the lithography. On the one hand, a smaller feature size allow for a better thermal performance, because the maximum stresses can be reduced by a smaller beam width. Hence, also the losses due to mechanical deformations can be reduced, resulting in better energy conversion of the thermally induced energy into mechanical work. On the other hand, increasing the structure height, strongly increases the out-of-plane stiffness. In the presented designs, the latching mechanism can be released by a repeated knocking of the device against a hard surface. The structures are only 16 μm in height and when a force deflects the lever out-of-plane, the latch can accidentally be released. This can be avoided by a guidance above and below the critical structure regions.

The activation and threshold temperatures of the presented samples can be influenced by the offsets between the latches. Assuming a thermal actuator with a temperature sensitivity of 5 $\mu\text{m}/\text{K}$, a minimal feature size of the fabricated structures of 7 μm and an angle of the latch triangles of 30°, a minimal temperature difference between the activation and threshold temperature of approximately 5 K comes in range.

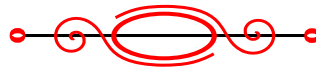
A much greater improvement can be achieved by applying different material combinations with a larger difference in their coefficients of thermal

expansion. For instance CuGe_2P_3 has a CTE of $\alpha = 37.6 \text{ ppm/K}$, which is by a factor of three larger than the CTE of Ni. Recently, new metamaterials with tunable and even negative CTE were introduced and investigated [123]. A combination of a substrate with negative CTE and a material with high CTE would impressively increase work that such an actuator can prove. There is still the issue with the yield strength, limiting the maximum deflection. But for a disposable device, also a small plastic deformation of the material could be accepted.

The design of the latching mechanism and the electrical short circuit can be improved further to increase the reproducibility for the whole sensing element. For instance, gold covering the Ni structure will help to establish a short circuit contact with high reproducibility. This Au layer could be sputtered, which would lead to a sidewall covering of approximately 1:10, compared to the top surface. Due to an under etch of the seed-layer beneath the Ni, a short circuit to the substrate can be avoided.

Also the unexpected lateral movements of the lever of the thermal actuator during pushing against the latching cantilever have to be investigated in detail.

The developments in the field of small scale antenna technology allow for the combination of MEMS devices and antenna on a single chip [124,125]. This is essential for a sensor-grain comprising, sensor, antenna, storage capacitor, and electrical readout circuit. ◀◀



Bibliography

- [1] John R. Allegra, John Brennan, Vicki Lanier, Robert Lavery, and Bruce MacKenzie. Storage temperatures of out-of-hospital medications. *Academic Emergency Medicine*, 6(11):1098–1103, 1999.
- [2] Lawrence H. Brown, Kurt Krumperman, and Christopher J. Fullagar. Out-of-hospital medication storage temperatures: A review of the literature and directions for the future. *Prehospital Emergency Care*, 8(2):200–206, January 2004.
- [3] Lagerprobleme: AKH muss Blutkonserven vernichten. http://diepresse.com/home/panorama/wien/663224/Lagerprobleme_AKH-muss-Blutkonserven-vernichten, May 2011.
- [4] T. F. Mendoza, B. A. Welt, S. Otwell, A. A. Teixeira, H. Kristonsson, and M. O. Balaban. Kinetic parameter estimation of time-temperature integrators intended for use with packaged fresh seafood. *Journal of Food Science*, 69(3):FMS90–FMS96, 2004.
- [5] Marco Riva, Luciano Piergiovanni, and Alberto Schiraldi. Performances of time-temperature indicators in the study of temperature exposure of packaged fresh foods. *Packaging Technology and Science*, 14(1):1–9, January 2001.
- [6] SuessCo KG, Rathausplatz 18, 3130 Herzogenburg, Austria. <http://www.suessco.com>, March 2014.
- [7] Technische Universität Wien: Kühlkette unterbrochen? Magnet-Sensor bringt Sicherheit. http://www.tuwien.ac.at/aktuelles/news_detail/article/8165/?no_cache=1, April 2013.
- [8] Bernhard Bergmair, Jian Liu, Thomas Huber, Oliver Gutfleisch, and Dieter Suess. Wireless and passive temperature indicator utilizing the large hysteresis of magnetic shape memory alloys. *Applied Physics Letters*, 101(4):042412, 2012.
- [9] Thomas Huber, Bernhard Bergmair, Christoph Vogler, Florian Bruckner, Gino Hrkac, and Dieter Suess. Magnetoelastic resonance sensor for remote strain measurements. *Applied Physics Letters*, 101(4):042402, 2012.

- [10] J. W. Wittwer, M. S. Baker, D. S. Epp, and J. A. Mitchell. MEMS passive latching mechanical shock sensor. In *Proceedings of the ASME Design Engineering Technical Conferences*, volume 4, pages 581–588. American Society of Mechanical Engineers; American Society of Mechanical Engineers, 2009.
- [11] Gabriel M. Rebeiz. RF MEMS switches: status of the technology. In *TRANSDUCERS, Solid-State Sensors, Actuators and Microsystems, 12th International Conference on, 2003*, volume 2, pages 1726–1729, 2003.
- [12] Yong Jia Lv, Wen Zhong Lou, Chuan Qin Liu, and Long Fei Zhang. Performance analysis of a novel MEMS terminational latch mechanism. *Key Engineering Materials*, 483:705–710, June 2011.
- [13] Mustafa Emre Karagozler, Jason D. Campbell, Gary K. Fedder, Seth Copen Goldstein, Michael Philetus Weller, and Byung Woo Yoon. Electrostatic latching for inter-module adhesion, power transfer, and communication in modular robots. In *Intelligent Robots and Systems, 2007. IROS 2007. IEEE/RSJ International Conference on*, pages 2779–2786, 2007.
- [14] Luke J. Currano, Scott Bauman, Wayne Churaman, Marty Peckerar, James Wienke, Seokjin Kim, Miao Yu, and Balakumar Balachandran. Latching ultra-low power MEMS shock sensors for acceleration monitoring. *Sensors and Actuators A: Physical*, 147(2):490–497, October 2008.
- [15] Luke J. Currano, Miao Yu, and Balakumar Balachandran. Latching in a MEMS shock sensor: Modeling and experiments. *Sensors and Actuators A: Physical*, 159(1):41–50, April 2010.
- [16] A. Unamuno and D. Uttamchandani. MEMS variable optical attenuator with vernier latching mechanism. *IEEE Photonics Technology Letters*, 18(1):88–90, January 2006.
- [17] R. R. A. Syms, H. Zou, J. Stagg, and D. F. Moore. Multistate latching MEMS variable optical attenuator. *IEEE Photonics Technology Letters*, 16(1):191–193, January 2004.
- [18] R. R. A. Syms, H. Zou, and J. Stagg. Micro-opto-electro-mechanical systems alignment stages with vernier latch mechanisms. *Journal of Optics A: Pure and Applied Optics*, 8(7):S305–S312, July 2006.
- [19] Vivek Agrawal. A latching MEMS relay for DC and RF applications. In *Electrical Contacts, 2004. Proceedings of the 50th IEEE*

- Holm Conference on Electrical Contacts and the 22nd International Conference on Electrical Contacts*, pages 222–225, 2004.
- [20] P. R. Ouyang, R. C. Tjiptoprodjo, W. J. Zhang, and G. S. Yang. Micro-motion devices technology: The state of arts review. *The International Journal of Advanced Manufacturing Technology*, 38(5-6):463–478, August 2008.
- [21] Bijoyraj Sahu, Curtis R. Taylor, and Kam K. Leang. Emerging challenges of microactuators for nanoscale positioning, assembly, and manipulation. *Journal of Manufacturing Science and Engineering*, 132(3):030917, 2010.
- [22] Cornelius T. Leondes. *MEMS/NEMS: Handbook techniques and applications. Manufacturing methods*. Springer, 2006.
- [23] A. A. Geisberger, N. Sarkar, M. Ellis, and G. D. Skidmore. Electrothermal properties and modeling of polysilicon microthermal actuators. *Journal of Microelectromechanical Systems*, 12(4):513–523, August 2003.
- [24] G. K. Lau, J. F. L. Goosen, F. van Keulen, Trinh Chu Duc, and P. M. Sarro. Polymeric thermal microactuator with embedded silicon skeleton: Part I - Design and analysis. *Journal of Microelectromechanical Systems*, 17(4):809–822, August 2008.
- [25] Hergen Kapels, Robert Aigner, and Josef Binder. Fracture strength and fatigue of polysilicon determined by a novel thermal actuator. *Electron Devices, IEEE Transactions on*, 47(7):1522–1528, 2000.
- [26] John H. Comtois and Victor M. Bright. Applications for surface-micromachined polysilicon thermal actuators and arrays. *Sensors and Actuators A: Physical*, 58(1):19–25, January 1997.
- [27] John H. Comtois and Victor M. Bright. Surface micromachined polysilicon thermal actuator arrays and applications. In *Proc. Solid-State Sensor and Actuator Workshop*, pages 174–177, 1996.
- [28] Imed Zine-El-Abidine and Michal Okoniewski. A tunable radio frequency MEMS inductor using MetalMUMPs. *Journal of Micromechanics and Microengineering*, 17(11):2280–2287, November 2007.
- [29] John H. Comtois, M. Adrian Michalicek, and Carole Craig Barron. Electrothermal actuators fabricated in four-level planarized surface micromachined polycrystalline silicon. *Sensors and Actuators A: Physical*, 70(1):23–31, 1998.

- [30] Eniko T. Enikov and Kalin Lazarov. PCB-integrated metallic thermal micro-actuators. *Sensors and Actuators A: Physical*, 105(1):76–82, June 2003.
- [31] C. D. Lott, T. W. McLain, J. N. Harb, and L. L. Howell. Modeling the thermal behavior of a surface-micromachined linear-displacement thermomechanical microactuator. *Sensors and Actuators A: Physical*, 101(1):239–250, 2002.
- [32] Long Que, Jae-Sung Park, Mo-Huang Li, and Y. B. Gianchandani. Reliability studies of bent-beam electro-thermal actuators. In *Reliability Physics Symposium, 2000. Proceedings. 38th Annual 2000 IEEE International*, pages 118–122, 2000.
- [33] Rana I. Shakoor, Prasanna Srinivasan, and S. A. Bazaz. Performance of a compliant structure for a thermal resonant microgyroscope. *IEEE Sensors Journal*, 11(6):1465–1475, June 2011.
- [34] Michael J. Sinclair. A high force low area MEMS thermal actuator. In *Thermal and Thermomechanical Phenomena in Electronic Systems, 2000. ITherm 2000. The Seventh Intersociety Conference on*, volume 1, 2000.
- [35] J. J. Khazaai, M. Haris, Hongwei Qu, and J. Slicker. Displacement amplification and latching mechanism using V-shape actuators in design of electro-thermal MEMS switches. In *2010 IEEE Sensors*, pages 1454–1459, 2010.
- [36] Jonathan W. Wittwer, Michael S. Baker, and Larry L. Howell. Simulation, measurement, and asymmetric buckling of thermal microactuators. *Sensors and Actuators A: Physical*, 128(2):395–401, April 2006.
- [37] Bruno Ando, Salvatore Baglio, Nicolo Savalli, and Carlo Trigona. Cascaded "Triple-Bent-Beam" MEMS sensor for contactless temperature measurements in nonaccessible environments. *IEEE Transactions on Instrumentation and Measurement*, 60(4):1348–1357, April 2011.
- [38] Craig Arthur, Neil Ellerington, Ted Hubbard, and Marek Kuja. MEMS earthworm: A thermally actuated peristaltic linear micromotor. *Journal of Micromechanics and Microengineering*, 21(3):035022, March 2011.
- [39] Chihchung Chen, Chengkuo Lee, Chia-Yu Wu, Hong-Da Lee, Wen-Chih Chen, and Ruey-Shing Huang. Novel X-shaped electrother-

- mal actuators with large displacement. In *Proceedings of the Asia-Pacific conference on transducers and micro-nano technology*, 2004.
- [40] Nikolas Chronis and Luke P. Lee. Polymer-based actuators integrated into microfluidic systems. In Yoshinobu Baba, Shuichi Shoji, and Albert van den Berg, editors, *Micro Total Analysis Systems 2002*, pages 754–756. Springer Netherlands, January 2002.
- [41] N. Chronis and L. P. Lee. Electrothermally activated SU-8 micro-gripper for single cell manipulation in solution. *Journal of Microelectromechanical Systems*, 14(4):857–863, August 2005.
- [42] Mojgan Daneshmand, Siamak Fouladi, Raafat R. Mansour, Mario Lisi, and Tony Stajcer. Thermally-actuated latching RF MEMS switch. In *Microwave Symposium Digest, 2009. MTT'09. IEEE MTT-S International*, pages 1217–1220, 2009.
- [43] E. T. Enikov, S. S. Kedar, and K. V. Lazarov. Analytical model for analysis and design of V-shaped thermal microactuators. *Journal of Microelectromechanical Systems*, 14(4):788–798, August 2005.
- [44] Changhong Guan and Yong Zhu. An electrothermal microactuator with Z-shaped beams. *Journal of Micromechanics and Microengineering*, 20(8):085014, August 2010.
- [45] Qing-An Huang and Neville Ka Shek Lee. Analysis and design of polysilicon thermal flexure actuator. *Journal of Micromechanics and Microengineering*, 9(1):64, 1999.
- [46] J. Khazaai, M. Haris M. Khir, Hongwei Qu, and James Slicker. Design and fabrication of a low power electro-thermal V-shape actuator with large displacement. In *Proc. NSTI-Nanotech*, volume 2, pages 681–684, 2010.
- [47] Jay J. Khazaai, Hongwei Qu, Meir Shillor, and Lorenzo Smith. Design and fabrication of electro-thermally activated micro gripper with large tip opening and holding force. In *Sensors, 2011 IEEE*, pages 1445–1448, 2011.
- [48] Jay Jamshid Khazaai and Hongwei Qu. Electro-thermal MEMS switch with latching mechanism: Design and characterization. *IEEE Sensors Journal*, 12(9):2830–2838, September 2012.
- [49] Chengkuo Lee and Chia-Yu Wu. Study of electrothermal V-beam actuators and latched mechanism for optical switch. *Journal of Micromechanics and Microengineering*, 15(1):11–19, January 2005.

- [50] J. K. Luo, Y. Q. Fu, J. A. Williams, and W. I. Milne. Thermal degradation of electroplated nickel thermal microactuators. *Journal of Microelectromechanical Systems*, 18(6):1279–1287, December 2009.
- [51] Hirotugu Matoba, Toshio Ishikawa, C.-J. Kim, and Richard S. Muller. A bistable snapping microactuator. In *Micro Electro Mechanical Systems, 1994, MEMS'94, Proceedings, IEEE Workshop on*, pages 45–50, 1994.
- [52] Nam-Trung Nguyen, Soon-Seng Ho, and Cassandra Lee-Ngo Low. A polymeric microgripper with integrated thermal actuators. *Journal of Micromechanics and Microengineering*, 14(7):969–974, July 2004.
- [53] Sahil Oak, Sandesh Rawool, Ganapathy Sivakumar, Egbert J. Hendriske, Daniel Buscarello, and Tim Dallas. Development and testing of a multilevel chevron actuator-based positioning system. *Journal of Microelectromechanical Systems*, 20(6):1298–1309, December 2011.
- [54] K. Ogando, N. La Forgia, J. J. Zarate, and H. Pastoriza. Design and characterization of a fully compliant out-of-plane thermal actuator. *Sensors and Actuators A: Physical*, 183:95–100, August 2012.
- [55] Nasim Paryab, Hamid Jahed, and Amir Khajepour. Creep and fatigue failure in single- and double hot arm MEMS thermal actuators. *Journal of Failure Analysis and Prevention*, 9(2):159–170, February 2009.
- [56] Jin Qiu, J. H. Lang, A. H. Slocum, and A. C. Weber. A bulk-micromachined bistable relay with U-shaped thermal actuators. *Journal of Microelectromechanical Systems*, 14(5):1099–1109, October 2005.
- [57] L. Que, M.-H. Li, L. L. Chu, and Y. B. Gianchandani. A micromachined strain sensor with differential capacitive readout. In *Micro Electro Mechanical Systems, 1999. MEMS'99. Twelfth IEEE International Conference on*, pages 552–557, 1999.
- [58] Long Que, Jae-Sung Park, and Yogesh B. Gianchandani. Bent-beam electrothermal actuators-Part I: Single beam and cascaded devices. *Microelectromechanical Systems, Journal of*, 10(2):247–254, 2001.

- [59] Ole Sigmund. Design of multiphysics actuators using topology optimization- Part I: One-material structures. *Computer methods in applied mechanics and engineering*, 190(49):6577–6604, 2001.
- [60] Mathew Stevenson, Peng Yang, Yongjun Lai, and Chris Mechefske. Development of a bidirectional ring thermal actuator. *Journal of Micromechanics and Microengineering*, 17(10):2049–2054, October 2007.
- [61] J. Wei, T. Chu Duc, and P. M. Sarro. An electro-thermal silicon-polymer micro-gripper for simultaneous in-plane and out-of-plane motions. In *Proc. of Eurosensors 2008*, pages 7–10, 2008.
- [62] Dong Yan, Amir Khajepour, and Raafat Mansour. Design and modeling of a MEMS bidirectional vertical thermal actuator. *Journal of Micromechanics and Microengineering*, 14(7):841–850, July 2004.
- [63] Yu-Sheng Yang, Yu-Hsin Lin, Yi-Chiuen Hu, and Cheng-Hsien Liu. A large-displacement thermal actuator designed for MEMS pitch-tunable grating. *Journal of Micromechanics and Microengineering*, 19(1):015001, January 2009.
- [64] Yong Zhu, Alberto Corigliano, and Horacio D. Espinosa. A thermal actuator for nanoscale *in situ* microscopy testing: Design and characterization. *Journal of Micromechanics and Microengineering*, 16(2):242–253, February 2006.
- [65] Herbert B. Callen. *Thermodynamics and an Introduction to Thermostatistics*. Wiley, New York, 2 edition edition, September 1985.
- [66] C. H. Mastrangelo and C. H. Hsu. Mechanical stability and adhesion of microstructures under capillary forces. I. Basic theory. *Microelectromechanical Systems, Journal of*, 2(1):33–43, 1993.
- [67] C. H. Mastrangelo and C. H. Hsu. Mechanical stability and adhesion of microstructures under capillary forces. II. Experiments. *Microelectromechanical Systems, Journal of*, 2(1):44–55, 1993.
- [68] Bharat Bhushan. Adhesion and stiction: Mechanisms, measurement techniques, and methods for reduction. *Journal of Vacuum Science & Technology B: Microelectronics and Nanometer Structures*, 21(6):2262, 2003.
- [69] Niels Tas, Tonny Sonnenberg, Henri Jansen, Rob Legtenberg, and Miko Elwenspoek. Stiction in surface micromachining. *Journal of Micromechanics and Microengineering*, 6(4):385, December 1996.

- [70] Jeremy A. Walraven. Future challenges for MEMS failure analysis. In *International Test Conference*, pages 850–855, 2003.
- [71] Marc J. Madou. *Fundamentals of Microfabrication: The Science of Miniaturization*. CRC Press, 2002.
- [72] Tao Ma and Bin Zheng. A COMSOL based programming-language implementation of structure topology optimization with stress constraints. In *Computer Engineering and Technology (ICCET), 2010 2nd International Conference on*, volume 5, pages V5–170, 2010.
- [73] Ole Sigmund and Salvatore Torquato. Design of materials with extreme thermal expansion using a three-phase topology optimization method. *Journal of the Mechanics and Physics of Solids*, 45(6):1037–1067, 1997.
- [74] O. Sigmund and P. M. Clausen. Topology optimization using a mixed formulation: An alternative way to solve pressure load problems. *Computer Methods in Applied Mechanics and Engineering*, 196(13-16):1874–1889, March 2007.
- [75] Claus B. W. Pedersen, Thomas Buhl, and Ole Sigmund. Topology synthesis of large-displacement compliant mechanisms. *International Journal for Numerical Methods in Engineering*, 50(12):2683–2705, 2001.
- [76] Warren Clarence Young and Raymond Jefferson Roark. *Roark's formulas for stress and strain*. McGraw-Hill, New York, NY [u.a.], 2002.
- [77] Mattias Vangbo and Ylva Bäcklund. A lateral symmetrically bistable buckled beam. *Journal of Micromechanics and Micro-engineering*, 8(1):29, 1998.
- [78] M. Vangbo. An analytical analysis of a compressed bistable buckled beam. *Sensors and Actuators A: Physical*, 69(3):212–216, 1998.
- [79] Jin Qiu, Jeffrey H. Lang, and Alexander H. Slocum. A centrally-clamped parallel-beam bistable MEMS mechanism. In *Micro Electro Mechanical Systems, 2001. MEMS 2001. The 14th IEEE International Conference on*, pages 353–356, 2001.
- [80] J. Qiu, J. H. Lang, and A. H. Slocum. A curved-beam bistable mechanism. *Journal of Microelectromechanical Systems*, 13(2):137–146, April 2004.
- [81] Jin Qiu. *An electrothermally-actuated bistable MEMS relay for power applications*. PhD thesis, Massachusetts Institute of Technology, 2003.

- [82] N. D. Masters and L. L. Howell. A self-retracting fully compliant bistable micromechanism. *Journal of Microelectromechanical Systems*, 12(3):273–280, June 2003.
- [83] Rajesh Loharuka and Peter J. Hesketh. Design of fully compliant, in-plane rotary, bistable micromechanisms for MEMS applications. *Sensors and Actuators A: Physical*, 134(1):231–238, February 2007.
- [84] Y. Gerson, S. Krylov, B. Ilic, and D. Schreiber. Large displacement low voltage multistable micro actuator. In *Micro Electro Mechanical Systems, 2008. MEMS 2008. IEEE 21st International Conference on*, pages 463–466, 2008.
- [85] www.webelements.com/. <http://www.webelements.com/>, March 2014.
- [86] David R. Lide. *CRC handbook of chemistry and physics: A ready-reference book of chemical and physical data : 2008-2009*. CRC Press, Boca Raton; London; New York, 2008.
- [87] Your cell phone has more computing power than NASA circa 1969. <http://knopfdoubleday.com/2011/03/14/your-cell-phone/>, March 2011.
- [88] Hubert Lorenz, M. Laudon, and Philippe Renaud. Mechanical characterization of a new high-aspect-ratio near UV-photoresist. *Microelectronic engineering*, 41:371–374, 1998.
- [89] Daniel Bachmann, Bernd Schöberle, Stephane Kühne, Yves Leiner, and Christofer Hierold. Fabrication and characterization of folded SU-8 suspensions for MEMS applications. *Sensors and Actuators A: Physical*, 130-131:379–386, August 2006.
- [90] Benjamin Bohl, Reinhard Steger, Roland Zengerle, and Peter Koltay. Multi-layer SU-8 lift-off technology for microfluidic devices. *Journal of Micromechanics and Microengineering*, 15(6):1125–1130, June 2005.
- [91] A. del Campo and C. Greiner. SU-8: A photoresist for high-aspect-ratio and 3D submicron lithography. *Journal of Micromechanics and Microengineering*, 17(6):R81–R95, June 2007.
- [92] J. Hammacher, A. Fuelle, J. Flaemig, J. Saupe, B. Loechel, and J. Grimm. Stress engineering and mechanical properties of SU-8-layers for mechanical applications. *Microsystem Technologies*, 14(9-11):1515–1523, January 2008.

- [93] Alvaro Mata, Aaron J. Fleischman, and Shuvo Roy. Fabrication of multi-layer SU-8 microstructures. *Journal of Micromechanics and Microengineering*, 16(2):276–284, February 2006.
- [94] Volker Seidemann, Sebastian Bütetisch, and Stephanus Büttgenbach. Fabrication and investigation of in-plane compliant SU8 structures for MEMS and their application to micro valves and micro grippers. *Sensors and Actuators A: Physical*, 97:457–461, 2002.
- [95] P. Svasek, E. Svasek, B. Lendl, and M. Vellekoop. Fabrication of miniaturized fluidic devices using SU-8 based lithography and low temperature wafer bonding. *Sensors and Actuators A: Physical*, 115(2-3):591–599, September 2004.
- [96] Lung-Jieh Yang and Kuan-Chun Liu. SU-8 buckled-type microvalves switched by surface tension forces. In *Nano/Micro Engineered and Molecular Systems, 2007. NEMS'07. 2nd IEEE International Conference on*, pages 105–108, 2007.
- [97] Harald Steiner, Franz Keplinger, Wilfried Hortschitz, and Michael Stifter. The non-linear thermal behavior of SU-8. In *Electronics Technology (ISSE), 2012 35th International Spring Seminar on*, pages 450–454, 2012.
- [98] Kristof Wouters and Robert Puers. Diffusing and swelling in SU-8: insight in material properties and processing. *Journal of Micromechanics and Microengineering*, 20(9):095013, September 2010.
- [99] V. M. Blanco Carballo, J. Melai, C. Salm, and J. Schmitz. Moisture resistance of SU-8 and KMPR as structural material for integrated gaseous detectors. *Microelectronic Engineering*, 86(4–6):765–768, April 2009.
- [100] Stephan Keller, Daniel Haefliger, and Anja Boisen. Fabrication of thin SU-8 cantilevers: Initial bending, release and time stability. *Journal of Micromechanics and Microengineering*, 20(4):045024, April 2010.
- [101] B. Schoeberle, M. Wendlandt, and C. Hierold. Long-term creep behavior of SU-8 membranes: Application of the time-stress superposition principle to determine the master creep compliance curve. *Sensors and Actuators A: Physical*, 142(1):242–249, March 2008.
- [102] Alongkorn Pimpin and Werayut Srituravanich. Review on micro- and nanolithography techniques and their applications. *Engineering Journal*, 16(1):37–56, January 2012.

- [103] W. E. G. Hansal, H. Steiner, R. Mann, M. Halmdienst, J. Schalko, and F. Keplinger. Microgalvanic nickel pulse plating process for the production of thermal actuators. In *Proc. SPIE 8763, Smart Sensors, Actuators, and MEMS VI*, volume 8763, pages 87632X–1–87632X–7, May 2013.
- [104] Wolfgang E. G. Hansal, Barbara Tury, Martina Halmdienst, Magda Lakatos Varsanyi, and Wolfgang Kautek. Pulse reverse plating of Ni-Co alloys: Deposition kinetics of watts, sulfamate and chloride electrolytes. *Electrochimica Acta*, 52(3):1145–1151, November 2006.
- [105] Happy Plating GmbH, Viktor-Kaplan-Straße 2D, 2700 Wiener Neustadt. <http://www.happyplating.eu/>, March 2013.
- [106] H. Steiner, W. Hortschitz, M. Stifter, F. Keplinger, and T. Sauter. Highly sensitive thermal actuators for temperature sensing. In *Proc. SPIE 8763, Smart Sensors, Actuators, and MEMS VI*, volume 8763, pages 87630T–87630T–7, May 2013.
- [107] H. Steiner, W. Hortschitz, M. Stifter, F. Keplinger, and T. Sauter. Thermal actuators featuring large displacements for passive temperature sensing. *Microsystem Technologies*, 20(4–5):551–557, 2014.
- [108] Europractice Consortium. <http://www.europractice-ic.com/>, March 2014.
- [109] MEMSCAP SA., Parc Activillage des Fontaines ZI Bernin, 38 926 Crolles Cedex, France. <http://www.memscap.com/>, March 2014.
- [110] L. Almeida, R. Ramadoss, R. Jackson, K. Ishikawa, and Q. Yu. Study of the electrical contact resistance of multi-contact MEMS relays fabricated using the MetalMUMPs process. *Journal of Micromechanics and Microengineering*, 16(7):1189–1194, July 2006.
- [111] M. Driesen, F. Ceyssens, J. Decoster, and R. Puers. Nickel-plated thermal switch with electrostatic latch. *Sensors and Actuators A: Physical*, 164(1-2):148–153, November 2010.
- [112] Jui-che Tsai, Ren-Jie Lai, Chun-Yi Yin, Dian-Sheng Chen, and Po-Fan Yeh. An out-of-plane rotational platform with in-plane electrostatic combs made by the MetalMUMPs process. *Journal of Micromechanics and Microengineering*, 19(7):074007, July 2009.
- [113] M. Daneshmand, S. Fouladi, R. R. Mansour, M. Lisi, and T. Stajcer. Thermally actuated latching RF MEMS switch and its charac-

- teristics. *IEEE Transactions on Microwave Theory and Techniques*, 57(12):3229–3238, December 2009.
- [114] Keith Miller, Allen Cowen, Greg Hames, and Busbee Hardy. SOI-MUMPs design handbook. *MEMScAP Inc., Durham*, 2004.
- [115] Wolfgang E. G. Hansal, Harald Steiner, R. Mann, M. Halmdienst, J. Schalko, F. Keplinger, and P. Svasek. Microgalvanic nickel pulse plating process for the fabrication of thermal microactuators. *Microsystem Technologies*, 20(4–5):681–689, 2014.
- [116] Matthias Sachse. *Development of a capacitive transducer for a fully implantable middle ear microphone*. PhD thesis, Vienna University of Technology, 2011.
- [117] Jae Wook Shin. *Stress generation and relaxation in thin films: The role of kinetics and grain boundaries*. PhD thesis, Brown University, 2009.
- [118] Siyuan He, John S. Chang, Lihua Li, and Hsu Ho. Characterization of Young’s modulus and residual stress gradient of Metal-MUMPs electroplated nickel film. *Sensors and Actuators A: Physical*, 154(1):149–156, August 2009.
- [119] Chuanjun Liu, Ying Liu, Mordechai Sokuler, Daniela Fell, Stephan Keller, Anja Boisen, Hans-Jürgen Butt, Günter K. Auernhammer, and Elmar Bonaccorso. Diffusion of water into SU-8 microcantilevers. *Physical Chemistry Chemical Physics*, 12(35):10577, 2010.
- [120] Zaifa Zhou, Qing-An Huang, Weihua Li, Wei Lu, Zhen Zhu, and Ming Feng. The swelling effects during the development processes of deep UV lithography of SU-8 photoresists: theoretical study, simulation and verification. In *Sensors, 2007 IEEE*, pages 325–328, 2007.
- [121] Kristof Wouters and Robert Puers. Determining the Young’s modulus and creep effects in three different photo definable epoxies for MEMS applications. *Sensors and Actuators A: Physical*, 156(1):196–200, November 2009.
- [122] J. Luo, A. Flewitt, S. Spearing, N. Fleck, and W. Milne. Young’s modulus of electroplated ni thin film for MEMS applications. *Materials Letters*, 58(17-18):2306–2309, July 2004.
- [123] Joseph N. Grima, Pierre S. Farrugia, Ruben Gatt, and Victor Zammit. A system with adjustable positive or negative thermal expansion. *Proceedings of the Royal Society A: Mathematical, Physical and Engineering Science*, 463(2082):1585–1596, August 2007.

-
- [124] Philipp K. Gentner, Robert Langwieser, Arpad L. Scholtz, Günter Hofer, and Christoph F. Mecklenbräuker. A UHF/UWB hybrid silicon RFID tag with on-chip antennas. *EURASIP Journal on Embedded Systems*, 2013(1):12, August 2013.
 - [125] P.K. Gentner, P. Amreich, H. Reinisch, and G. Hofer. A passive ultra wideband tag for radio frequency identification or wireless sensor networks. In *2012 IEEE International Conference on Ultra-Wideband (ICUWB)*, pages 417–420, 2012.

Danksagung

Als Erstes möchte ich mich bei meiner Familie für die vielfältige Unterstützung bedanken. Es wusste niemand so richtig etwas damit umzugehen, als ich vor so vielen Jahren bekannt gab, dass ich ein Physik-Studium anfangen möchte. Trotzdem erhielt ich immer Rückendeckung von ihr ohne welche mein Studium wahrscheinlich nicht so reibungslos und größtenteils unkompliziert verlaufen wäre, und das nun mit dem Abschluss der Dissertation sicher einen neuen Höhepunkt erreicht hat.

Ich möchte den vielen guten Seelen danken, die mich direkt und indirekt bei meiner Arbeit unterstützt haben. Dem Team von Technologen (Peter u. Eda Svasek, Arthur Jachimowicz, Johannes Schalko) gebührt großer Dank. Ohne ihr reichhaltiges Know-How und ihre akribische Arbeit wären wohl viele technologischen Hürden in dem Projekt nicht zu überwinden gewesen. Ewald Pirker hat seine Fähigkeiten und sein praktisches Wissen zur Verfügung gestellt um die thermische Messkammer zu optimieren und zu fertigen.

Franz Keplinger hat großen Anteil am Erfolg dieser Dissertation. Von ihm stammt die Idee, die dieser Arbeit zugrunde liegt. Es ist ihm auch Hoch anzurechnen, dass er sich immer die Zeit nimmt seinen Studenten bei ihren Problemen zu helfen und ihnen Unterstützung zukommen lässt. Obwohl er mit allen möglichen administrativen Tätigkeiten betraut ist, hat er immer Zeit für Fachgespräche und Unterstützung beim Schreiben und Korrigieren von wissenschaftlichen Texten gefunden.

Ich möchte an dieser Stelle auch Franz Kohl erwähnen, der für mich ein großes Vorbild im wissenschaftlichen Bereich darstellt. Er überrascht immer mit seinem sehr fundierten und breit gefächerten Wissen und verblüfft mit seinem Blick fürs Wesentliche. Ich bin immer wieder erstaunt mit welchen einfachen Abschätzungen er es schafft, sehr komplexe Systeme zu verstehen und mit einer intuitiven und fast prophetischen Gabe zu erwartende Messergebnisse vorhersagen kann.

Einen großen Dankeschön gilt auch meinen Arbeitskollegen Wilfried Hortschitz, Michael Stifter und Thomas Glatzl, ohne die ich mit der Dissertation sicher schneller fertig geworden wäre :-). Ich habe sehr viel von ihnen gelernt und sie haben mich zum Teil angetrieben, als sich die Motivation zum Schreiben der Arbeit dem Tiefpunkt näherte.

Ebenfalls gebührt mein Dank Prof. Bernhard Jakoby der sich dazu bereit erklärt hat als Zweitbetreuer zur Verfügung zu stehen und seinen Bemühungen beim Korrigieren und Verbessern der Arbeit.

Auch die vielfältigen Korrekturleser, mögen hier erwähnt werden: Elisabeth Schiefer, Felix Ring, Andreas Kainz, Franz Kohl, Wilfried Hortschitz, Bernhard Jakoby, Franz Keplinger.

Unserem Ansprechpartner bei Infineon und Projektmanager Gerald Holweg möchte ich dafür danken, dass er immer Interesse an unserer Arbeit gezeigt hat, aber trotz so mancher Schwierigkeiten beim Projekt nie einen Termindruck ausgeübt hat. Auch die Österreichische Forschungsförderungsgesellschaft (FFG) sollte erwähnt werden, ohne deren finanzielle Unterstützung, das Projekt Contactless (RFID) Sensing (Projekt Nr.: 830604) nicht zustande gekommen wäre.

Des Weiteren möchte ich mich bei Frau Sandra Schlager und Frau Silvia Plank bedanken, die mir abseits der Familie und der Arbeitskollegen, durch ihre Freundschaft Kraft, Halt und einen Ausgleich in meinem Leben gegeben haben.

Jedem der diese Danksagung liest sollte bewusst werden, dass sehr viele Personen zum Erfolg einer Dissertation beitragen. Sollte ich unglücklicherweise jemanden vergessen haben zu erwähnen, so bitte ich inständig um Verzeihung.

“Wer arbeitet, macht Fehler.”



About the Author



Harald Steiner was born in Neunkirchen, Austria in 1981. After graduating with distinction from secondary technical collage (Höhere Technische Bundes Lehr- und Versuchsanstalt für Hochbau, Wr.Neustadt, Austria), he studied technical physics at the Vienna University of Technology, receiving his master degree in 2007. The research topic of his master thesis at the Institute of Solid State Physics was in the field of thin film technology. He deepened his knowledge of material science during his work as technical operator for scanning electron mi-

croscopy and atomic force microscopy at the Center of Competence in Applied Electrochemistry. Between 2007 and 2011 he was affiliated with the Institute of Integrated Sensor Systems (Austrian Academy of Science). In particular, he worked on the production of MEMS structures for vibration sensors and in the field of structural health monitoring, especially on numerical and semi-analytical simulation of the propagation of ultrasonic waves in solids. Since 2011 he was with the Institute of Sensor and Actuator systems (Vienna University of Technology), pursuing a Ph.D. degree. Currently he is with the Center for Integrated Sensor Systems (Danube University Krems), working in the field of thermal flow sensors.